Applied Magnetic Resonance (2023) 54:207–287
https://doi.org/10.1007/s00723-022-01511-w

Applied
Magnetic Resonance

REVIEW

High-field/High-frequency EPR Spectroscopy in Protein Research: Principles and Examples

Klaus Möbius[1] · **Anton Savitsky**[2]

Received: 7 October 2022 / Revised: 10 October 2022 / Accepted: 9 November 2022 /
Published online: 13 December 2022

Abstract
During the last decades, the combined efforts of biologists, chemists, and physicists in developing high-field/high-frequency EPR techniques and applying them to functional proteins have demonstrated that this type of magnetic resonance spectroscopy is particularly powerful for characterizing the structure and dynamics of stable and transient states of proteins in action on biologically relevant time scales ranging from nanoseconds to hours. The review article describes how high-field EPR methodology, in conjunction with site-specific isotope and spin-labeling strategies, is capable of providing new insights into fundamental biological processes. Specifically, we discuss the theoretical and instrumental background of continuous-wave and pulse high-field EPR and the multiple-resonance extensions EDNMR, ENDOR, TRIPLE, ESEEM, PELDOR, and RIDME. Some emphasis is placed on a balanced description of both the historical spadework and the achieved performance of advanced EPR at 95 GHz and 360 GHz. This culminates in a coherent treatment of state-of-the-art research of high-field EPR in terms of both instrumentation development and application to representative protein complexes such as cofactor binding sites in photosynthesis.

1 Introduction

During the last 30 years or so, high-field/high-frequency EPR spectroscopy is rapidly growing. Application of ever higher magnetic fields and microwave frequencies results in spectacular improvements of both spectral and time resolution.

✉ Klaus Möbius
moebius@physik.fu-berlin.de

✉ Anton Savitsky
anton.savitsky@tu-dortmund.de

[1] Department of Physics, Free University Berlin, Arnimallee 14, 14195 Berlin, Germany

[2] Faculty of Physics, Technical University Dortmund, Otto-Hahn-Str. 4a, 44227 Dortmund, Germany

Thereby, more complex spin systems can be studied by EPR, very much in analogy to what has happened in modern NMR spectroscopy decades earlier. The reasons for this time delay between EPR and NMR developments are obvious: EPR has to cope with resonance frequencies three orders of magnitude larger than in NMR and correspondingly shorter electron spin relaxation times. The resulting requirements in adequate microwave technology were challenging and needed their time to be solved. It was only after the lifting of the East/West "Iron Curtain" in the early 1990's when low-noise mm microwave sources, fast switches and detectors, which had been developed in the military domain, became available also for unclassified research in the public domain, for instance at universities and basic-research institutions. These devices deliver and process microwave power in the range of several 10 milliwatt at frequencies up to several 100 GHz necessary for fast pulsed high-field EPR. Nowadays, we witness multifrequency and multi-dimensional EPR benchmark experiments at the technical limits of quasioptical sub-mm microwave bridges and sweepable wide-bore cryomagnets with homogeneous Zeeman fields of up to 10 Tesla and beyond [1].

Our review contribution to this Special Issue of *Applied Magnetic Resonance* is intended as an introduction for students and experts alike. It is offering guiding principles of high-field/high-frequency EPR spectroscopy and the characteristics of its specific instrumentation. This goes along with illustrative examples, most of them from our own research work in biochemistry and molecular biology, supplemented by a few examples from dedicated laboratories around the world other laboratories as well. We hope that the mixture of introductory and specialized sections of the article will be interesting for both specialists and newcomers in this fascinating area of research and instrumentation development.

Our research described was performed in collaboration projects with numerous internationally renowned spectroscopy groups, and this in teamwork with undergraduate and graduate students, postdocs and senior scientists from around the world. A stronghold of the projects was photochemistry and photobiology, with emphasis on the cofactors of photosynthesis in interaction with their immediate molecular environment of the "solvent matrix".

In more recent years, our cooperation network developed to a Platonic octahedron with six groups at the cornerstones (the vertices): Novosibirsk, Kazan, Moscow, Bologna, Berlin, and Mülheim (Ruhr). This network was 2018 extended by a seventh group in Dortmund (Anton Savitsky, previously in Berlin and Mülheim) resulting in a more complex polyhedron of collaborations that can be visualized as an augmented triangular prism with seven vertices (see Fig. 1). The collaborations focus on light-initiated electron-transfer processes in natural and artificial photosynthesis. They require a variety of advanced multifrequency, multiresonance EPR techniques to be characterized in detail [2–18].

The unique potential of high-field/high-frequency EPR spectroscopy for studying complex spin systems was recognized by a few research groups already more than 45 years ago, and Yakov S. Lebedev and his group at the NN Semenov Institute of Chemical Physics in Moscow were the first to start a dedicated high-field/high-frequency research and development program. They had realized the distinct advantages of high-field/high-frequency EPR compared to conventional X-band EPR. In a

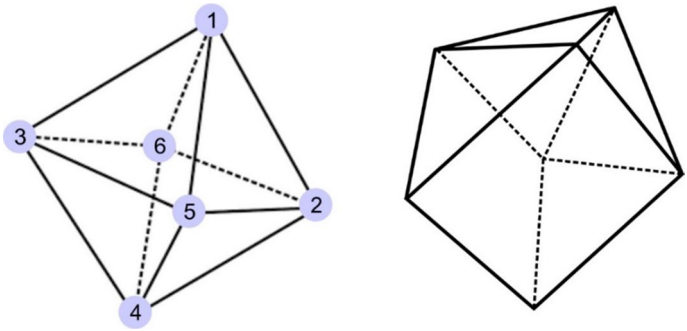

Fig. 1 Left: Platonic octahedron of EPR collaborations between six groups (the vertices, the names of the respective group leaders are given in parentheses) in Novosibirsk (Renad Sagdeev), Kazan (Kev Salikhov), Moscow (Alexey Semenov), Bologna (Giovanni Venturoli), Berlin (Klaus Möbius), and Mülheim/Ruhr (Wolfgang Lubitz). Right: Since 2018, the octahedron was extended by Dortmund (Anton Savitsky) to a more complex polyhedron of collaborations visualized as an augmented triangular prism with seven vertices

nutshell, the advantages are enhanced spectral resolution and orientational selectivity even for disordered molecules with small g-tensor anisotropy, enhanced spectral separation of radicals with only slightly different g-values, enhanced time resolution for tracing transient radical intermediates, enhanced detection sensitivity for small samples with low spin concentration, increased sensitivity toward molecular motion conformational changes and associated relaxation effects by transforming motionally narrowed EPR spectra into the slow-motion regime. In 1976, they completed a versatile continuous-wave (cw) high-field EPR spectrometer employing a 150 GHz microwave source and a 5 T superconducting magnet. In the following, the advantages of the high-field EPR will be discussed in some detail.

1.1 Why EPR at High Magnetic Fields/Microwave Frequencies?

In general, EPR spectroscopy has proven to be a very useful technique for studying both stable and transient radical-pair intermediates in liquid and solid phases. For large low-symmetry spin systems, however, standard X-band EPR (9.5 GHz) soon reaches its limits of useful information content, unless single-crystal samples are available. Unfortunately, large molecular complexes are often available only as disordered samples. Their X-band EPR spectra are poorly resolved, and the information on magnetic parameters and molecular orientations is hidden under broad lines due to strong inhomogeneous line broadening. By turning to higher and higher magnetic fields and microwave frequencies, for example to EPR at W-band (95 GHz) or even at 360 GHz, at least five important features, (i), (ii)–(v), are emerging from the EPR spectra: (i) enhanced spectral resolution; (ii) enhanced orientational selectivity in disordered samples; (iii) enhanced low-temperature electron spin polarization; (iv) enhanced detection sensitivity for restricted-volume samples such as small protein single crystals, and (v) enhanced sensitivity for probing fast motional dynamics, i.e.,

high-frequency EPR makes a faster ''snapshot'' for characterizing complex molecular motions.

Ad (i): The strategy for spectral resolution enhancement is similar in EPR and NMR: With increasing external Zeeman field the field-dependent spin interactions in the spin Hamiltonian are separated from the field-independent ones (see Fig. 2). In high-field EPR, the g-factor resolution is increased in relation to the hyperfine couplings, in high-field NMR the chemical-shift resolution is increased in relation to the spin–spin couplings.

Resolution problems due to inhomogeneous line broadening also arise when several radical species or different magnetic sites of rather similar g-values are present in the sample. Or when a small g-tensor anisotropy of the paramagnetic system does not allow canonical orientations of the powder EPR spectrum to be resolved.

For "real" high-field EPR experiments, properties of the spectrometer have to be related with properties of the sample: For all cases of delocalized spin systems, in which unresolved hyperfine interactions dominate the inhomogeneous EPR linewidth, a real high-field experiment must fulfill the condition:

$$\frac{\Delta g}{g_{\mathrm{iso}}} \cdot B_0 > \Delta B, \tag{1}$$

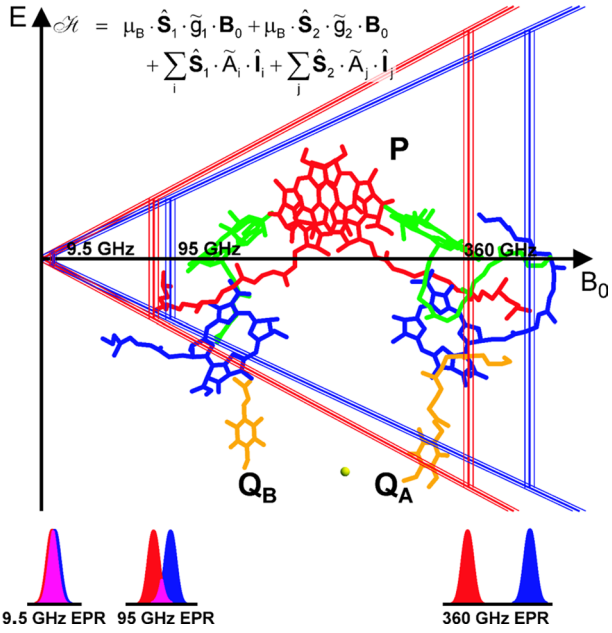

Fig. 2 Enhanced spectral resolution by high-field EPR, taking the cofactor radical ions in bacterial photosynthetic reaction centers as example, with P the primary donor, Q_A and Q_B the quinone acceptors. The spin Hamiltonian in the inset describes two radicals in an external Zeeman field B_0 and contains the Zeeman interactions of the two electron spins S_1, S_2 and their hyperfine interactions with the nuclear spins I_i, I_j in the radicals. For details, see text

i.e., the anisotropic electron Zeeman interaction, described by the difference Δg of principal g-tensor components, must exceed the EPR inhomogeneous linewidth ΔB. On the other hand, when ΔB is reduced by isotope labeling, e.g., by perdeuteration of the nitroxide spin-label molecule and/or ^{15}N-substitution of ^{14}N, lower B_0 fields may already be sufficient to meet the condition for true high-field EPR, Eq. (1). In certain systems, the reduction of ΔB by isotope labeling may be the only way to enhance the spectral resolution when field-dependent g-strain effects become the linewidth-determining parameter at higher Zeeman fields, see [1].

Ad (ii): The important feature of enhanced orientation selectivity by high-field EPR on randomly oriented spin systems becomes essential for organic radicals with only small g-anisotropy (see Fig. 3). For example, below room temperature the overall rotation of a protein complex often becomes so slow that powder-type EPR spectra are obtained. However, if the anisotropy of the leading interaction tensor in the spin Hamiltonian is larger than the inhomogeneous linewidth, the canonical orientations of the interaction tensor can be resolved. As a consequence, single-crystal-like information on the hyperfine interactions can be extracted by performing orientation-selective ENDOR at the field values of resolved spectral features. In the case of transition-metal complexes, however, the hyperfine anisotropy of the metal ion may provide this orientation selectivity from the entire orientational distribution of the molecules. Their g-anisotropy is often large enough to allow for distinct orientational selectivity already in X-band EPR and single-crystal like ENDOR spectra [19–21]. For a detailed elucidation of the molecular structure and orientation of large biological complexes, such as membrane proteins, this is an important strategy because preparation of single crystals is often difficult or even impossible.

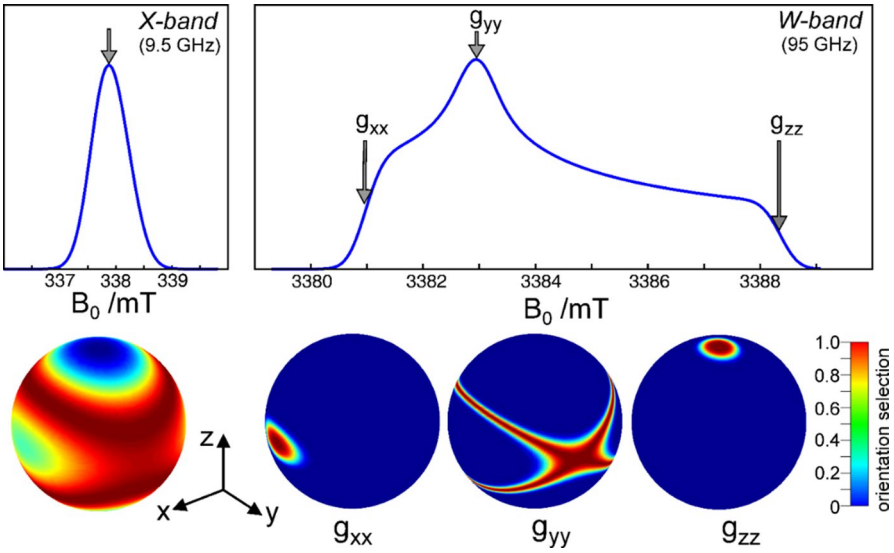

Fig. 3 Enhanced orientation selectivity by high-field EPR, taking the anion radical of the ubiquinone acceptor cofactor in frozen-solution bacterial photosynthetic reaction centers as example

Ad (iii): Because of the enhanced low-temperature electron spin polarization at sufficiently large Zeeman fields, the absolute sign of the zero-field splitting parameter, D, of a two-spin system such as biradicals or triplet states can be determined. At high fields, considerable thermal spin polarization can be achieved already well above helium temperature. The necessary condition is that the sample temperature becomes comparable with the Zeeman temperature, $T_z = g \cdot \mu_B \cdot B_0/k_B$ (g: electron g-factor, μ_B: Bohr magneton, B_0: Zeeman field; k_B: Boltzmann constant). At $T \gg T_Z$, the characteristic triplet powder EPR spectrum (see Fig. 4) is symmetric at its low- and high-field sides and, hence, contains no information of the sign of D. At $T < T_Z$, the Boltzmann distribution leads to increased populations of the low-energy levels, resulting in asymmetric line shapes from which the absolute sign of D can be directly read off. Thermal spin polarization as a means to determine the absolute sign of D in high-spin systems has been used at a variety of EPR frequencies, for example at 9.5 GHz ($T_Z \approx 0.4$ K) [22], at 95 GHz ($T_Z \approx 4$ K) [23], 140 GHz ($T_Z \approx 6.5$ K) [24], 360 GHz ($T_Z \approx 15.5$ K) [25].

Ad (iv): With respect to detection sensitivity and its enhancement with increasing microwave frequencies, one has to distinguish between the absolute and relative (concentration) sensitivities. The absolute sensitivity is defined by the minimum detectable number of spins in the sample, $N_{\min}$; the relative sensitivity is given by $N_{\min}/V_S$, i.e., is scaled by the sample volume, V_S. This is limited by the amount of sample that can be placed into the cavity of high-field EPR spectrometers which, of course, is usually significantly smaller than standard X-band cavities. Consequently, if the amount of sample available is limited like in single crystals of proteins, the sensitivity of high-field EPR can be superior by orders of magnitude

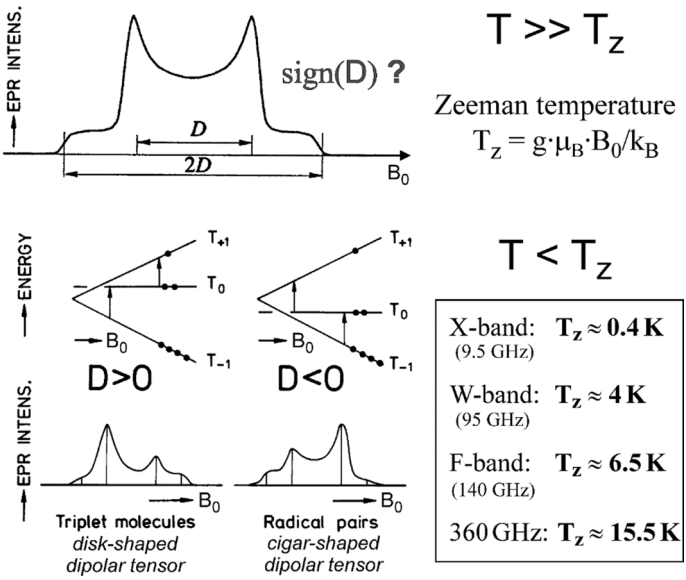

Fig. 4 Enhanced thermal spin polarization by high-field EPR, taking mechanically generated radical pairs in a donor–acceptor mixture as example. For details, see [23]

because the absolute sensitivity grows with increasing frequencies much stronger than the relative sensitivity does. Under certain experimental conditions, for constant incident microwave power and unsaturated EPR lines, one obtains theoretical expressions for the absolute sensitivity, $N_{\min} \propto \omega_0^{-9/2}$, and for the relative sensitivity, $N_{\min}/V_S \propto \omega_0^{-3/2}$ (see the detailed sensitivity discussions in refs. [26, 27]).

Ad (v): The faster ''snapshot'' capability for complex motional dynamics with increasing EPR frequency can be used in a multifrequency continuous-wave (cw) EPR approach at the same temperature to probe fast internal modes of motion and to discriminate them from the slow restricted motion of a macromolecule in solution. In high-frequency cw EPR spectra, slow motions appear to be frozen out, whereas fast motions dominate the observed spectral lineshape [28–31].

1.2 NMR *Versus* EPR

For many decades after the invention of EPR and NMR in the 1940s, the popularity of EPR has been hopelessly behind its famous (though younger) sister NMR, and it is only during the last decades that the chemistry, biology and physics communities appreciate the dramatic catching up of EPR in modern magnetic resonance spectroscopy. The reasons for EPR's large-scale jump ahead are to be found in the remarkable technological breakthroughs in pulsed microwave technology, sweepable cryomagnet fabrication and fast data acquisition and handling instrumentation. Modern advanced EPR is apparently booming, rather similar to what had happened with NMR 15–20 years earlier, both exhibiting unique and complementary capabilities in elucidating structure and dynamics of complex (bio)chemical systems in the fluid, glassy, or solid state.

The technical requirements for pulsed NMR and pulsed EPR are dramatically different and related to the different time scales of the NMR and EPR phenomena. They are a consequence of the vastly different magnetic moments of nuclei and electrons (for example for ^{1}H, the magnetic moment ratio is $1.5 \cdot 10^{-3}$, for ^{14} N it is $1.1 \cdot 10^{-4}$). Thus, the time scales are determined by the nuclear and electron resonance frequencies, in the radiofrequency (rf) and microwave (mw) domains, respectively. And the characteristic frequency separations in the respective resonance spectra (Hz versus MHz) and the relaxation times T_1, T_2 (ms *versus* ns) are vastly different. Because of the long nuclear T_1 and T_2 times in diamagnetic molecules, NMR 90° and 180° pulses need not be shorter than 10 μs, which to generate and detect coherently does not pose technical problems. The electronic transverse relaxation times (T_2), however, are typically in the 100 ns range and, consequently, in EPR, the mw 90° and 180°pulses have to be as short as a few ns. To generate and detect them coherently poses great technical problems even today. This holds, for example, for the mw sources with adequate output power, for fast mw switches and mixers as well as for fast electronic semiconductor components and computers for controlling the pulse trains, likewise for detecting and handling the transient signals in the ns time scale.

Nowadays, pulse NMR has completely replaced cw NMR, culminating in multidimensional Fourier Transform (FT) spectroscopy. High-field steady-state cryomagnets and nuclear resonance frequencies up to 1 GHz (for protons) have dramatically

improved the detection sensitivity and chemical-shift separations. And even formerly exotic nuclei have become routinely observable by now. Despite the spectacular breakthroughs in mm and sub-mm microwave technologies in the last decade, in EPR the cw versus pulse situation is still very different from that in NMR. In fact, the general prognosis is that coexistence between cw and pulse EPR will continue to persist. Which option to choose will be determined entirely by the sample under study. The specific sample properties and relaxation times ultimately dictate the preference for either a cw or pulse experiment to be performed.

Regarding spectral resolution and detection sensitivity, both modern EPR and NMR spectroscopies follow similar strategies: to apply higher and higher static Zeeman fields to separate field-dependent from field-independent spin interactions in the molecular system. By this strategy not only otherwise overlapping lines can be disentangled, but also the population difference and quantum energy of the driven transitions between electron and nuclear spin energy levels will be increased allowing for the detection of fewer and fewer spins.

1.3 Chronological Account

EPR and NMR phenomena were originally discovered in radiofrequency spectroscopy experiments employing cw electromagnetic fields, EPR in 1944 by E. K. Zavoisky at Kazan University, NMR in 1946 by E. M. Purcell, H. G. Torrey and R. V. Pound at Harvard University and, independently, by F. Bloch, W. Hansen and M. E. Packard at Stanford University. These classic NMR experiments were honored as early as 1952 by the Nobel Prize in Physics to Bloch and Purcell. Zavoisky's discovery of EPR, on the other hand, was only inadequately recognized on the West side of the Iron Curtain—in contrast to the East side: In 1957, E. K. Zavoisky was awarded the Lenin Prize, the highest sign of recognition in the former USSR for his discovery of ''The Electron Paramagnetic Resonance Phenomenon''. It was not until 1977 that E. K. Zavoisky was finally also honored internationally. Though not by a Nobel Prize, but at least by the prestigious ISMAR Award of the International Society of Magnetic Resonance. The Award was conferred in May 1977 at the ISMAR Conference in Banff, Canada—alas posthumously [18], because he had already died in Moscow in October 1976, just after having been informed about the decision of the international ISMAR Prize Committee.

Up to the 1960's, both NMR and EPR remained to be cw methods, i.e., the samples in the static magnetic field (the Zeeman field B_0) were irradiated with continuous radiofrequency (rf) and microwave (mw) fields to drive NMR and EPR transitions, respectively. But it was as early as 1949, when E. L. Hahn at Urbana University applied *rf* pulses and invented the nuclear "spin-echo" detection. This, together with the introduction of powerful fast computers for "Fast Fourier transformation" in the late 1970s, opened the arena for FT-NMR spectroscopy. R. R. Ernst was awarded the Nobel Prize in Chemistry in 1991 for his contributions toward the development of Fourier transform nuclear magnetic resonance spectroscopy while at Varian Associates and ETH Zurich (Richard R. Ernst, Nobel Lecture, Nuclear Magnetic Resonance Fourier Transform Spectroscopy, December 9, 1992). Fourier

transform NMR has an enormous potential for recording multi-dimensional spectra of complex biosystems in the liquid and solid state, and for applications in medical imaging such as MRI diagnostics.

It took almost a decade before R. J. Blume at Columbia University [32] observed, for the first time, electron spin echoes analogous to Hahn's nuclear spin echoes. And it took many more years before electron spin echo-detected EPR (ESE) methodologies gained sufficient experimental and theoretical backing to revolutionize FT-EPR spectroscopy, see A. Schweiger and G. Jeschke [33].

Pulse EPR spectroscopy has many discoverers, both from the theoretical and the experimental side. In the early 1970s, K. M. Salikhov at Akademgorodok (Novosibirsk) [34] laid the theoretical foundation for several advanced pulse EPR methods. For example, he developed the theory of electron spin phase relaxation by stochastic modulation of the dipole–dipole interaction between paramagnetic centers and its effect on the ESE decay [35]. He suggested the first pulse ELDOR (PELDOR) protocol to observe the modulation of the ESE signal due to the electron–electron dipolar interaction of weakly coupled biradical systems in disordered solids [36]. Some years later, K. M. Salikhov theoretically predicted new spin phenomena, such as quantum beats of the EPR line intensity [37] and out-of-phase spin echoes of correlated radical pairs [38]. These spin phenomena should be observable in time-resolved EPR spectra of transient spin-polarized radical-pair intermediates. And, indeed, such new spin phenomena were observed in several laboratories shortly after they had been predicted. A prominent example of application was the bacterial photosynthetic reaction center with its donor photoexcited to the singlet state by short laser flashes leading to spin-correlated donor–acceptor radical pairs (for a review of these early experiments, see [39]. A rich variety of mw pulse sequences and sophisticated experiments is found in more recent reviews and text books, for example that of A. Schweiger and G. Jeschke [33]. Pioneering work was done, among others, by W. B. Mims at Bell Telephone Laboratories, Yu. D. Tsvetkov in Novosibirsk, J. H. Freed at Cornell University and A. Schweiger at ETH Zurich.

It was a milestone in the history of magnetic resonance spectroscopy when, in 1956, G. Feher at Bell Labs [40] invented ENDOR (electron–nuclear double resonance). His ingenious concept was to apply simultaneously two electromagnetic fields, one in the mw, the other in the rf range, to drive EPR and NMR transitions having an energy level in common. Thereby, the advantages of EPR (high detection sensitivity) are combined with those of NMR (high resolution capability). Feher's first cw ENDOR experiment was technically feasible only because the sample—phosphorus doped silicon—was kept at low temperature, where all the relaxation times are sufficiently long to easily saturate both EPR and NMR transitions, which is a necessary condition for cw ENDOR. The cw ENDOR technique was later extended to ESE-detected pulse versions for solid-state samples by W. B. Mims (1965) at Bell Labs [41] and E. R. Davies (1974) at Clarendon Laboratory [42]. W.B. Mims is widely acknowledged to be the driving force in pulse EPR in general, and in pulse ENDOR in particular [33].

In contrast to solid-state ENDOR at low temperatures, for radicals in liquid solution the electronic and nuclear relaxation times are much shorter—in the order of 10^{-5} to 10^{-7} s. Consequently, cw ENDOR-in-solution experiments are technically

much more demanding since much larger saturating mw and rf fields have to be applied. This is the reason why liquid-state ENDOR experiments took many more years than solid-state ENDOR experiments before they were successful. The pioneering work was performed by A. L. Cederquist at Washington University [43] in 1963, who studied metal ammonia solutions. And by J. S. Hyde and A. H. Maki at Varian Associates and Harvard University, respectively, in 1964 [44], who studied a stable organic radical dissolved in n-heptane solution. The further development of cw ENDOR-in-solution spectroscopy was highly stimulated by J. H. Freed at Cornell University, whose general theory of saturation and double resonance proved to be adequate for describing amplitude, width, and shape of ENDOR lines in great detail (see, for example, [45]).

There are apparent weaknesses of ENDOR in comparison to EPR concerning sensitivity (typically one order of magnitude lower) and relative line intensities (they do no longer reflect the number of contributing nuclei). These weaknesses can be overcome by extending ENDOR to electron–nuclear–nuclear triple resonance. For the special case of only one set of hyperfine-coupled nuclei, such a triple resonance extension was proposed early on by G. Feher [46] and J. H. Freed [47]. Its experimental realization, however, had to wait until 1974, when K. P. Dinse in the Möbius group at Free University (FU) Berlin accomplished ''Special TRIPLE'' on radicals in liquid solution [48]. In cw Special TRIPLE, the two frequency-swept rf fields are applied at frequencies always symmetrically placed around the Larmor frequency of the respective nucleus. This variant of triple resonance enhances the signal intensity and allows to relate relative line intensities to the number of responsible nuclei. Thereby, the assignment of ENDOR lines to molecular positions is made possible, which is a vital task, but notoriously difficult in ENDOR spectroscopy [49–51].

About a year later, it was demonstrated by R. Biehl in the same group at FU Berlin [52], that additional information about relative signs of hyperfine couplings of radicals in solution—and thereby about their assignment—can be obtained by generalizing the triple resonance experiment to include NMR transitions of different nuclei in the radical ("General TRIPLE"). In cw General TRIPLE, two rf fields with independently variable frequencies are applied, one pumping a selected NMR transition while the other is swept through the ENDOR spectrum. From the resulting characteristic intensity changes in the ENDOR spectrum, the relative signs of the hyperfine couplings can be directly read off. The analog of this experiment for solid-state samples at low temperature (77 K) was performed earlier by R. J. Cook and D. H. Whiffen (1964) at Teddington National Physical Laboratory [53]. They called it ''double ENDOR'', and applied it to X-irradiated organic crystals to determine relative signs of hyperfine couplings. The advantages of TRIPLE over ENDOR—enhanced sensitivity and resolution, information about multiplicity and relative signs of hyperfine couplings from line intensity variations—justify the extra experimental efforts inherent in the triple resonance spectroscopy. It was shown to be extremely powerful in elucidating the electronic structures not only of organic radicals in solution [49] but also of transient cofactor radical–ion intermediates in primary photosynthesis [54, 55].

To measure the electron–nuclear hyperfine and nuclear quadrupole interactions by combinations of EPR and NMR techniques, the nuclear transitions can be

driven either directly by rf fields as in ENDOR or, as a more indirect alternative, by ESEEM (electron spin echo modulation). This single-resonance technique was introduced by W. B. Mims [56] in 1972. He applied a mw spin-echo pulse train with varying inter-pulse separation and observed, on top of the exponential echo-decay trace, echo-amplitude modulations from hyperfine and quadrupole interactions. To obtain detectable echo modulations, efficient mixing of the nuclear and electron spin eigenfunctions by the dipolar hyperfine interaction is mandatory. Consequently, the strength of the external magnetic field has to be properly chosen to balance the Zeeman splitting of the nuclear sublevels and the respective hyperfine splitting (''cancelation condition'').

Concerning the detection of short-lived transient states or reaction intermediates, besides pulsed EPR also specific cw EPR strategies can be used to obtain time-resolved signals. Employing field modulation at a frequency as high as 1 MHz, the time resolution could be extended to the μs range. A decisive step forward to drastically higher time resolution was achieved for fast photoreactions by abandoning field modulation at all but generating the time-dependent EPR signal via wavelength-selective pulsed laser excitation. Subsequent direct, i.e., broadband detection of the transient EPR signal at a fixed Zeeman field value is accomplished by employing sufficiently fast data acquisition systems. The Zeeman field is stepped through the spectrum establishing a time-resolved transient (TR) technique known as ''TREPR''. The pioneering experiment was done by S.I. Weissman and co-workers [57] at Washington University in 1979. In TREPR, the inherent loss of sensitivity for broadband detection of transient paramagnetic states can often be compensated by accumulation of the spectra after each light flash. Moreover, an orders-of-magnitude signal enhancement via electron spin polarization effects can be utilized which occur in many photoreactions. They appear in reactions with instantaneously generated excited states and subsequent fast detection of the transient reaction intermediates, e.g., triplets, radicals, radical pairs, before spin–lattice relaxation can thermalize them (for overviews of electron spin polarization effects, see for example [39, 58, 59]. By now, the time resolution of TREPR has been pushed to the 10 ns range, and TREPR has proven to perform extremely well over a wide range of mw frequencies, from S-band (4 GHz), X-band (9 GHz), K-band (24 GHz), Q-band (35 GHz) up to the high-field EPR frequencies 95 GHz, 120 GHz and 240 GHz [39, 60–62]. For many applications in photochemistry, a multifrequency approach of TREPR experiments with a wide range of Zeeman fields turned out to be essential for the detailed analysis of spin-polarized spectra in case of competing polarization mechanisms.

Long-range distance measurements with the scale of a few nm in chemical and biological systems are an important application for pulse EPR spectroscopy [63]. They are based on the electron–electron dipolar coupling between two spin-carrying domains, which is a function of their interspin distance and relative orientation. The main advantage of pulse versus cw EPR techniques in this endeavor is the ability to separate the electron–electron coupling from other interactions, such as electron–nuclear hyperfine interactions, and to reduce inhomogeneous line broadening. Thereby, the distance range that can be probed is extended to about 8 nm. Yu. D. Tsvetkov and his co-workers at Novosibirsk [36, 64] established the 3-pulse electron–electron double resonance (PELDOR, also called DEER, double

electron–electron resonance) technique in 1981. Later it was extended to a 4-pulse sequence for dead-time free detection [33, 65]. Other powerful pulse sequences for measuring electron–electron frequencies and, thereby, distances have been invented, for example the single-frequency techniques DQC (double-quantum-coherence EPR) by J.H. Freed and co-workers at Cornell [66] and RIDME (relaxation-induced dipolar modulation enhancement) by Yu. D. Tsvetkov and co-workers in Novosibirsk [67].

At this point, we would like to emphasize that the development of high-field/high-frequency EPR marked another leap forward of the capabilities of EPR spectroscopy on (bio)chemical complexes. As many major developments in science, also high-field EPR spectroscopy has several fathers who independently took the decisive actions in a similar period of time. Thorough historical overviews on such developments are provided in the literature, see for instance, [13, 68, 69].

First publications on this subject appeared around 1970 [70–73]. But it was Ya. S. Lebedev in Moscow who was the first to start a long-term research and development program on high-field/high-frequency EPR in physical chemistry, starting in the 70's [69]. In his group, Oleg Grinberg and Alexander Dubinskii were primarily involved in the instrument development [69]. They were inspired by the earlier preliminary experiments of D. J. E. Ingram at the University of Keele [70, 71]. The construction of their high-field/high-frequency EPR started in 1973 in close cooperation with the Physical-Technical Institute in Donetsk (Ukraine). In the following years, several prototypes of the spectrometer were constructed. Different microwave sources including klystrons, BWOs, diffraction generators and solid-state oscillators were tested. Single-mode resonators, oversized cavities and Fabry–Perot resonators, as well as different detectors, were compared in their performance. The first working version of the 140 GHz cw EPR spectrometer, finished in 1979, reached a sensitivity of $4 \cdot 10^8$ spins/mT at 1 Hz bandwidth, which was about three orders of magnitude higher than for X-band EPR at that time. In parallel with the development of EPR instrumentation, the Lebedev group performed a series of EPR experiments approving the advantages of high-field/high-frequency EPR for application to physical, chemical and biological systems.

Yakov Lebedev's contributions certainly set quality benchmarks and widened the horizons in EPR spectroscopy. His early death in 1996 at the age of only 61 was a tragic loss for the whole EPR community, his family and friends, see [6]. In the early 1980s, the Möbius group at Free University Berlin started with their 95 GHz EPR and ENDOR projects [74], and extended them in subsequent years to 360 GHz EPR and ENDOR. These projects focused on applications to protein complexes and model systems (for an overview, see [1]).

Only a few laboratories have developed the instrumentation for millimeter and submillimeter high-field EPR spectrometers, thus ploughing the ground for a promising new field of molecular spectroscopy of complex systems. Until the second half of the 1990s, laboratory-built high-field EPR spectrometers have been described for continuous-wave (cw) microwave irradiation at 95 GHz ($\lambda \approx 3$ mm), for example by the Möbius group at FU Berlin: [74–77], around 150 GHz ($\lambda \approx 2$ mm) [78–80], at 250 GHz ($\lambda \approx 1$ mm) [81–83], and in the sub-mm region [84–86], even reaching 360 GHz/14 T EPR [87]. A few other EPR spectrometers operating at frequencies

above 200 GHz have been described until the end of the 90s [88–91]. High-field EPR spectrometers with pulsed microwave irradiation have also been described during this time, operating at wavelengths of 3 mm [60, 92, 93] and 2 mm [80, 94, 95].

The extension to high-field ENDOR experiments has been realized at the 3 mm [60, 74, 96, 97] and 1 mm [98] microwave frequency bands. Whereas W-band high-field cw ENDOR was accomplished first in Berlin [96], high-field pulse ENDOR was accomplished first in Leiden [93, 99].

After these early years of high-field EPR spectroscopy, several groups continued and other groups started to build their dedicated high-field/high-frequency instrumentation. To give a few examples:

The research group of J. H. Freed at Cornell University was the first to push EPR instrumentation to far-infrared technology, and pioneered the use of quasioptical mw techniques in EPR. Details of their 250 GHz EPR spectrometer were published in 1988 [81]. The Cornell group also developed specially designed Fabry–Perot resonators for which high detection sensitivity was achieved even for aqueous biological samples [100]. The Frankfurt group of Thomas Prisner built a pulsed 180 GHz spectrometer with a quasioptical circulator and single-mode cavity; the instrument is designed for optional pulsed ENDOR and PELDOR experiments [101].

In 1989, the group of L.-C. Brunel at the Grenoble High-Magnetic-Field Laboratory realized an EPR system operating up to 525 GHz and magnetic fields up to 20 T [85]. A couple of years later, L.-C. Brunel moved to the National High Magnetic Field Laboratory (NHMFL), Tallahassee, Florida, where he, together with H. van Tol, developed a 25 Tesla cw EPR machine that can operate up to 700 GHz for a Lande factor $g = 2$ system [91, 102]. And around 2008, the research group of G. M. Smith and co-workers in St Andrews published their first spectacular results of their ambitious HIPER design concepts of a high-power, wideband 94 GHz spectrometer [103]. The HIPER instrumentation project, entitled “Bringing the NMR Paradigm to EPR”, was a top ranked research proposal in the UK and, later, turned into a UK high-field EPR facility [104]. This spectrometer has state-of-the-art sensitivity and is now a UK EPSRC facility and part of a European network on high-field EPR instrumentation and research. Commercially available EPR and ENDOR spectrometers are mostly operating at W-band frequencies. They were introduced at the end of the 1990s, the major manufacturer was, and still is, Bruker Biospin, Germany [105, 106]. Appropriate references to the laboratories which completed the construction of mm- and sub-mm high-field EPR spectrometers since the end of the 90s are included in recent overview articles, for instance [1, 29, 107–118].

Time-resolved EPR spectroscopy is an important issue in general, and under high-field conditions in particular. The arena of time-resolved high-field EPR was opened in 1989 by the first pulsed W-band EPR spectrometer built in the Schmidt group in Leiden [77, 99]. Soon after, T. F. Prisner and M. Rohrer in the Möbius group in Berlin completed a versatile pulsed EPR spectrometer at W-band, which served also for the first high-field echo-detected TREPR experiment on pulsed laser-generated transient radicals in photosynthetic reaction centers [60]. However, the introduction of time resolution capability of the sub-mm high-field EPR at 360 GHz with quasioptical microwave bridge had to wait until 2004. The design of this spectrometer in Berlin started with the cw mode of operation [87] using a solid-state 120 GHz

source with subsequent tripling. The 360 GHz output power at the Gaussian horn antenna is only 1 mW, thus limiting the B_1 field at the sample in the Fabry–Perot resonator to values too small for fast pulsing. As an unconventional novel approach to time-resolved sub-mm high-field EPR, a dedicated 360 GHz pulsed Orotron (''Oro'' refers to Russian abbreviations for ''open resonator plus reflecting grid'' in the high-voltage vacuum-tube generator) was constructed and integrated in the quasioptical microwave bridge of the heterodyne induction-mode EPR spectrometer in Berlin [119].

As mentioned above, under certain conditions, ESEEM can be a competitive alternative to ENDOR for measuring hyperfine and quadrupole interactions [56]. First successful W-band high-field ESEEM measurements of nitrogen hyperfine and quadrupole interactions in disordered powder samples were performed in Berlin in 1998 [120]. More recently, this work was largely extended by elaborate W-band ESEEM studies on nitroxide spin-label molecules to explore the sensitivity of the g-, hyperfine- and quadrupole-tensors for probing polarity and proticity effects of the solvent matrix [121].

In 2006/2007 pulsed high-field electron dipolar spectroscopy, specifically PELDOR or DEER, was introduced for resolving the relative orientation of weakly coupled biradical partners in a frozen-solution sample, in addition to measuring their distance. This extension of electron dipolar spectroscopy, established at X-band frequencies for determining large inter-radical distances (see recent overviews [122–124], to high frequencies and fields was accomplished independently by the group of T. F. Prisner (Frankfurt) [116, 125, 126] at 180 GHz, the group of G. Jeschke (Konstanz) [127] at 95 GHz and the group of K. Möbius (Berlin) at 95 GHz [128]. A more detailed chronological account of the landmark developments in advanced EPR spectroscopy and its multifrequency extensions can be found in [1].

Figure 5 shows the microwave and radiofrequency irradiation schemes of a variety of cw and pulse high-field EPR techniques that have been applied by various laboratories also at high Zeeman fields. Several of them are discussed in considerable detail in the present article.

Concluding this Introduction section, we point out that a major challenge of molecular biology, biochemistry, and biophysics is to understand function and reaction mechanism of highly specialized proteins on the level of their molecular and electronic structure. We take the view that the arsenal of modern EPR techniques in general, and of high-field EPR in particular, provides powerful and versatile tools highly needed for such an endeavor. The molecular information obtained is complementary to what can be learned from other biophysical techniques established in the field.

2 Principles of High-Field/High-Frequency EPR

In the following, we present a rather phenomenological description of the theoretical principles of EPR techniques that stood the test for high-field applications in biophysics and biochemistry. For a more in-depth theoretical treatment of advanced EPR spectroscopy we refer to renowned textbooks, for example [1, 33, 58, 129,

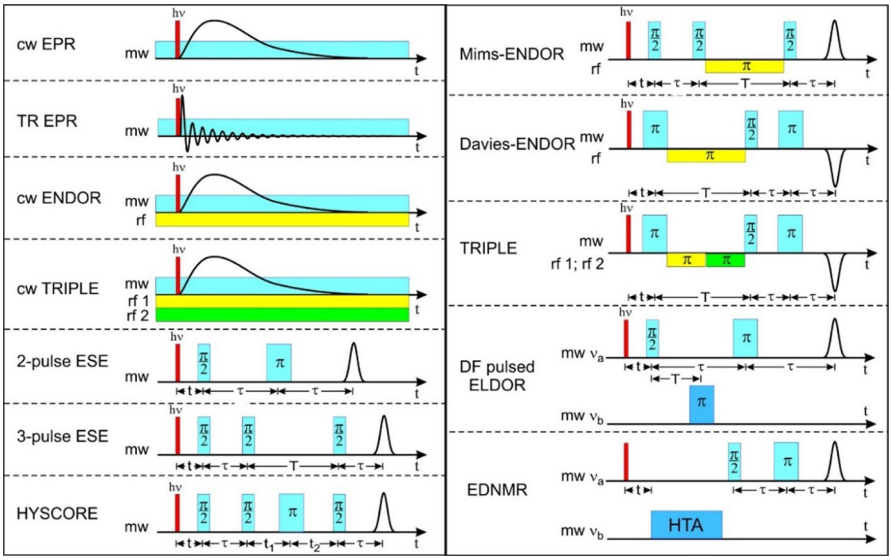

Fig. 5 Microwave (mw) and radiofrequency (rf) cw and pulse irradiation schemes of various time-resolved EPR techniques. The initial laser excitation pulse $h\nu$ starts the photoreaction with paramagnetic intermediates. For stable paramagnetic systems, the laser pulse is omitted. *cw* continuous wave, *TR* transient, *ENDOR* electron–nuclear double resonance, *TRIPLE* electron–nuclear–nuclear triple resonance, *ESE* electron spin echo, *HYSCORE* hyperfine sublevel correlation spectroscopy, *DF* dual frequency, *pulsed ELDOR* PELDOR: pulsed electron–electron double resonance, *EDNMR* ELDOR-detected NMR, *HTA* high turning angle. For details, see text and [1]. In this ref., additional pulse irradiation schemes of various time-resolved EPR techniques are discussed

130]. We also refer to rather recent overview articles on high-field/high-frequency EPR in the biosciences [107–110, 115, 116, 118, 131–136]. We will focus on high-field EPR studies of biochemical systems that were performed in our laboratory at FU Berlin in teamwork with undergraduate and graduate students, postdocs and senior scientists from over the world.

2.1 Spin Hamiltonians for EPR at High Magnetic Fields

We first describe the basic spin Hamiltonians with interaction terms that determine the energy levels and EPR transition frequencies and, thereby, the characteristic features of the EPR spectrum of an open-shell system.

2.1.1 Organic Radicals and Low-Spin Transition-Metal Ions ($S = 1/2$)

In molecular radicals or transition-metal ion complexes with unpaired electron spins $S = 1/2$, the electron and nuclear spins will align with respect to the total magnetic field they experience. This is the vector sum of the external Zeeman field, $\vec{B}_0$, the local field originating from the residual orbital angular momentum of the unpaired electron and spin–orbit coupling (leading to effective g-tensor

components shifted from the free-electron value), and the additional local hyperfine and quadrupole fields from nearby magnetic nuclei. For example, ^{14}N nuclei with $I = 1$ or protons, ^{1}H, with nuclear spin $I = 1/2$. They are located in the radical molecule or in the solvent micro-environment of the radical (''matrix'' nuclei).

For such $S = 1/2$ systems, the static spin Hamiltonian, $\widehat{H}_0$, that describes the time-independent spin-interaction energies, consists of the terms

$$\frac{\widehat{H}_0}{h} = \frac{\mu_B}{h} \cdot \vec{B}_0 \cdot \widetilde{g} \cdot \widehat{S} - \sum_i g_{ni} \cdot \frac{\mu_N}{h} \cdot \vec{B}_0 \cdot \widehat{I}_i + \sum_i \widehat{S} \cdot \widetilde{A}_i \cdot \widehat{I}_i + \sum_i \widehat{I}_i \cdot \widetilde{P}_i \cdot \widehat{I}_i, \quad (2)$$

i.e., $\widehat{H}_0$ contains the field-dependent electron and nuclear Zeeman interactions as well as the field-independent electron–nuclear hyperfine and nuclear quadrupole interactions with magnetic nuclei (for the quadrupole interaction to exist, nuclei with $I > 1/2$ in an asymmetric electronic environment are required). Here, $\vec{B}_0$ is the external magnetic field (a vector), $\widetilde{g}$, $\widetilde{A}$ and $\widetilde{P}$ are the corresponding interaction tensors (matrices) of the electron Zeeman, hyperfine and quadrupole interactions (h: Planck constant; μ_B and μ_N: Bohr and nuclear magnetons; g_n: nuclear g-factors; $\widehat{S}$, $\widehat{I}$: electron and nuclear spin vector operators; the summation is over all nuclei).

The quadrupole interaction between a nuclear electric quadrupole moment, Q, and an electric field gradient at the position of the nucleus is described by the spin Hamiltonian $\widehat{I} \cdot \widetilde{P} \cdot \widehat{I}$. In its principal axes system, the quadrupole tensor, $\widetilde{P}$, is traceless, and the quadrupole Hamiltonian can be written as

$$\frac{\widehat{H}_Q}{h} = P_{xx} \cdot \widehat{I}_x^2 + P_{yy} \cdot \widehat{I}_y^2 + P_{zz} \cdot \widehat{I}_z^2 = \frac{e^2 \cdot q \cdot Q}{4I \cdot (2I-1) \cdot h} \cdot \left[3 \cdot \widehat{I}_z^2 + 2I(I+1) + \eta \cdot \left(\widehat{I}_x^2 - \widehat{I}_y^2\right)\right], \quad (3)$$

where $e \cdot q$ is the electric field gradient of the electron plus nuclear charge distribution along the z-direction, and $\eta = (P_{xx} - P_{yy})/P_{zz}$ is the asymmetry parameter of the charge distribution with $|P_{zz}| \geq |P_{yy}| \geq |P_{xx}|$ and $0 \leq \eta \leq 1$ [33, 130]. The largest principal value of the quadrupole tensor is given by $P_{zz} = \frac{e^2 \cdot q \cdot Q}{2I \cdot (2I-1) \cdot h}$.

Commonly, the quadrupole-tensor components for any given value $I \geq 1$ are characterized by the two quantities $e^2 \cdot q \cdot Q/h$ (in linear frequency units) and η; for quantifying the magnitude of the interaction the factor $2I(2I-1)$ has to be included.

The dipolar hyperfine interaction between an electron and a nuclear spin, $\widehat{S} \cdot \widetilde{A} \cdot \widehat{I}$ in Eq. (2), can be written as the sum of the isotropic (or Fermi contact) interaction, $\frac{\widehat{H}_{Fermi}}{h} = A_{iso}\, \widehat{S} \cdot \widehat{I}$; with (in SI units)

$$A_{iso} = \frac{2\mu_0}{3h} \cdot g_e \cdot \mu_B \cdot g_n \cdot \mu_N \cdot |\Psi(0)|^2, \quad (4)$$

and the anisotropic dipole–dipole interaction between the magnetic moments of the electron and nuclear spins (END interaction)

$$\frac{\widehat{H}_{SI}}{h} = \frac{\mu_0}{4\pi \cdot h} \cdot g_e \cdot \mu_B \cdot g_n \cdot \mu_N \cdot \left[\frac{3\left(\widehat{S} \cdot \vec{r}\right)\left(\vec{r} \cdot \widehat{I}\right)}{r^5} - \frac{\widehat{S} \cdot \widehat{I}}{r^3} \right], \tag{5}$$

where μ_0 is the vacuum permeability, $|\Psi(0)|^2$ the electron density at the nucleus, r is the distance between the electron and nuclear spins, g_e is the free-electron g-factor.

For nucleus i, the Hamiltonian of the anisotropic part of the electron–nuclear hyperfine interaction, the electron–nuclear dipolar (END) term, $\widehat{H}_{SI}$, can be written as [137]

$$\frac{\widehat{H}_{SI}}{h} = \frac{\mu_0}{4\pi \cdot h} \cdot g_e \cdot \mu_B \cdot g_n \cdot \mu_N \cdot (A + B + C + D + E + F). \tag{6}$$

The six terms A, B, C, D, E, F represent products of electron and nuclear spin operators and angular functions in spherical coordinates with the polar angles θ and φ describing the orientation between the dipolar axis and the external Zeeman field $\vec{B}_0$:

$$\begin{aligned}
A &= \widehat{S}_z \cdot \widehat{I}_z \cdot \left(3\cos^2\theta - 1\right), \\
B &= \tfrac{1}{4} \cdot \left(\widehat{S}_+ \cdot \widehat{I}_- + \widehat{S}_- \cdot \widehat{I}_+\right) \cdot \left(3\cos^2\theta - 1\right), \\
C &= \tfrac{2}{3} \cdot (\widehat{S}_+ \cdot \widehat{I}_z + \widehat{S}_z \cdot \widehat{I}_+) \cdot \sin\theta \cdot \cos\theta \cdot e^{-i\varphi}, \\
D &= \tfrac{2}{3} \cdot \left(\widehat{S}_- \cdot \widehat{I}_z + \widehat{S}_z \cdot \widehat{I}_-\right) \cdot \sin\theta \cdot \cos\theta \cdot e^{i\varphi}, \\
E &= \tfrac{3}{4} \cdot \widehat{S}_+ \cdot \widehat{I}_+ \cdot e^{-2i\varphi}, \\
F &= \tfrac{3}{4} \cdot \widehat{S}_- \cdot \widehat{I}_- \cdot e^{2i\varphi}.
\end{aligned} \tag{7}$$

Here, the x- and y-components of the spin operators are expressed in terms of the raising and lowering shift operators. Depending on the specific way these spin operators are acting on a state of the unperturbed Hamiltonian (the electron Zeeman interaction, being the leading term in X-band EPR and even more so in high-field EPR) the A, B, C, D, E, F terms are classified as secular (A term), pseudo-secular (B term) and non-secular (C, D, E, F terms). Only the secular and pseudo-secular parts in the END term contribute in first order to the dipolar splitting of the unperturbed energy levels. In EPR (or NMR or ENDOR), the coherent microwave (or radiofrequency) fields are normally applied in a direction perpendicular to the static external Zeeman field so that the selection rules $\Delta m_S = \pm 1$, $\Delta m_I = \pm 1$ hold. As a consequence, the non-secular terms are unimportant for determining the line positions of the spectra to first-order perturbation theory. Higher-order satellites due to small state admixtures will have vanishingly small intensities as long the Zeeman terms are much larger than the C, D, E, F terms. This does not mean, however, that the non-secular END parts, when becoming time dependent, are unimportant for the electron and nuclear relaxation pathways. They are induced by the pertaining randomly fluctuating local fields, for instance owing to Brownian motion of the radicals in liquid-state samples. Then, the time-dependent non-secular interactions induce

relaxation transitions of the electron spins (W_e) and nuclear spins (W_n) as well as coupled ''flop-flop'' cross-relaxation transitions (W_{x2}).

The tensors $\widetilde{g}$, $\widetilde{A}$, and $\widetilde{P}$ of the electron Zeeman interaction, the hyperfine interaction, and the quadrupole interaction probe the electronic structure (i.e., the electron wave function and energy) of the molecule either globally (g-tensor) or locally (hyperfine- and quadrupole-tensors). The g- and A-tensors contain isotropic and anisotropic contributions, whereas the P-tensor is traceless, i.e., contains only anisotropic contributions. In isotropic fluid solution at temperatures high enough for fast molecular tumbling, the anisotropic interaction components are averaged out so that only the isotropic values, $1/3 \cdot Tr(\widetilde{g})$ and $1/3 \cdot Tr(\widetilde{A}_i)$, contribute to the observed line positions. In frozen solutions, powders or single crystals, also anisotropic tensor contributions become observable, providing that the necessary spectral resolution conditions prevail, i.e., the separations of the lines are larger than their linewidths. For this situation, the information content of the EPR spectra is, of course, considerably enhanced by spatial information and, for example, molecular orientations with respect to $\vec{B}_0$ or electron–nuclear distances can be extracted.

In the strong-field approximation, the energy eigenvalues of Eq. (2) are classified by the magnetic spin quantum numbers, m_S and m_I, and are given (without quadrupole contribution), to first order (in frequency units) by

$$\frac{E(m_S, m_I)}{h} = \frac{g \cdot \mu_B}{h} \cdot B_0 \cdot m_S - \sum_i \frac{g_{ni} \cdot \mu_N}{h} \cdot B_0 \cdot m_{I_i} + \sum_i A_i \cdot m_S \cdot m_{I_i}, \qquad (8)$$

where the scalar interaction parameters g, A are the square root values of the squared tensors and contain the desired information about magnitude and orientation of the interaction tensors [130]. To keep the energy expression simple, the contributions due to the quadrupole interaction, P, are omitted for the moment. In thermal equilibrium between the spin system and the lattice, the energy levels are populated according to the Boltzmann distribution. When irradiating the sample with microwaves at a fixed frequency and sweeping the external field through the resonance region, EPR transitions occur according to the first-order selection rules $\Delta m_S = \pm 1$, $\Delta m_{I_i} = 0$. This leads to an EPR spectrum of absorption lines that is characteristic for the electron spin interactions of the sample molecules. The intensity distribution of the hyperfine lines is determined by the number of symmetry-equivalent nuclei. Hence, the intensity ratio of the hyperfine lines is a valuable aid for assigning the lines to specific nuclear positions in the molecule. From Eq. (8) it follows that the purely nuclear spin interactions, i.e., the nuclear Zeeman and quadrupole interactions, do not show up in the EPR spectrum as long as the first-order approximation for the selection rules holds. Second-order contributions from the nuclear Zeeman and quadrupole energy terms can often be neglected (see Fig. 2). However, this is only justified as long as the nuclear spin terms are considerably smaller than the other two terms. This might be no longer the case at high Zeeman fields or for substantial quadrupole couplings.

As a simple example, a doublet radical ($S = 1/2$) is considered, containing four symmetry-equivalent protons (each with $I = 1/2$) in a strong B_0 field. Figure 6 shows the energy level scheme according to Eq. (8) for the case that the radical is

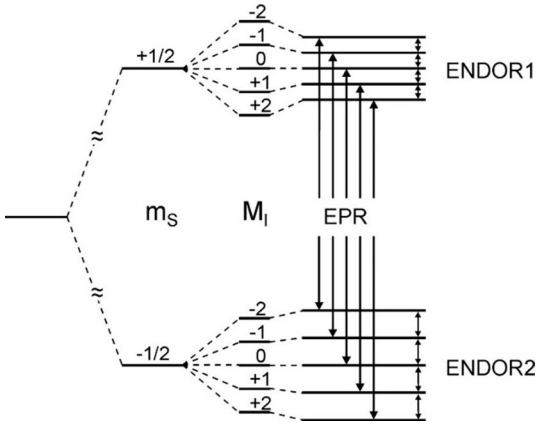

Fig. 6 High-field spin energy levels of a radical ($S = 1/2$) with a group of four equivalent protons ($I = 1/2$) dissolved in fluid solution. The allowed EPR and ENDOR transitions are marked by arrows. The energy splittings are drawn according to Eq. (8) with $A > 0$. The total nuclear quantum number of the group is $M_i = \sum_i m_{I_i}$.

dissolved in isotropic fluid solution. In this situation, only scalar interactions prevail provided that fast molecular tumbling occurs. As a consequence of the strong-field EPR selection rules, five EPR lines are observed with binominal intensity distribution owing to the first-order transition-frequency degeneracies of equivalent nuclei. Their isotropic hyperfine coupling constant (hfc) $A_{iso} = 1/3 \cdot Tr(\widetilde{A}_i)$ can be directly read off from the separation of the hyperfine lines in the EPR spectrum.

For single-crystal samples of the same radical, the complete g- and hyperfine-tensor information, i.e., both the isotropic and anisotropic contributions, can be extracted from the angular dependence of the EPR lines ("rotation patterns") when the crystal is rotated about three orthogonal axes. Note that there exists no quadrupole interaction with protons or other nuclei with $I = 1/2$. If the tensors $\widetilde{g}$ and $\widetilde{A}_i$ are collinear, i.e., have the same principal axes system (α, β, γ), their rotation patterns will have the same angular dependence. When the crystal is mounted on a proper wedge in such a way that the crystal rotation axes are parallel to the molecular axes system (x, y, z) and remain under rotation perpendicular to the B_0 field direction, the actual rotation occurs in a molecular plane defining an angle Θ between the rotation axis and the field direction. Iterated measurements of the angular dependence of the apparent g- and A-values at different orientations give the elements of the tensors $\widetilde{g}^2$ and $\widetilde{A}^2$, which can be transformed to principal axes. One could begin by rotating the field in the xy plane, followed by rotations in the yz and zx planes. Then, the dependence of the apparent g-value on the rotation angle Θ_{ij} in the ij plane takes the form [130, 138] (notice that g_{ij}^2 denotes the components of the squared g-tensor):

$$g(\Theta_{xy}) = \left(g_{xy}^2 \cdot \sin^2\Theta_{xy} + g_{yy}^2 \cdot \cos^2\Theta_{xy} + g_{xy}^2 \cdot \sin 2\Theta_{xy} \right)^{1/2}. \tag{9}$$

An analogous expression holds for the hyperfine coupling value A_i of nucleus i in the limit of small g-anisotropy, as is typical for bioorganic systems as long as they do not contain paramagnetic transition-metal ions. For the other two molecular planes, yz and zx, the corresponding tensor components are found by cyclic replacement $y \to z \to x \to y$, i.e.,

$$g(\Theta_{yz}) = \left(g_{yy}^2 \cdot \sin^2\Theta_{yz} + g_{zz}^2 \cdot \cos^2\Theta_{yz} + g_{yz}^2 \cdot \sin 2\Theta_{yz}\right)^{1/2}, \tag{10}$$

$$g(\Theta_{zx}) = \left(g_{zz}^2 \cdot \sin^2\Theta_{zx} + g_{xx}^2 \cdot \cos^2\Theta_{zx} + g_{zx}^2 \cdot \sin 2\Theta_{zx}\right)^{1/2}, \tag{11}$$

with the rotation angles Θ_{ij} defined as the respective angles between the i- and j-axis and the field direction.

For many bioorganic samples, in particular in frozen solution, conventional X-band EPR runs into problems with spectral resolution. This is because several radical species or different magnetic sites with rather similar g-values may be present or because a small g-tensor anisotropy does not allow canonical orientations of the powder spectrum to be resolved. From the spin Hamiltonian Eq. (2) one sees that some interactions are magnetic field-dependent (the Zeeman interactions), while others are not (the hyperfine and quadrupole interactions). Consequently, if paramagnetic species with different g-factors or with anisotropic g-tensor components are present, the difference in resonance field positions ΔB_0 is proportional to the frequency of the electromagnetic irradiation:

$$\Delta B_0 = \frac{h \cdot \nu}{\mu_B} \cdot \left(\frac{1}{g_1} - \frac{1}{g_2}\right). \tag{12}$$

This shows, in analogy to modern NMR spectroscopy, that higher mw EPR frequencies, ν, and corresponding resonance fields, B_0, should lead to enhanced spectral resolution, at least as long as the linewidths do not increase with field. Except for transition-metal complexes, for many bioorganic systems $g \cong 2$, and relative g-value variations $\Delta g/g$ rarely exceed $10^{-4} - 10^{-3}$. At X-band frequencies, therefore, the line separation due to g-value differences is only $\Delta B_0 = 0.03 - 0.3$ mT, which can easily be masked in disordered solid-state samples with typical linewidths around 1 mT. An increase of the mw frequency by, for instance, a factor of 10 (W-band, 95 GHz) improves the spectral resolution accordingly. This is a consequence of the increasing importance of the g-tensor components in the electronic Zeeman interaction as the magnetic field is increased. Moreover, the spectral analysis is generally simpler in high-field EPR because the first-order approximation for the energies often applies.

The question arises, how large the Zeeman field ought to be for maximum spectral information for a particular sample? The answer for all cases of delocalized spin systems, in which unresolved hyperfine interactions dominate the inhomogeneous EPR linewidth, is that a successful high-field experiment must fulfill the condition

$$\frac{\Delta g}{g} \cdot B_0 > \Delta B_{1/2}^{hf}, \tag{13}$$

which relates the Zeeman field B_0 of the spectrometer with properties of the sample, i.e., the anisotropic electron Zeeman interaction must exceed the inhomogeneous linewidth, $\Delta B_{1/2}^{hf}$. Apparently, there are two options to fulfill this condition, either to make the Zeeman interaction large enough or to reduce the linewidth sufficiently.

Hence, instead of fixing a minimum field/frequency value to meet the ''high-field EPR'' benchmark, one should ensure that the chosen B_0 value renders the Zeeman splitting to be larger than the inhomogeneous linewidth. Nevertheless, it has become common practice in the EPR community to use the term ''high-field EPR'' for microwave frequencies in the W-band or higher and Zeeman fields produced by superconducting magnets. For example, for deuterated samples, Q-band EPR might already fulfill the high-field condition Eq. (13) in the case of semiquinone radicals with a rather large g-anisotropy [139–141], whereas for protonated samples with inherently larger linewidths, it does not. On the other hand, in the case of chlorophyll ion radicals, due to their very small g-anisotropy, even W-band EPR might not meet the high-field condition for protonated samples. Then deuteration of the sample will be necessary or, as an alternative, a further increase of the mw frequency and B_0 field is required, for instance by resorting to 360 GHz EPR. Fortunately, for many protein systems with no paramagnetic transition-metal ion sites or, at least, no substantial spin density at such a site, the increase of line separation ΔB_0 with increasing Zeeman field directly translates into an increase of spectral resolution, because often no noticeable line broadening due to ''g-strain'' effects occurs with increasing B_0. For the primary donor cation radical in reaction centers (RCs) from Rb. sphaeroides, for example, up to 24 T were applied [142], and g-strain broadening was found to be negligible.

The term ''g-strain'' is used to describe a spread of principal g-factors caused by heterogeneities of the local environment of the spins and leading to additional line broadening that increases linearly, or approximately linearly with the Zeeman field. This phenomenon is well known in the case of paramagnetic transition-metal complexes such as metallo-proteins [143, 144] where large spin–orbit coupling can produce dramatic variations in the g-values with varying crystal fields. Such effects are, however, expected to be small in the case of organic radicals in proteins for which small g-anisotropies are the rule. Apparently, the primary donor cation radical in RCs from Rb. sphaeroides is not an exception of this rule.

In addition to the improved g-resolution mentioned above, high-field EPR can also improve the detection sensitivity. In this respect one has to distinguish between the absolute and relative (or concentration) sensitivities because the amount of sample that can be introduced into the cavity of high-field EPR spectrometers is usually significantly smaller than in standard X-band spectrometers. Consequently, the amount of sample available must be considered. When this is limited like in single crystals of proteins, the sensitivity of high-field EPR can be superior by orders of magnitude. For a quantitative discussion of the sensitivity problems, we refer to [1].

2.1.2 Triplet States and High-Spin Transition-Metal Ions ($S > 1/2$)

Also for high-spin systems ($S > 1/2$), such as enzymatic proteins with one or several transition-metal cofactors, EPR spectroscopy at high magnetic fields might be advantageous. For such systems "fine-structure" and exchange terms have to be added to the spin Hamiltonian, i.e., Eq. (2) has to be extended by

$$\frac{\widehat{H}_{ZFS}}{h} + \frac{\widehat{H}_{exchange}}{h} = \widehat{S} \cdot \widetilde{D} \cdot \widehat{S} - J \cdot \left(\widehat{S}^2 - 1\right), \tag{14}$$

with the total spin $S = (S_1 + S_2 + \dots)$. Here, $\widetilde{D}$ is the traceless zero-field splitting (ZFS) tensor, and J is the isotropic exchange interaction parameter (in standard convention, $J < 0$ corresponds to antiferromagnetic coupling, $J > 0$ to ferromagnetic coupling). In the principal axes system of $\widetilde{D}$, the anisotropic part in Eq. (14) is normally rewritten in terms of the zero-field parameters D, E:

$$\frac{\widehat{H}_{ZFS}}{h} = \widehat{S} \cdot \widetilde{D} \cdot \widehat{S} = D \cdot \left(\widehat{S}_z^2 - \frac{1}{3} \cdot S \cdot (S+1)\right) + E\left(\widehat{S}_x^2 - \widehat{S}_y^2\right), \tag{15}$$

with $D = 3/2 \cdot D_{zz}$ and $E = \left(D_{xx} - D_{yy}\right)/2$, where D_{xx}, D_{yy} and D_{zz} are the principal values of the ZFS tensor. For a triplet state, they are related to the zero-field energy eigenvalues (energy levels) of the triplet spin eigenfunctions$|T_x\rangle$,$|T_y\rangle$, $|T_z\rangle$ as follows [138]:

$$E_x/h = \frac{1}{3} \cdot D - E, E_y/h = \frac{1}{3} \cdot D + E, E_z/h = -\frac{2}{3} \cdot D. \tag{16}$$

Obviously, it might happen that EPR transitions of high-spin systems with large zero-field splitting cannot be observed at all at standard X-band frequencies because the energy of the mw quantum is too small. For such cases, the higher quantum energy of high-frequency microwaves can drive the transitions [145, 146]. An example for such a biological high-spin system is metmyoglobin with $S = 5/2$ ferric heme, for which EPR transitions at 130 GHz became observable that had been undetectable at X-band due to the large zero-field splitting [88].

Although in the spin Hamiltonian the fine-structure term is not field-dependent it leads, in combination with the electronic Zeeman term, to a field-dependent mixing of the electron spin eigenfunctions. At zero field, the triplet spin eigenfunctions, $|T_x\rangle, |T_y\rangle, |T_z\rangle$, are quantized along the molecular axes system (x, y, z). At high field, the magnetic spin quantum number, $m_S = +1, 0, -1$, is a good quantum number, and the spin eigenfunctions become $|T_{+1}\rangle, |T_0\rangle, |T_{-1}\rangle$. If the external field values B_0 are such that the electron Zeeman and the fine-structure splitting are comparable in magnitude, the spin functions become mixed functions of both bases, the degree of mixing depending on B_0 and the relative orientation of the molecule with respect to the field. As a consequence, the triplet energy eigenvalues of the different electron wave functions are not linearly related to the strength of B_0. This intermediate region requires more complicated calculations to analyze the EPR spectrum. Hence, for high-spin systems ($S > 1/2$), there is another reason for choosing EPR at high Zeeman field, which is to simplify the analysis of spectra.

There is an additional benefit: The EPR lines of high-spin systems usually get narrower at higher magnetic fields than in X-band EPR spectra, again because of second-order effects. If we take Mn^{2+} centers ($S = 5/2, I = 5/2$) in disordered protein samples as an example, the EPR transitions are strongly broadened by contributions from the zero-field tensor components. Their linewidth, $\Delta B_{1/2}$, is determined

by second-order contributions from the zero-field coupling D, $\Delta B_{1/2} \propto \frac{D^2}{B_0}$. No wonder, therefore, that "needle sharp" manganese hyperfine lines are normally observed in the 95 GHz high-field EPR spectra of Mn^{2+} containing protein complexes, such as photosystem II of oxygenic photosynthesis, even in disordered frozen-solution samples.

This is exploited by high-field EPR spectroscopists who use Mn^{2+} ions doped into MgO powder as reference sample for magnetic field calibration and precise g-factor measurements [74]. Up to second order, the EPR resonance fields of the six Mn^{2+} hyperfine components,$m_I = 5/2, ... + 5/2$, are given by

$$B_{m_I} = B_0 - A_{iso} \cdot \left[m_I - \frac{A_{iso}}{2B_0} \cdot \left(I \cdot (I-1) - m_I^2 \right) \right], \tag{17}$$

where A_{iso} is the isotropic Mn^{2+} hyperfine coupling in field units. The electronic g-factor is contained in the Zeeman field $B_0 = F \cdot \nu / g$ (ν frequency, $F = h/\mu_B$= 71.447751 mT·GHz^{-1}). The high-precision reference data are: g (Mn^{2+}) = 2.00101 ± 0.00005 and A_{iso}(Mn^{2+}) = − (8.710 ± 0.003) mT [74].

To underline it once again: High-field EPR is particularly useful for half-integer high-spin systems ($S = (2n+1)/2, n = 1, 2, ...$), such as Mn(II) and Fe(III) with $S = 5/2$, and Gd(III) with $S = 7/2$. For such systems the inhomogeneous linewidth of orientationally disordered samples, $\Delta B_{1/2}$, of the central $|-1/2 \rightarrow |1/2$ EPR transition is determined by second-order contributions from the zero-field coupling. Hence, when $g \cdot \mu_B \cdot \frac{B_0}{h} \gg D$ the broadening becomes negligible and narrow signals are obtained also in orientationally disordered samples. This leads to increased sensitivity and resolution. In this case the first-order approximation is valid and the resonance fields are given by:

$$B\left(m_S \rightarrow m_S + 1\right) = B_0 - \frac{h}{g \cdot \mu_B} \cdot A_{iso} \cdot m_I + \frac{h}{g \cdot \mu_B} \cdot \left(2m_S + 1\right) \cdot \nu_D$$

$$\nu_D = \frac{D}{2} \cdot \left[\left(3\cos^2\theta - 1 \right) + \eta \cdot \sin^2\theta \cdot \cos 2\varphi \right], \tag{18}$$

where A_{iso} is the isotropic hyperfine coupling of ^{55}Mn (in frequency units), m_I is the corresponding nuclear spin projection and $\eta = 3 \cdot E/D$. The angles θ and φ describe the orientation of the magnetic field relative to the principal axes system of the ZFS tensor.

Another important aspect of high-field EPR on high-spin systems, for example organic triplet states and radical pairs with $S = 1$, is the possibility to determine the absolute sign of the zero-field parameter D by sufficient thermal polarization of the triplet levels already at moderately low temperatures [22, 23]. If the temperature is low enough to fulfill the condition $k_B T < g \cdot \mu_B \cdot B_0$, the lowest spin level, corresponding to $m_S = -1/2$, is predominantly populated, and the EPR spectra of disordered samples become asymmetric. The ''Zeeman temperature'', $T_Z = g \cdot \mu_B \cdot B_0 / k_B$, is defined accordingly as the temperature around which this asymmetry becomes pronounced: A higher line intensity is observed either on the

high-field side ($D > 0$) or on the low-field side ($D < 0$) of the spectrum. Approximate values of the Zeeman temperature at different EPR frequencies are: $T_Z = 0.4$ K (at 9.5 GHz), 4 K (at 95 GHz), 6.5 K (at 140 GHz), and 15.5 K (at 360 GHz). The sign of D is indicative of the shape of the dipolar tensor. Organic triplet states generally have disk-shaped dipolar tensors ($D > 0$), whereas weakly coupled radical pairs have cigar-shaped ones ($D < 0$).

2.2 High-field ENDOR, TRIPLE, ESEEM, HYSCORE, EDNMR, PELDOR, RIDME

We now turn to several extensions of high-field/high-frequency EPR spectroscopy in some more detail to clarify what can be learned additionally about (bio)chemical and biological systems when going beyond conventional X-band techniques. The topics selected are ENDOR, TRIPLE, ESEEM, HYSCORE, EDNMR, PELDOR, and RIDME. We will group these techniques under two headings: Electron–nuclear hyperfine spectroscopy; Electron–electron dipolar spectroscopy.

2.2.1 Electron–Nuclear Hyperfine Spectroscopy

Thorough accounts of high-field/high-frequency ENDOR and TRIPLE spectroscopy have recently been published, and we suggest them for further reading [1, 118, 147, 148].

2.2.1.1 cw ENDOR For large low-symmetry radicals with the unpaired electron delocalized over many spin-carrying nuclei, for example the cofactor ion radicals occurring in photosynthetic electron transfer, with each set of inequivalent nuclei the number of EPR lines increases in a multiplicative way, according to the EPR selection rules $\Delta m_S = \pm 1, \Delta m_{I_i} = \pm 1$. This results in strong inhomogeneous broadening of the EPR spectra because individual hyperfine lines can no longer be resolved in the available spectral range. For $g = 2$ systems, this is restricted to ca. 3 mT due to the normalization condition for the unpaired electron spin density.

For such cases, by resorting to ENDOR techniques the spectral resolution can be greatly improved. This is because ENDOR is inherently a variant of NMR on paramagnetic systems, the unpaired electron serving as highly sensitive detector for the NMR transitions, $m_{I_i} = \pm 1$. Each group of equivalent nuclei—no matter how many nuclei are involved and of what value their individual nuclear spin is—contributes only two ENDOR lines at $\nu^{\pm}$ because, within an m_S manifold, the hyperfine levels are equidistant to first order (see Fig. 6). Hence, in ENDOR, with each set of inequivalent nuclei the number of resonance lines increases merely in an additive way. Double resonance excitation, thus, offers the advantage of NMR in terms of high resolution via reduced number of redundant hyperfine lines in conjunction with the advantage of EPR in terms of detecting low-intensity rf transitions via high-intensity mw transitions, i.e., by means of quantum transformation via the gyromagnetic ratios.

In cw ENDOR, the sample is irradiated simultaneously by two electromagnetic fields, a mw field (to drive EPR transitions $\Delta m_S = \pm 1$) and an rf field (to drive NMR

transitions $\Delta m_{I_i} = \pm 1$). Under appropriate experimental conditions, which are more stringent for cw than for pulse irradiation schemes [33, 129, 149], ENDOR signals are observed by monitoring the changes of EPR line intensities when sweeping the rf field through the nuclear resonance frequencies. In cw Special TRIPLE resonance [48] the two rf fields are applied at frequencies symmetrically placed around the nuclear Larmor frequency to enhance the signal intensity. In cw General TRIPLE resonance [52], two rf fields with independently variable frequencies are applied, one pumping a selected ENDOR transition while the other is swept through the ENDOR spectrum. From the resulting characteristic intensity changes in the ENDOR spectrum, the relative signs of the hyperfine couplings can directly be read off.

In the pulsed version of triple resonance [150], the first rf pulse (pump pulse) with fixed frequency pumps a specific nuclear transition, while the frequency of the second rf pulse is swept to cover the resonance region**.** The time separation between the two rf pulses can be varied. Again, assignment of hyperfine couplings and determination of their relative signs are the main goals. When the frequencies of the two rf pulses are varied independently, a two-dimensional triple resonance spectrum is obtained [151].

Apparently, the gain in resolution of ENDOR versus EPR, becomes very pronounced for low-symmetry molecules with increasing number of groups of symmetry-related nuclei. The resolution enhancement becomes particularly drastic when nuclei with different magnetic moments are involved. Their ENDOR lines appear in different frequency ranges and, providing that their Larmor frequencies are separated at the chosen Zeeman field value B_0, the different nuclei can be immediately identified. In the case of an accidental overlap of ENDOR lines from the different nuclei at X-band (9.5 GHz, 0.34 T) the lines can be separated when working at higher Zeeman fields and mw frequencies, for instance at 3.4 T, 95 GHz [96] or even at 12.9 T, 360 GHz [152]. This disentangling of ENDOR lines by different field/frequency settings for the EPR condition is depicted in Fig. 7. In biological molecules with several non-proton magnetic nuclei this separation of accidentally overlapping ENDOR lines is of great help for analyzing complex spin systems by means of their nuclear Zeeman and hyperfine interactions.

In the pulsed version of triple resonance [150], the first rf pulse (pump pulse) with fixed frequency pumps a specific nuclear transition, while the frequency of the second rf pulse is swept to cover the resonance region**.** The time separation between the two rf pulses can be varied. Again, assignment of hyperfine couplings and determination of their relative signs are the main goals. When the frequencies of the two rf pulses are varied independently, a two-dimensional triple resonance spectrum is obtained [151].

Apparently, the gain in resolution of ENDOR *versus* EPR, becomes very pronounced for low-symmetry molecules with increasing number of groups of symmetry-related nuclei. The resolution enhancement becomes particularly drastic when nuclei with different magnetic moments are involved. Their ENDOR lines appear in different frequency ranges and, providing that their Larmor frequencies are separated at the chosen Zeeman field value B_0, the different nuclei can be immediately identified. In the case of an accidental overlap of ENDOR lines from the different

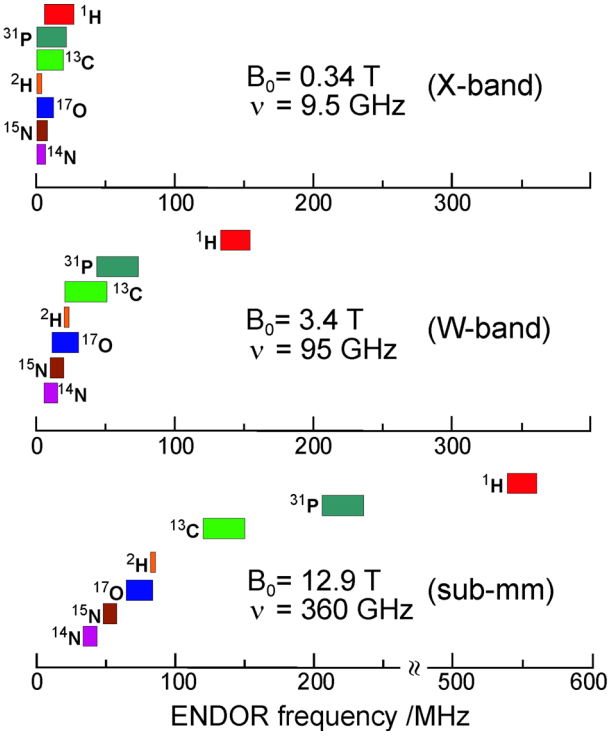

Fig. 7 Gain in ENDOR resolution for doublet-state systems ($S = 1/2, g = 2$) with increasing Zeeman field B_0 and corresponding microwave resonance frequency ν. Spectral lines of typical nuclei in organic biomolecules, largely overlapping at traditional X-band ENDOR ($B_0 = 0.34$ T, $\nu = 9.5$ GHz), become completely separated at 360 GHz/12.9 T ENDOR

nuclei at X-band (9.5 GHz, 0.34 T) the lines can be separated when working at higher Zeeman fields and mw frequencies, for instance at 3.4 T, 95 GHz [96] or even at 12.9 T, 360 GHz [152]. This disentangling of ENDOR lines by different field/frequency settings for the EPR condition is depicted in Fig. 7. In biological molecules with several non-proton magnetic nuclei this separation of accidentally overlapping ENDOR lines is a great help for the analysis of complex spin systems by means of their nuclear Zeeman and hyperfine interactions.

For a doublet radical with electron–nuclear hyperfine interaction, but without nuclear quadrupole interactions, according to its spin Hamiltonian only two ENDOR lines of a particular group of equivalent nuclei with $I = 1/2$, appear, to first order, at

$$\nu^{\pm}_{ENDOR} = |\nu_n \pm A_{i/2}|, \tag{19}$$

where the nuclear Larmor frequency is given by $\nu_n = g_n \cdot \mu_N \cdot B_0/h$, and the hyperfine coupling parameter A contains isotropic and anisotropic contributions. Obviously, the two ENDOR lines are symmetrically displayed about ν_n or $A/2$, whichever is larger. In isotropic solution, in steady-state ENDOR, the hyperfine couplings (hfcs) are given by $A_{iso} = 1/3 \cdot Tr(\widetilde{A})$.

At this point, it seems appropriate to give a brief phenomenological explanation of liquid-phase cw steady-state ENDOR signal intensities and their alteration by applying a second rf field in TRIPLE resonance experiments. In isotropic liquid solution, at sufficiently elevated temperatures, the anisotropic contributions of the g-tensor are effectively averaged out. Nevertheless, EPR and ENDOR studies at higher frequency/field settings than for standard X-band EPR can be of great advantage: If in the sample several radical species with only slightly different isotropic g-values are present, for example as intermediate or final reaction products with g_1 and g_2, they can be spectroscopically resolved and identified at sufficiently high Zeeman fields according to Eq. (12).

A detailed theoretical study of steady-state multiresonance experiments in the liquid phase has been carried out by J. H. Freed and co-workers in a series of papers [153–155] using the density matrix formalism and Redfield's approximate treatment of relaxation. In one of these papers [155], subtle line shape effects—broadening and splitting—were described that are due to the coherent nature of the applied strong rf and mw fields. A specific coherence effect is particularly interesting because it can be exploited to assign ENDOR lines to molecular positions, i.e., when applying ENDOR as an analytical tool. It requires nuclear spins $I > 1/2$ or a set of at least two equivalent nuclei of $I = 1/2$. The magnitude of the coherence splitting is dependent on the hyperfine transitions being mw saturated and on the rf field strength.

This coherence effect was optimized by K. P. Dinse et al. [156, 157] to assign hyperfine splittings in ENDOR-in-solution spectra of various low-symmetry radicals by counting the number of protons contributing to a specific ENDOR line. A cylindrical ENDOR cavity (TE_{011} mode) was constructed to achieve cw rf fields up to 3 mT (rotating frame). The internal NMR coil is part of the power stage of a 1 kW cw rf transmitter station. To secure thermal stability of the cavity frequency, effective water cooling was employed both for the cavity body and the two-loop NMR coil [157].

On the basis of Freed's relaxation theory for radicals in fluid solution, M. Plato, W. Lubitz, and K. Möbius [158] carried out a systematic investigation of the cw ENDOR effect, i.e., the ENDOR sensitivity, of various hetero-nuclei (nuclei other than protons) in organic radicals. Optimum ENDOR conditions, such as temperature and viscosity of the solvent, mw and rf field strengths, were formulated as a function of a few nuclear and molecular properties. They include relaxation rates due to fluctuating spin-rotation interaction, electron–nuclear dipolar and nuclear quadrupolar couplings and Heisenberg spin exchange. The theoretical results were found to be in good agreement with experimental observations on ^{2}H, ^{13}C, $^{14/15}$ N, ^{19}F, ^{31}P and alkali nuclei in different molecular systems, thus allowing predictions to be made on the ENDOR detectability of other chemically interesting nuclei, such as $^{10/11}$B, ^{17}O, ^{27}Al, ^{29}Si, ^{33}S and $^{35/37}$Cl. In the meantime, most of these nuclei have indeed been detected by cw ENDOR in solution [49, 159, 160].

2.2.1.2 cw TRIPLE Resonance as an Extension of Steady-State ENDOR From many applications in chemistry, biology and physics it became clear that steady-state cw ENDOR in solution, though extremely powerful in resolving complex hyperfine

structures of low-symmetry radicals, is suffering from sensitivity problems: Only less than 10% of the EPR intensity is normally observed as steady-state ENDOR effect which has to be maximized by carefully controlling temperature and viscosity of the solvents, thereby optimizing a delicate interplay between electron and nuclear relaxation rates, $W_{\alpha\beta}$ [158]. Additionally, cw ENDOR suffers from problems of assigning the measured hyperfine couplings to molecular positions. This is because the ENDOR line intensities are determined primarily by electron and nuclear relaxation rates and not by the multiplicity of the NMR transitions. These drawbacks were the main motivation to extend liquid-solution ENDOR to electron–nuclear–nuclear TRIPLE resonance [48, 52] in which two high-power rf sources are connected to the NMR coil inside the EPR cavity.

Figure 8 shows the energy level diagram and transition scheme of induced mw and rf as well as relaxation driven EPR and NMR transitions for the simplest case $S = 1/2$, $I = 1/2$. According to the different irradiation schemes involving only one nucleus or two inequivalent nuclei, we distinguish between Special TRIPLE and General TRIPLE resonance.

Special TRIPLE Resonance: There are mainly two drawbacks of the cw ENDOR method: (i) In the frequently occurring case of a W_n bottleneck, i.e., when$W_n \ll W_e$, the ENDOR effect becomes very weak if cross relaxation is absent. (ii) The intensity pattern of ENDOR lines generally does not reflect the number of nuclei involved in the various transitions. Both drawbacks can, at least in part, be overcome by applying two NMR rf fields at a frequency separation $\nu^{\pm}$ of the hfc of a particular set of equivalent nuclei. This Special TRIPLE resonance experiment can be understood with the aid of the four-level scheme of Fig. 8. In addition to the first NMR rf field at, for instance, frequency ν^{-} $(1 \leftrightarrow 3)$, a second NMR rf field at frequency ν^{+}

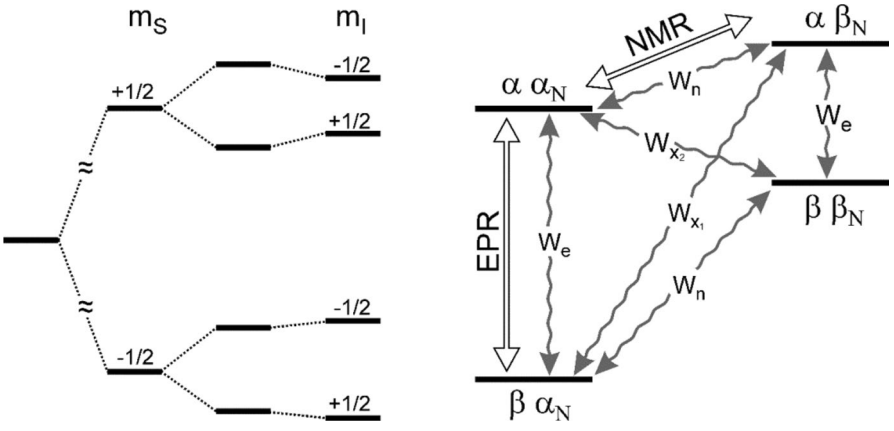

Fig. 8 Four-level diagram of a spin system with $S = 1/2$, $I = 1/2$ (left, a positive sign of the isotropic hyperfine coupling constant is assumed) with indicated (right) induced EPR and NMR transitions together with spin relaxation rates $W_{\alpha\beta}$. Only one EPR- and one NMR-induced transition is shown. The Greek letters $\alpha\alpha_N$, $\alpha\beta_N$,… denote the values of the electron and nuclear magnetic spin quantum numbers m_S and m_I, respectively. The wavy lines indicate the relaxation transitions with their rates for electron (W_e), nuclear (W_n), and electron–nuclear cross relaxation (W_{x1}, W_{x2}). For details, see [1] and references given in the text

short-circuits the W_n bottleneck ($2 \leftrightarrow 4$). Thereby, the efficiency of the NMR-induced relaxation bypass is enhanced. Provided that both rf fields are applied at saturating levels, a considerable increase in the signal intensity can be achieved and, additionally, the line intensities become rather independent ofW_n. For $W_n \ll W_e$, this results in an intensity pattern which, similar to NMR, is dominated by the number of nuclei involved in a particular transition. This facilitates the assignment of hfc's to specific molecular positions. Furthermore, Special TRIPLE has the advantage of narrower lines, i.e., at a given power level the effective NMR saturation, which determines the observed linewidth, is smaller in TRIPLE than in ENDOR. Linewidth reductions of typically 30–50% are observed in agreement with model calculations [161].

General TRIPLE Resonance: We have shown that in the special triple resonance version, both rf fields are applied at a separation of the hfc, A_{iso}, (denoted as "a" in Fig. 9) of the same nucleus. Triple resonance can, however, be generalized to several inequivalent nuclei with the aim to obtain hfc's together with their relative signs [52]. If we consider, for example, two inequivalent protons, the first-order energy levels in the basis $|m_e m_{I_1} m_{I_2}\rangle$ can be arranged to form the eight corners of a cube, see Fig. 9. In such a three-dimensional representation, the various desaturation bypasses for a pumped electron transition, involving the NMR transitions of the two nuclei, can be visualized more clearly than in the conventional two-dimensional transition schemes. In Fig. 9, this energy level arrangement is depicted for the two different cases, $a_1, a_2 > 0$ and $a_1 > 0$, $a_2 < 0$. Every two corners are connected by the various relaxation and induced transitions, the EPR transitions occurring vertically,

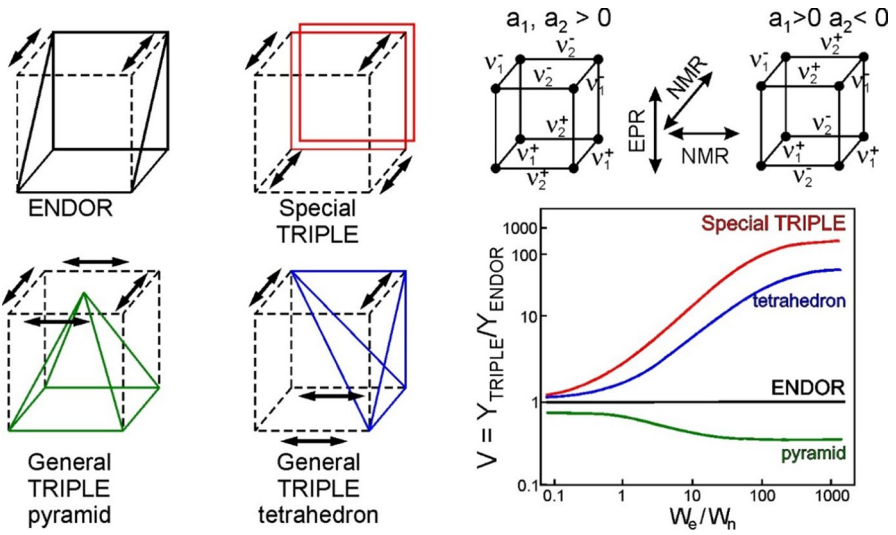

Fig. 9 Topology of ENDOR and TRIPLE resonance experiments for the three-spin system $S = 1/2$, $I_1 = 1/2$, $I_2 = 1/2$. The NMR transitions with their frequencies are given for the two cases of equal and opposite signs of the hyperfine couplings. For simplification, the EPR transitions are not distinguished. The graph shows the TRIPLE amplification factor V as function of the ratio W_e/W_n, obtained by analyzing the electric-circuit analog of the various relaxation networks. The curves shown are valid for induced NMR rates 100 times larger than W_n; cross relaxation was neglected. For details, see ref. [48]

the NMR transitions horizontally. All transitions are doubly degenerate to first order. If we now consider the level populations, the different multiple-resonance experiments can be represented by different geometrical figures (see left part of Fig. 9). These figures are derived from the cubes by contracting those corners that are connected by induced NMR transitions. They represent the limiting case of highly saturated transitions where the populations of the connected levels are equalized. In this representation, an ENDOR experiment forms a prism, and a Special TRIPLE experiment forms a square. If we consider the case that both rf fields drive the low-frequency transitions (ν_1^- and ν_2^-), in General TRIPLE two different cases have to be distinguished depending on the relative signs of the hfc's. If they have the same sign, all the NMR transitions are saturated in the same plane resulting in a pyramid. If the hfcs have opposite signs, the NMR transitions for the two nuclei are saturated in the opposite planes and a tetrahedron is formed. The sign of the hyperfine coupling is an important parameter in molecular spectroscopy. For example, in the case of the isotropic hyperfine constant, A_{iso}, the sign provides additional insight into the electronic structure when finding an answer to the question: how is unpaired electron density produced at the nucleus? Either by a spin-polarization mechanism ($A_{iso} < 0$, for example α-protons) or by conjugation or hyperconjugation mechanisms ($A_{iso} > 0$, for example β-protons).

The significance of these topological games is visualized using Fig. 9. It shows the result of a theoretical analysis of the relaxation networks of the various geometrical figures for a wide range of W_e/W_n values [52]. This analysis was performed within the approximation of the electric-circuit analog of rate equations (mentioned above) applying Kirchhoff's laws for branching networks. When a TRIPLE amplification factor, V, is defined as the ratio of TRIPLE and ENDOR line amplitudes, always $V > 1$ for a "tetrahedron" experiment and $V < 1$ for a "pyramid" experiment. The difference between pyramid and tetrahedron becomes particularly pronounced in cases where W_n is much smaller than W_e. Such cases are typical for many ENDOR-in-solution experiments. In the extreme situation $W_e/W_n >> 1$, Special TRIPLE can even reach 100% EPR sensitivity! Obviously, relative signs of hfc's can easily be determined from intensity changes in General TRIPLE spectra. As a representative example, Fig. 10 shows for the fluorenone$^{\cdot-}$/Na^+ ion pair in fluid solution how the intensity patterns of proton and sodium lines change in a characteristic way when extending ENDOR to General TRIPLE. From such intensity patterns the signs of the various hfcs are revealed relative to the sign of the hfc belonging to the pumped transition [162]. Different relative signs of the hfcs of different types of protons and of the sodium counter ion as a function of temperature are reflected by inversion of the amplitude ratios and, thereby, inform about the planarity of the ion pair [162].

To conclude this section on cw mode ENDOR and TRIPLE resonance on systems in fluid solution, we point out that pulsed ENDOR and TRIPLE on solid-state systems is a completely different story, which to tell would require a separate section. This would go beyond the scope of this article and, hence, we mention this issue only in passing and refer to excellent presentations in the literature instead, see for instance [1, 33, 163].

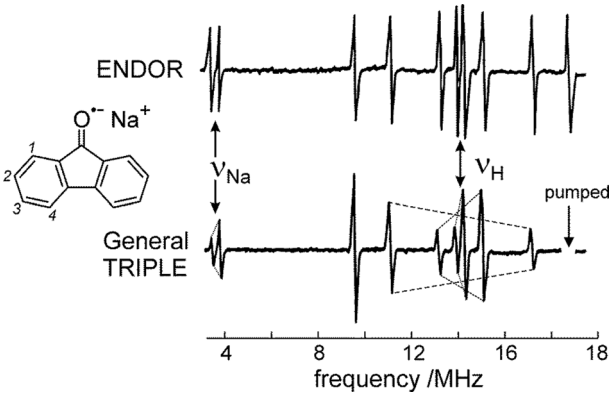

Fig. 10 ENDOR and General TRIPLE spectra of the fluorenone anion radical (solvent: tetrahydrofurane, counter ion: Na^+, $T = 226$ K). For details, see [162]

The basis of the various techniques in pulsed EPR spectroscopy and its multitude of combinations of electron–nuclear and electron–electron resonances, is the detection of the resulting electron spin echoes—in analogy to the spin-echo detection in NMR spectroscopy introduced by E.L. Hahn already in 1950 ("Hahn echoes") (Fig. 11).

Translated to pulsed EPR, in a Hahn electron spin echo (ESE) experiment, a microwave 90° (π/2) pulse at resonance frequency ν produces a signal that decays away (FID). If the EPR spectrum is inhomogeneously broadened, we can recover this disappeared signal with another microwave pulse at the same frequency ν, but of pulse length of 180° (π): after an inter-pulse time delay of τ a Hahn echo is produced, see [33]. Echoes are important in EPR because FIDs of very broad spectra decay away very quickly and often escape detection.

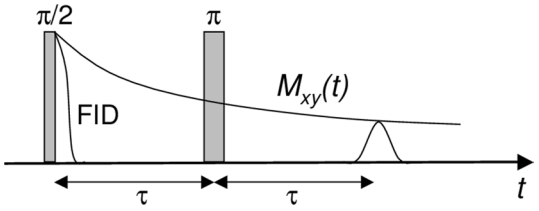

Fig. 11 Hahn Spin Echo in NMR (or EPR). The NMR signal observed following an initial mw excitation π/2 pulse decays in the *xy* plane in the rotating frame (FID, Free Induction Decay) with time due to both spin relaxation and any inhomogeneous effects which cause the spins in the sample to precess at different speeds. The first of these effects, relaxation, leads to an irreversible loss of magnetization. But the inhomogeneous dephasing can be removed by applying a π inversion pulse that inverts the magnetization vectors. Examples of inhomogeneous effects include a magnetic field gradient and a distribution of chemical shifts. If the inversion pulse is applied after a period τ of dephasing, the inhomogeneous evolution will rephase to form an echo at time 2τ

For technical reasons, presently signals cannot be detected during an approximately80 ns period after the microwave pulse. This period of time is called the deadtime of the spectrometer. If the FID is very short, it will disappear before the deadtime ends. If we make τ long enough, we can ensure that the echo appears after the deadtime. There are different pulse schemes for different types of echoes, e.g., the "dead-time free echo detection" and the "stimulated-echo detection" (for references, see [33]). Both of them have become common practice in modern NMR/EPR spectroscopy and magnetic resonance imaging (MRI). Whereas a Hahn spin echo arises from the action of two radiofrequency/microwave pulses, a stimulated echo occurs from the action of three or more radiofrequency/microwave pulses.

How does the echo bring back our magnetic resonance signal? The decay of the FID is due to the different spin packet resonance frequencies in the EPR spectrum causing the magnetization to fan out in the *x*–*y* plane of the rotating frame. When we apply the π pulse, we flip the magnetization about the *x* axis. The magnetization still rotates in the same direction and speed. The higher frequency spin packets will have traveled further than the lower frequency spin packets after the first pulse. However, because the higher frequency spin packets are rotating more quickly, they will eventually catch up with the lower frequency spin packets along the $+y$ axis after the second pulse [33]). After the spin packets had bunched up, they will dephase again just like an FID. If we Fourier transform the FID, we obtain the EPR spectrum. The Fourier transform is a mathematical function that decomposes a waveform, which is a function of time, into the frequencies that make up the waveform. Hence, the Fourier transform is the primary tool for analyzing signals in the frequency domain, especially when signals are sampled. According to Fourier theory, "broad" in the time domain means "narrow" in the frequency domain.

2.2.1.3 Pulse ENDOR In addition to what has been said concerning relaxation effects on the cw ENDOR signal strength, it should be noted that also pulse ENDOR techniques are sensitive to nuclear spin relaxation to some degree, but as a general rule, cw techniques to a greater, pulse techniques to a lesser extent. The cw ENDOR enhancement effect requires a delicate balance of saturation and desaturation of electron and nuclear sublevel transitions at a particular working temperature. For specific sample conditions this is sometimes difficult to do owing to unfavorable electron and nuclear relaxation times T_1 and T_2. In such a situation, pulsed ENDOR techniques are often the solution of the problem. But also pulsed ENDOR might be impeded by too short T_2 relaxation times, while the T_1 times can generally be adjusted by lowering the temperature. Pulsed ENDOR techniques require the nuclear $T_1 \cdot T_2$ product to be sufficiently long to coherently rotate the nuclear magnetization by the rf pulses used for detection. Hence, the sample properties dictate whether cw or pulse ENDOR is the preferable method. To quote from the Schweiger-Jeschke "Scripture": "In most practical situations, cw ENDOR is the method of choice for the measurement of small hyperfine couplings in liquid solution, whereas in solids pulse ENDOR is often superior" [33].

For solid-state samples, ESE-detected pulse ENDOR versions were introduced by W. B. Mims (1965) at Bell Labs [41] and E. R. Davies (1974) at Clarendon [42], see below. Pulsed ENDOR spectroscopy offers several distinct advantages over the

conventional cw technique: The ENDOR effect can be as large as the electron spin echo intensity itself (cw ENDOR reaches only 1–10% of EPR); it requires no critical balance of rf-driven and relaxation transition rates (a condition which has to be met in cw ENDOR); it is less susceptible to artifacts as there is neither an rf nor a mw field applied during the detection period (high-power cw ENDOR often suffers from rf pick-up problems distorting or even ruining the detected signals); it gives immediate access to all relaxation times of a spin system (electron T_1 and T_2, nuclear T_1 and T_2, cross relaxation T_x). Therefore, pulse ENDOR has been the commonly used technique in many laboratories in the last decades, applying pulse sequences predominantly developed by Mims [41] and Davies [42]. The two techniques are very similar to each other in their implementation; however, they are sort of complementary in their results and usefulness, specifically concerning handling of experimental artifacts such as "blind spots" in the spectrum [164].

The Mims-type ENDOR technique is based on a stimulated electron spin echo (ESE) sequence, using two π/2 preparation mw pulses to invert the electron spin population, and a final π/2 mw pulse after the mixing period for stimulated echo signal detection. Between the preparation pulses and the final pulse, an rf π pulse is used to invert the nuclear spin population, resulting in polarization transfer between the nuclear and electronic transitions in the mixing period. The echo intensity is subsequently measured as a function of the rf frequency to give the characteristic ENDOR spectrum. The Mims ENDOR technique is most suited for weakly coupled nuclei, i.e., nuclei with small hyperfine coupling constants.

In Davies-type ENDOR, a preparation mw π pulse is used in order to invert the magnetization of the electron spins in the applied static B_0 field. This essentially creates a hole in the EPR spectrum, whose width and depth depend on the length of the pulse applied, with a long pulse producing narrow holes. During the mixing period, an rf π pulse is applied, and only if the rf frequency is resonant with an NMR transition, magnetization will be transferred to the other m_S electron spin manifold. Otherwise, no mixing will occur to fill in the hole that the inversion pulse creates. During the detection period, the z-component of the magnetization is measured using a mw two-pulse echo sequence, π/2, π, and one detects an inverted echo, i.e., the EPR signal is restored during the mixing period. The Davies ENDOR technique is well suited to detect nuclei with large hyperfine couplings.

All pulse ENDOR techniques suffer from detectability problems at certain frequencies ("blind spots"). The important difference between the Mims and Davies pulse sequences, however, is that in Davies ENDOR there are no blind spots. Blind spots are directly correlated to the size of the hyperfine interactions of the coupled nuclei. Hence, when using pulsed ENDOR as a tool for structure determination, one has to make sure that no artifacts have occurred owing to the specific pulse strategy applied which might mask certain hyperfine couplings and lead to wrong interpretation of the spectra [164]. Powerful pulse strategies have been developed in various EPR laboratories to either avoid or overcome blind-spot artifacts, for references, see [33, 165]. Here we only want to mention, as a promising pulse strategy for high-field pulse EPR spectroscopy, the FID detection of EPR and ENDOR spectra [166] owing to the short deadtime that can be achieved at high microwave frequencies. This FID detection is particularly attractive for EPR and ENDOR of paramagnetic species that

exhibit inhomogeneous EPR line broadening and short dephasing times [33], for example metallo-proteins [33, 167].

2.2.1.4 HYSCORE A very powerful technique for measuring electron–nuclear hyperfine couplings of complex molecular systems is HYSCORE (Hyperfine sublevel correlation spectroscopy), which is essentially a two-dimensional ESEEM experiment in which correlation is transferred from one electron spin manifold m_S (e.g., $m_S = +1/2$) to nuclear frequencies in the other m_S manifold (e.g., $m_S = -1/2$). It is based upon the COSY (Correlation Spectroscopy) NMR experiment and was introduced by P. Höfer, M. Mehring and co-workers [168] at the University of Stuttgart in 1986. This 2D experiment improves the spectral resolution by spreading overlapping peaks over two dimensions and provides information which is difficult to obtain in a 1D ESEEM experiment. Hence, HYSCORE has become the standard experiment for the measurement of complex hyperfine and quadrupole spectra [33] and produces complimentary and comparable information to the ENDOR experiment. In a HYSCORE experiment, the time between the second π/2 and π pulse is varied in one dimension and the time between the π and third π/2 pulse is varied in a second dimension. A two-dimensional Fourier transformation then gives the spectra, and examples from protein chemistry are given, for instance, in [13].

2.2.1.5 ESEEM Hyperfine Spectroscopy A very important class of echo experiments is ESEEM (Electron Spin Echo Envelope Modulation, (ESEEM) [56]). The electron spins interact with the nuclei in their vicinity and this interaction causes a periodic oscillation in the echo height superimposed on the normal echo decay. The modulation or oscillation is caused by periodic dephasing by the nuclei. If we subtract the decay of the spin echo and Fourier transform the oscillations, we obtain the splittings due to the nuclei. Armed with this information, we can identify nearby nuclei and their distances from the electron spin and shed light on the local environment of the radical or metal ion.

Thus, when a single-frequency microwave spin-echo pulse train with varying pulse spacing is applied to a molecular system with hyperfine-coupled electron and nuclear spins, amplitude modulations of the exponentially decaying echo signal can be observed. This ESEEM phenomenon requires certain conditions to be fulfilled by the spin system, as will be shown below. The modulated echo-decay time trace is normally analyzed by means of fast Fourier transformation into the frequency domain to extract hyperfine and quadrupole couplings in a way that is complementary to ENDOR.

In the following, we summarize a recent high-field EPR and ESEEM investigation of the ^{14}N quadrupole interaction of nitroxide spin labels in disordered solids [121]. The aim was to explore the experimental and theoretical background for using the quadrupole-tensor components of nitroxide spin labels for probing polarity and proticity effects of their micro-environment. It is an attempt to obtain an additional handle for separating polarity from proticity effects, which is expected to complement the matrix information obtained from using the g- and nitrogen hyperfine-tensor components of the nitroxide spin probe. We consider the high-field ESEEM

experiments on nitroxide spin labels in organic frozen solutions as a step toward differentiation between polarity and proticity matrix effects on the biological function of proteins.

For protein systems that have exclusively diamagnetic states of their reactants, e.g., the intermediate states of the light-controlled proton pump bacteriorhodopsin, EPR techniques can still serve for probing environmental effects on the process efficiency. This is possible by resorting to site-directed spin-labeling (SDSL) mutagenesis techniques, using specific nitroxide spin-label side chains as reporter groups, for example the MTS [(1-oxyl-2,2,5,5-tetramethylpyrroline-3-methyl) methanethiosulfonate] spin label [169, 170]. SDSL has matured to an extremely important branch of bio-EPR spectroscopy, and tailor-made nitroxide side chains can be introduced at almost any desired site in a protein. It has been shown (for reviews, see [171, 172] that the isotropic and anisotropic components of the g- and hyperfine-tensors of the nitroxide spin label can be used to reveal the polarity and proticity properties of the immediate environment of the reporter group. Since single crystals of membrane proteins are often difficult to prepare, if at all, frozen-solution protein preparations, lacking long-range order, are commonly used for EPR studies of matrix effects.

For nitroxide spin-labeled molecules with rather small anisotropies of their spin interactions, the application of high-field EPR techniques with correspondingly high microwave frequencies is preferable compared to the standard X-band EPR techniques to ensure high spectral and time resolution as well as high orientational selectivity [115, 173]. Such a magnetoselection can be further exploited using double resonance techniques at high fields, e.g., ENDOR or pulsed ELDOR (PELDOR) or ESEEM techniques. They are capable of providing single-crystal like information from orientationally selected fractions of molecules in the disordered samples. By combination of high-field EPR and SDSL techniques, subtle changes of the polarity and proticity profiles could be measured, for example along proton transfer pathways in proteins embedded in natural and artificial membranes [173]. This information was obtained by resolving the g_{xx} and A_{zz} components of the nitroxide interaction tensors of a series of molecules with the spin label attached to specific molecular sites. The linear correlation plots of g_{xx} *vs* A_{zz} are theoretically predicted [174–178] and experimentally established [179, 180]. Moreover, different slopes occasionally observed in the g_{xx} *vs* A_{zz} plots were assigned to either polarity or proticity effects on the magnetic parameters of the spin label from its local protein or membrane environment.

In contrast to the g- and nitrogen hyperfine-tensors, the ^{14}N ($I = 1$) quadrupole interaction tensor of the nitroxide spin label has not been widely exploited in EPR for probing effects of the micro-environment of functional protein sites. Precise knowledge of the ^{14}N quadrupole coupling constant $e^2 \cdot q \cdot Q$ and the asymmetry parameter η of the electric field gradient at the ^{14}N nucleus in the nitroxide would enlarge the arsenal of sensitive probes for environmental effects on specific sites of the molecule, both in terms of polarity [181] and hydrogen-bond effects [182].

To measure directly the nuclear quadrupole interaction by advanced EPR techniques, the nuclear transitions are normally driven directly by rf fields as in ENDOR. A more indirect though effective alternative is offered by ESEEM, i.e., by applying a mw single-frequency pulse train with varying pulse separation and

observing spin-echo modulations from hyperfine and quadrupole interactions. To obtain detectable modulations of the echo decays it is mandatory that ''forbidden'' transitions, flipping the electron and nuclear spins simultaneously, become partially allowed [56]. This requires an efficient mixing of the nuclear and electron spin eigenfunctions by the dipolar hyperfine interaction. Consequently, the strength of the external magnetic field has to be properly chosen to approximately balance the Zeeman splitting of the nuclear sublevels and the respective hyperfine splitting ("cancelation condition") [183]. This means that an optimum Zeeman field value exists for each nucleus and hyperfine coupling, as has been demonstrated by multifrequency ESEEM experiments on $S = 1/2$, $I = 1/2$ as well as on $S = 1/2$, $I = 1$ systems [183–186]. Pulsed ENDOR and ESEEM techniques are complementary to each other [33, 187] concerning their ability to reveal large or small nitrogen dipolar hyperfine interactions ("geminate" or "distal" nitrogens), respectively. Only a few high-field nitrogen ESEEM experiments on single-crystalline [188] and disordered samples [186] have been reported in recent years. Below, we will review an example from our laboratory [121].

The aim of this work [121] was to investigate, by means of high-field EPR and ESEEM experiments in conjunction with DFT calculations, two important issues: (i) whether nitrogen quadrupole-tensor components can be determined with high accuracy from frozen-solution samples and (ii) what kind of information on the polarity and proticity properties of the nitroxide spin-label environment can be extracted from the interaction between the electric field gradient (tensor with elements $e{\cdot}q_{ij}$) at the site of the ^{14}N nitrogen nucleus and its electric quadrupole moment ($e \cdot Q$). Specifically, the question was addressed whether the ^{14}N quadrupole information on matrix effects is similar or complementary to that obtained from the established spin-probe parameters, g_{xx} and A_{zz}.

We focused on the spectroscopic and quantum-chemical aspects of measuring and calculating the quadrupole interaction parameters of the perdeuterated nitroxide radical R1 dissolved in frozen solutions of either non-polar, aprotic *ortho*-terphenyl or polar, protic glycerol, Fig. 12.

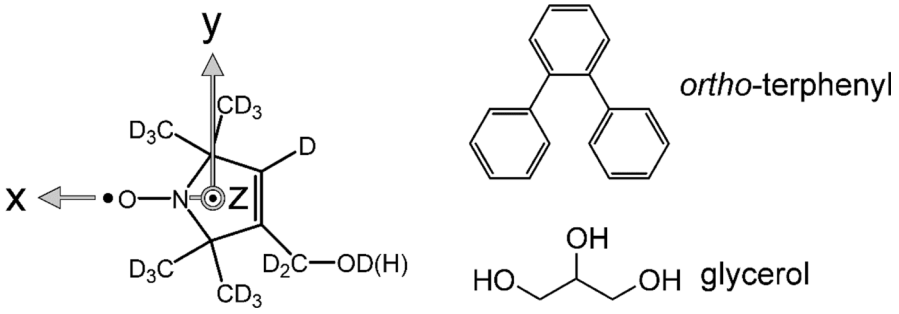

Fig. 12 Molecular structure of the perdeuterated nitroxide radical (R1); the conventional principal axes of the g-tensor are indicated; *ortho*-terphenyl and glycerol hosts for the diluted nitroxide glassy solutions, see [121]. R1was studied both as R1-^{14}N and R1-^{15}N nitroxide radicals

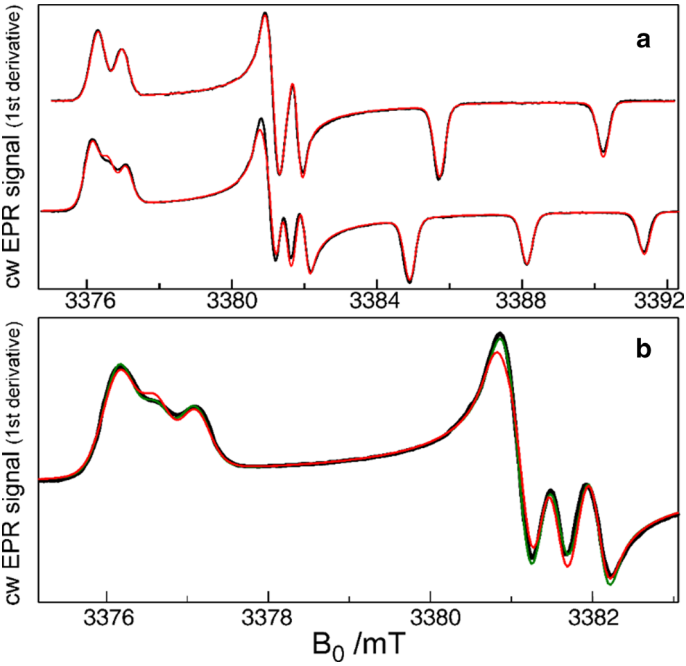

Fig. 13 **a** Experimental W-band cw EPR spectra of 1 mM R1-^{15}N (upper spectrum) and R1-^{14}N (lower spectrum) nitroxide radicals in frozen solution of *ortho*-terphenyl taken at 180 K. They are overlaid with the corresponding best-fit spectra (red lines) obtained without taking the quadrupole interaction into account. For the derived magnetic parameters, see text. **b** Expanded view of the g_{xx}, g_{yy} regions of the R1-^{14}N spectrum. The best-fit spectra calculated without quadrupole contributions and with the quadrupole couplings P_{xx} = 1.1 MHz; P_{yy} = 0.6 MHz are shown by red and dark-green lines, respectively. For details, see [121]

Figure 13 shows W-band cw EPR spectra of R1-^{14}N and R1-^{15}N nitroxide radicals in frozen ortho-terphenyl solution at 180 K. The spectra exhibit the typical powder-pattern lineshape expected for a dilute distribution of nitroxides. The spectra are clearly resolved into three separate regions corresponding to the principal values of the g-tensor, g_{xx}, g_{yy} and g_{zz} Moreover, due to the reduction of the inhomogeneous linewidth by perdeuteration of the radicals, the nitrogen hyperfine splitting (doublets for R1-^{15}N, $I = 1/2$, triplets for R1-^{14}N, $I = 1$) is observed in all g-regions. The spectra were analyzed by numerical solution of the spin Hamiltonian given in Eq. (2). At first, the spectrum of R1-^{15}N was considered. The best-fit spectrum is shown in Fig. 13a. Perfect agreement with the experimental spectrum is achieved by using the set of magnetic parameters, i.e., g-tensor, nitrogen hyperfine-tensor, homogeneous EPR linewidth, orientation-dependent EPR inhomogeneous linewidths, as listened in [121]. In the next step, the spectrum of R1-^{14}N was calculated using the parameters obtained from R1-^{15}N, i.e., tentatively omitting quadrupole

contributions, but rescaling the γ_N and A values by the factor $(1.4)^{-1}$ according to the ratio of the nitrogen nuclear g-values $g_n(^{15}N)/g_n(^{14}N) = 1.4$. Although there is good agreement of the positions of the EPR lines in all spectral regions of the g-tensor components (see Fig. 13a), the EPR signal intensities agree only in the g_{zz} spectral region. This disagreement of intensities in the g_{xx} and g_{yy} regions cannot be improved by varying the corresponding linewidths. However, switching on the ^{14} N quadrupole interaction term in the spin Hamiltonian allows to reproduce the intensities of the experimental EPR spectrum, Fig. 13b. From the simulation, the values $P_{xx} = +1.1$ MHz and $P_{yy} = +0.6$ MHz were obtained. Thus, the quadrupole effects in the cw W-band EPR spectrum of perdeuterated ^{14}N nitroxide radicals are directly observed. This is only possible because of the narrow EPR linewidth (below 10 MHz) of the perdeuterated spin label.

Although the ^{14}N quadrupole interaction is observed in the cw W-band EPR spectra, the P_{xx} and P_{yy} values can be evaluated only with quite a large error. This is because they are obtained by a multiparameter fit of fine details of the experimental cw EPR spectra. Hence, we decided to resort to ESEEM experiments from which

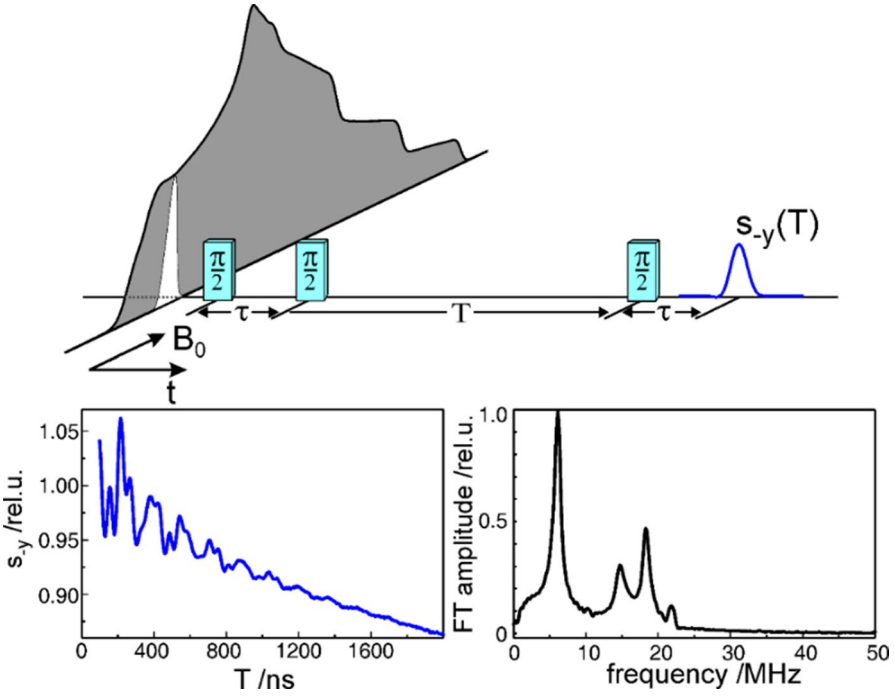

Fig. 14 W-band microwave pulse sequence for the stimulated high-field ESEEM experiment on the nitroxide radical R1. Top: The echo-detected EPR spectrum of the R1-^{14}N radical as well as the microwave excitation bandwidth for typical microwave pulse-length settings are shown (τ = 40 ns, $\pi/2$-pulse length t_p= 30 ns. The time T is stepped from T_0 = 100 ns in 5 ns steps). Bottom left: Representative example of a nuclear modulation echo-decay trace at the indicated B_0 position. Bottom right: Fourier-transformed (FT) spectrum of the ESEEM echo-decay trace. For details, see [121]

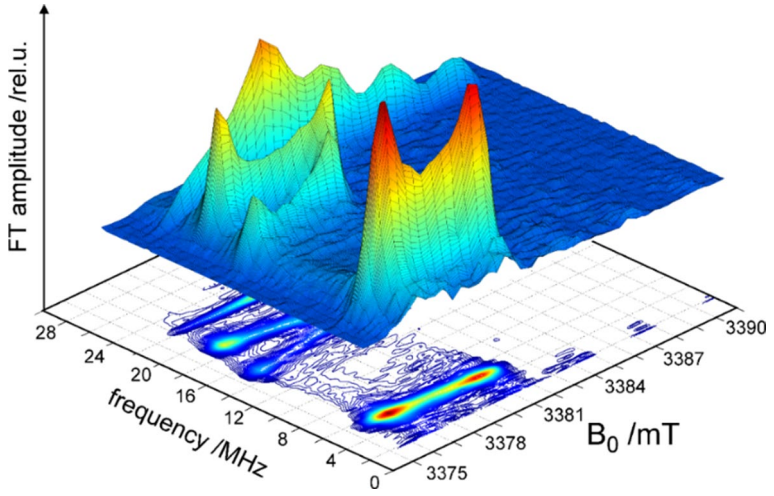

Fig. 15 3D representation of the experimental ESEEM surface. In the frequency-B_0 plane, the contour-plot representation of the ESEEM intensities is shown. This 3D representation is now commonly used in the literature. For details, see [121]

the quadrupole interactions can be determined in a more straightforward way, see Figs. 14, 15).

The stimulated ESE decays show distinct modulations for both the R1-^{15}N and the R1-^{14}N nitroxides. In the case of R1-15N, the echo modulation is dominated by a frequency of about 22.1 MHz in the whole spectral region of nitroxide EPR absorption. This modulation is assigned to the nitroxide methyl deuterons, see Fig. 12. Additional ESEEM frequencies are detected in the g_{xx}, g_{yy} region. Their analysis and interpretation are thoroughly discussed in [121] and [1]. There, it is concluded that measurement of the quadrupole component P_{yy} can provide important contributions to the study of environmental effects. Additionally, it serves as a consistency check of polarity and/or proticity results obtained from the often employed g_{xx} *vs.* A_{zz} correlation in spin-label EPR spectroscopy.

Polarity control in protein complexes from innermolecular electric fields have been widely investigated by observing shifts of A_{zz} and/or g_{xx} on NO spin labels in various environments. Whereas A_{zz} reacts to polarity changes in non-bonding as well as H-bonding situations predominantly through changes in the spin density distribution of the NO bond (as a consequence of charge displacements between N and O), g_{xx} is also significantly affected by additional perturbations of the n–π energy gap of the O-atom in H-bonding situations. Thus, the observation of g_{xx} shifts may be desirable for the detection of H-bond formation (proticity), but can also lead to ambiguous results in trying to quantitatively separate proticity from polarity effects. If measurement of A_{zz} alone does not safely yield the desired information on polarity changes, measurement of P_{yy} is, therefore, the appropriate choice. Qualitatively, P_{yy}

has the same probing properties as A_{zz} in detecting polarity and proticity effects, see [121].

2.2.1.6 ELDOR-Detected NMR (EDNMR) As we have seen, there are several pulsed EPR techniques that are capable of probing nuclear transition frequencies of paramagnetic compounds such as ESEEM-based techniques, as well as ENDOR techniques. There is another technique able to unravel congested nuclear spectra which has become very popular in recent years, and this is Pulsed ELDOR-detected NMR (EDNMR) [141], see Fig. 5. The acronym ELDOR stands for electron–electron double resonance, i.e., two microwave fields are involved. The EDNMR experiment was introduced by A. Schweiger and his co-workers at the ETH Zurich in 1994, it excels by its potential to determine small hyperfine interactions in disordered systems. In the original version of EDNMR, a strong and long selective preparation pulse (HTA) of microwave frequency ν_b excites allowed and forbidden transitions simultaneously, thereby burning spectral holes into the EPR line. The positions of the holes caused by the excitation of forbidden transitions correspond to the nuclear transition frequencies of the spin system. A selective detection pulse of frequency ν_a creates an FID with integrated intensity proportional to the magnetization at this frequency. The entire hole pattern is obtained by recording the integrated intensity of the FID while varying the frequency difference $\Delta\nu = \nu_b - \nu_a$ step by step. More recent EDNMR experiments apply a Hahn-type primary echo pulse sequence for detection instead of using FID detection [288, 289].

A few words concerning the fundamental difference between coherence-transfer techniques and polarization-transfer techniques seem to be appropriate at this point: ESEEM is a coherence-transfer technique in which the nuclear frequencies are obtained from the analysis of the time-dependent electron spin-echo modulation caused by the oscillation between allowed and forbidden electron coherences or by the evolution of nuclear coherences. ENDOR and EDNMR are polarization-transfer pulsed EPR experiments, that is, the nuclear frequencies are detected by manipulating the polarizations of electron and nuclear levels. The principal difference between ENDOR and EDNMR is the way in which the population of the nuclear levels is changed. In pulse ENDOR, the nuclear polarization is inverted by driving the allowed NMR transition ($\Delta m_S = 0$; $\Delta m_I = \pm 1$) with an rf π-pulse. In contrast, in EDNMR, the nuclear transitions of the spin manifold are probed indirectly by using a second strong and long microwave pulse (also called high-turning-angle (HTA) pulse), which drives forbidden electron transitions, ($\Delta m_S = 0$; $\Delta m_I = \pm 1$) that is, transitions where both the electron and nuclear spin change their projection direction. Such "forbidden" transitions in the spin manifold are "only weakly allowed" in the presence of an anisotropic hyperfine interaction or a nuclear quadrupole interaction. The frequency ν_2 of the pumping HTA pulse is swept around the fixed resonance frequency, ν_1 of the detection Hahn echo pulse sequence. At mw frequencies, where the HTA pulse coincides with a forbidden transition the observed primary echo signal of an allowed EPR transition decreases due to population transfer via the forbidden transitions. These ν_{mw} dependent changes in population differences and concomitant signal changes are observed as spectral lines, which correspond to the nuclear transitions of the spin manifold. For the simple case of a 4-level scheme

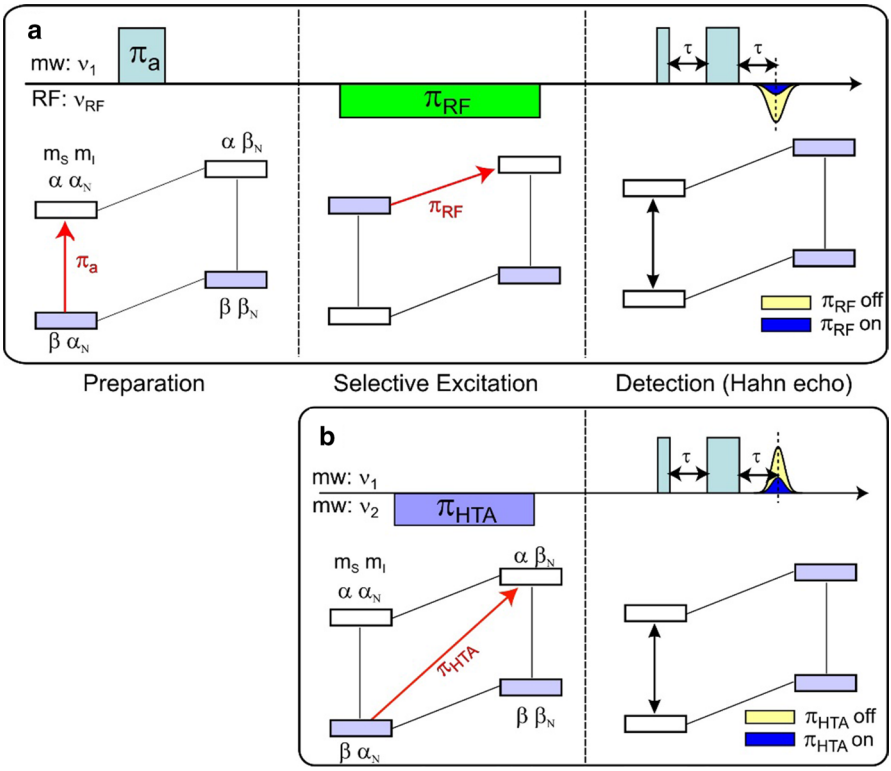

Fig. 16 Comparison of pulsed Davies-type ENDOR **a** with pulsed ELDOR-detected NMR, EDNMR **b** phenomenological description of spin populations after the respective pulses have flipped the spin projections of the electron and nucleus for the case $S = 1/2$, $I = 1/2$. Polarization transfer in the Davies-type pulse ENDOR experiment involving allowed electron and nuclear spin transitions. Polarization transfer in the EDNMR experiment involving allowed and forbidden transitions of the hyperfine-coupled electron and nuclear spins. For details, see ref. [13]. The labels π_a, π_{RF} and π_{HTA} denote the π-pulses required for optimal polarization transfer. Note: In the figure, the radiofrequency pulses are denoted "RF", while in the text they are denoted "rf"

($S = 1/2$, $I = 1/2$ with hyperfine interaction), Fig. 16 depicts the different forms of pulse-driven polarization transfer in Davies ENDOR (Fig. 16a) and EDNMR (Fig. 16b).

Pulsed ENDOR uses a selective mw pulse train at a frequency, which is in resonance with an allowed electron spin transition, to flip the electron spins and to observe the change of electron polarization which had occurred as a result of the change in nuclear polarization by flipping the nuclear spins by the rf pulse with the frequency of an allowed nuclear spin transition. In pulsed ELDOR-detected NMR, following the HTA pulse at a chosen mw frequency ν_2, a selective pulse train with fixed mw frequency ν_1 is applied probing an allowed electron spin transition. The frequency ν_b of the HTA pulse is varied, and once it matches one of the forbidden "cross" transitions ($\Delta m_S = \pm 1$; $\Delta m_I = \pm 1$), a population transfer occurs which is manifested in a change of the Hahn echo intensity (this population transfer can

alternatively be observed as a change of FID intensity [189]). The EDNMR experiment can principally be performed at any microwave frequency bands where the "forbidden" cross transitions are observable by EPR. It turned out, however, that it works best at Zeeman fields high enough to separate the NMR lines around the nuclear Larmor frequency well from the hole burnt into the EPR spectrum of allowed transitions by the HTA pulse, but small enough to keep the ratio of hyperfine and Zeeman interactions large enough to retain substantial second-order terms in the electron transition probabilities. Apparently, such conditions working in opposite direction can often be fulfilled by high-field EDNMR at W-band [190–194], and this method has become very attractive for measuring nuclear frequencies for low γ nuclei exhibiting broad ENDOR lines.

Compared to ENDOR, high-field EDNMR presents several advantages for the investigation of low-γ nuclei coupled to the electron spin of metallo-proteins. EDNMR is more robust against fast electron spin–lattice relaxation, T_1, and spectral diffusion than ENDOR. This robustness is because no preparation of the electron spin system prior to the HTA pulse is required and short HTA pulses can often be realized with the available microwave power. This results in high sensitivity and allows one to rapidly record 2D-EDNMR spectra with a sufficient signal-to-noise ratio. Moreover, the recorded EDNMR spectrum is not distorted by blind spots around the nuclear Larmor frequencies. These advantages have been demonstrated using a simple model system, $Mn^{II}(H_2{}^{17}O)_6$, see [195]. The spin Hamiltonian parameters extracted are: $A_{iso} = -7.7$ MHz; $A_{dip} = [-1.5; -1.5; 3.0]$ MHz; $\frac{e^2qQ}{h} = -8.5$ MHz; $\eta = 1$. For details, see [195] and [13].

Baute and Goldfarb [196] had shown that the ^{17}O signals arising from the hyperfine splitting of the ^{17}O nucleus within the $m_S = \pm 1/2$ and $\pm 3/2$ sublevels of the Mn^{II} electron spin manifold can be readily detected at W-band using Davies ENDOR for the corresponding EDNMR of the $Mn^{II}(H_2{}^{17}O)_6$ complex. For details, see [13].

Recently, the Goldfarb group (Rehovot) has extended EDNMR to a correlation method, referring to it with the acronym THYCOS (triple resonance hyperfine sublevel correlation spectroscopy) [191, 194]. It combines ENDOR and EDNMR in a manner similar to the pulsed TRIPLE method [151, 197, 198]. In the THYCOS pulse sequence, the HTA mw pulse with frequency ν_1 transfers population across a forbidden EPR transition ($m_S = \pm 1$; $\Delta m_I = \pm 1$). This reduces the population difference between the corresponding allowed transition which is detected via an FID (or a spin echo) produced by a selective pulse (or an echo pulse sequence) with frequency ν_2. A change in the FID intensity occurs when a rf pulse transfers population from any level affected by either of the mw pulses. The FID (or spin-echo) intensity decreases if the rf pulse excites the same nucleus as the HTA pulse, and it recovers if another nucleus is involved. Therefore, the THYCOS experiment correlates lines in the EDNMR spectrum with lines in the ENDOR spectrum of nuclei belonging to different electron spin manifolds m_S. This facilitates the assignment of nuclear resonance frequencies to their respective m_S manifold, and, hence, gives the sign of the hyperfine coupling. The feasibility of this new technique has been demonstrated for Cu^{2+}-histidine complexes both in single-crystal and frozen-solution samples [191].

The following is an interesting example of high-field EDNMR and ENDOR in photosynthesis research [16]:

Example: Local water sensing: Water exchange in bacterial photosynthetic reaction centers

By means of pulsed W-band (94 GHz) high-field multiresonance EPR spectroscopies, such as ELDOR-detected NMR and ENDOR, in conjunction with using specifically isotope-labeled water (D_2O and $H_2{}^{17}O$), the biologically important issue of detection and quantification of local water in membrane proteins is addressed. A specifically engeneering mutant of the bacterial reaction center (bRC) from *Rhodobacter sphaeroides* R26 embedded into a trehalose glass matrix is used as the model system. This bRC mutant hosts the two native radical cofactor ions $P_{865}^{\cdot+}$) (primary electron donor) and $Q_A^{\cdot-}$ (primary electron acceptor) as well as a nitroxide spin label site-specifically attached to a cysteine amino-acid site on the surface of the H-protein domain of the bRC. The resulting three paramagnetic reporter groups have distinctly different local environments. They serve as local probes to detect water molecules via hyperfine interactions (electron–nuclear hyperfine and quadrupole) with either ^2H or ^{17}O nuclei. The bRCs in the EPR sample tube were equilibrated in an atmosphere of different relative humidities allowing to control precisely different hydration levels of the protein. As the main result, we showed that using oxygen-17-labeled water, quantitative conclusions about the local and bulk water environment of the protein can be made. This approach is superior to the conventional strategy of using D_2O water for aqueous matrix studies, which suffers from proton–deuterium exchange processes in the protein. From the experiments we also concluded that dry trehalose operates as an anhydrobiotic protein stabilizer, a conclusion that is in line with the "anchorage hypothesis" of anhydrobiotic bio-protection. It predicts selective changes in the first solvation shell of the protein upon trehalose-matrix dehydration with subsequent changes in the hydrogen-bonding network. Changes in hydrogen-bonding patterns usually have an impact on the overall function of a biological system.

After this brief summary of our 2017 study, we will present some informative details that seem advisable for a better understanding of the work [16].

Water plays an important, if not essential part in the chemistry of Life on Earth. In particular, it governs the internal dynamics of biological macromolecules, such as proteins. Unrestricted dynamics at a specific time scale is a crucial requirement for the specific biological activity of proteins, including enzyme activity, macromolecular recognition, ligand binding and participation in electron and proton transfer processes. Under physiological conditions these macromolecules fluctuate between different conformational states [199]. Their dynamics span an enormous time range, i.e., from sub-picosecond to tens of microseconds, and include a multitude of stochastic local and collective motions, from bond vibrations to domain motions. Despite significant efforts over the past decades, our microscopic understanding of protein dynamics remains rather limited [200–202].

Liquid water has some unusual physical and chemical properties that are important for controlling its potency as a solvent, its ability to form hydrogen bonds and its amphoteric nature, i.e., the ability to act either as an acid or a base. Nevertheless, until rather recently, molecular biologists have regarded water essentially as the backdrop on which the molecular components constituting "Life" are arrayed and functionalized [203]. It is clear by now that water is an active constituent of

cell biology which has to be included in a meaningful molecular picture of life processes, see for example [204].

Water drives protein folding through hydrophobic interactions (the "hydrophobic effect") [205–208] but also contributes to the stabilization of the 3D protein structure and modulates the dynamics of a protein in a variety of ways [209]. In biological systems water is usually divided into three distinctly different classes: (i) internal, strongly bound water that cannot be removed even upon lyophilization; it contributes to the stabilization of the native protein structure. Internal water molecules that are hydrogen-bonded to specific amino-acid residues in a water pocket or are mobile along inner protein channels are often of key importance for protein function [210–212]; (ii) surface water in the hydration shell of the protein at the solute–solvent interface, and (iii) bulk water randomly distributed in the protein matrix. Water molecules in the protein hydration layer have restricted dynamics with respect to water molecules in the bulk. The thickness of the hydration layer at the solute–solvent interface is still a matter of debate, and the different results reported can often be rationalized by considering that different experimental methods probe different dynamical ranges of molecular motion. Such methods include nuclear magnetic resonance (NMR) [209, 213–215], Dielectric Spectroscopy in the microwave region [216], Terahertz Absorption Spectroscopy [204, 217], Infrared Spectroscopy (IR) [218, 219], and Neutron Spectroscopy [199]. Parallel to the development of new experimental methods for unraveling solvation dynamics of large molecules, powerful extensions of molecular dynamics simulation techniques have been recently reported [204, 220–222]. Solvated proteins exhibit complex conformational dynamics at physiologically relevant temperatures fluctuating between a multitude of conformational substates in a rugged energy landscape that is hierarchically organized in energy tiers [206, 223]. For most proteins cooled below the glass-transition temperature (typically around 200 K) their biological function is blocked due to restricted conformational motion. The "freezing out" of conformational dynamics by lowering the temperature is, thus, a common strategy for studying function–dynamics relationships in proteins.

However, freezing proteins in the presence of a cryoprotectant (used to minimize freezing damage by ice crystals) is problematic because it aggravates disentanglement of the influences of solvent and temperature on the protein dynamics. An elegant alternative approach is to embed the protein into amorphous matrices formed by disaccharides like trehalose (α-D-glucopyranosil α-D-glucopyranoside) [224, 225]. This allows preservation of the native protein fold during extensive protein dehydration, even at temperatures well above room temperature. In nature, the extraordinary bio-protective capabilities of disaccharide glasses are exploited by specific organisms, which are able to survive extreme conditions of temperature and dehydration by entering a state of reversibly arrested metabolic activity, called *anhydrobiosis* or *cryptobiosis* [226]. Extensive spectroscopic work, exploiting neutron scattering [227, 228], Raman [229], optical laser-flash [230], FTIR [231], and EPR [8] on different proteins incorporated into trehalose glasses have revealed a tight protein–matrix dynamic coupling at low water content. This implies that the protein conformational dynamics is controlled by that of the water–trehalose matrix coating the protein surface [8, 227–232]. At room temperature, the stepwise dehydration of

the trehalose matrix results in increasingly inhibited dynamics of the embedded protein. This was observed in both small globular proteins like myoglobin [224, 227] and large membrane proteins like bacterial photosynthetic reaction centers [225, 233] and photosystem I [234] of oxygenic photosynthesis.

Trehalose is the most efficient sugar for bio-protection against extreme dehydration and osmotic stress. The exact mechanistic details of the trehalose efficiency are not clear yet, but likely involve an interplay between several factors that include its extraordinarily high glass-transition temperature (385 K) [235], its polymorphism adopting several crystalline and amorphous states [236], its distinct propensity for hydrogen-bonding and the pronounced rigidity of its dehydrated glass matrix [237]. There exist several mechanistic hypotheses for explaining the exceptional behavior of trehalose (for a recent review, see ref. [238]). Generally speaking, these hypotheses, which are not mutually exclusive, vary in the fate of water molecules close to the protein surface and on how much the first solvation shell is depleted in favor of H-bond forming trehalose molecules. A dehydration of the protein certainly shifts the hydration equilibrium, but it is not known to what extent.

In this work, we applied pulsed multiresonance EPR techniques at high microwave frequency (W-band, 94 GHz) and a correspondingly high magnetic Zeeman field (3.4 T) to detect and quantify the accessibility of local water in bacterial photosynthetic reaction centers (bRC) from *Rhodobacter (Rb.) sphaeroides* R26 that were embedded in trehalose glasses at distinct hydration levels. The bRC is an integral membrane protein that catalyzes the initial photochemical processes to convert light energy into chemical free energy [239–241]. In the R26 mutant, the paramagnetic Fe^{2+} cofactor is replaced by diamagnetic Zn^{2+} to avoid excessive line broadening due to the paramagnetic Fe^{2+} ion [242].

The three bRC protein subunits, L, M, and H, host several cofactors [243] sequentially involved in light-driven electron transfer. Two bacteriochlorophyll *a* (BChl *a*) molecules near the periplasmic side of the membrane form the "special pair" P_{865}. After photo-excitation to its singlet state, the subsequent electron transfer proceeds predominantly via the protein branch A [239] to the Q_A acceptor. In the present EPR study, the secondary electron transfer $Q_A^{\cdot-} \rightarrow Q_B$ was blocked by Q_B deprivation (here, using stigmatellin [244]. The anion radical $Q_A^{\cdot-}$ is of particular concern. The nitroxide spin-label MTSSL was attached to Cys156 in the H-protein subunit. By EPR spectroscopy one can measure the electron Zeeman and electron–nuclear hyperfine interactions and thereby probe the unpaired electron spin density distribution in the transient ionic radical states, $P_{865}^{\cdot+}$ and $Q_A^{\cdot-}$, which are created during light-induced charge separation. These paramagnetic states provide unique information about the electronic structure of the electron-transfer system and, hence, have been thoroughly characterized previously by both cw and pulse EPR, for review see refs. [1, 140]. P_{865} and Q_A are located close to the periplasmic and cytoplasmic sides of the membrane, respectively, and are, thus, well suited to be used to study local water accessibility in the protein near its surface. In the bRC preparation of this work, with no cytochrome present and electron transfer from $Q_A^{\cdot-}$ to Q_B blocked, the charge-separated state $P_{865}^{\cdot+}Q_A^{\cdot-}$ recombines to $P_{865}Q_A$ within 100 ms by direct electron tunneling [239]. Hence, continuous illumination generates a steady-state EPR signal of the $P_{865}^{\cdot+}Q_A^{\cdot-}$ state that rapidly decays once the light is switched off. The W-band EPR

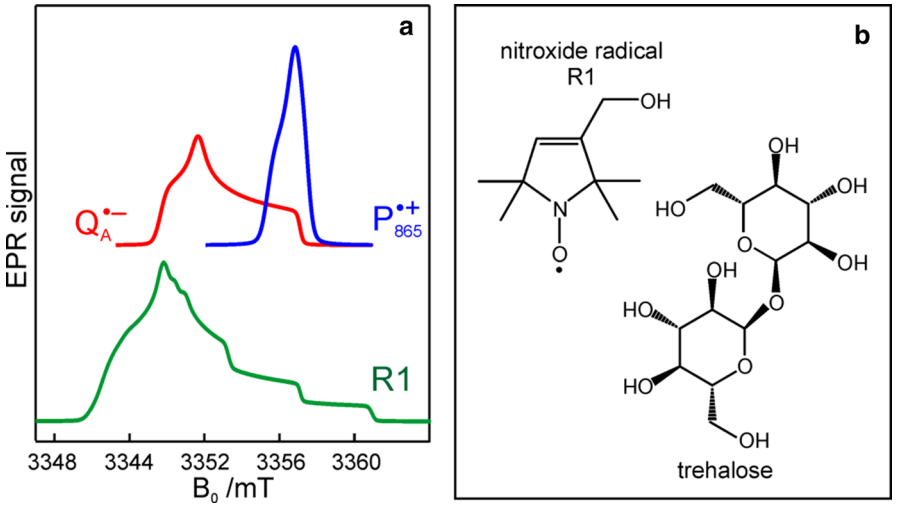

Fig. 17 **a** Top: Simulated rigid limit W-band EPR absorption spectra of $P_{865}^{\cdot+}$ (blue trace) and $Q_A^{\cdot-}$ (red trace), the radical-ion states of the primary donor and acceptor. For the simulation, previously reported magnetic parameter values were used [245, 246]. Bottom: Simulated rigid limit W-band EPR absorption spectrum of the nitroxide radical R1 (green trace). The magnetic parameter values used for the spectrum simulation were previously reported for a nitroxide dissolved in a water/glycerol mixture [247]. **b** Chemical structures of the pyrroline type MTSSL nitroxide radical R1 and the disaccharide trehalose (color figure online)

spectra of both $P_{865}^{\cdot+}$ and $Q_A^{\cdot-}$ reveal rhombic g-tensors [245, 246] resulting in characteristic line shapes, see Fig. 17a.

The native bRC contains five cysteine residues which are buried within the protein domains except for cysteine 156 which is moderately solvent exposed in subunit H. This residue can be site-specifically spin labeled with an external paramagnetic probe molecule. We used MTSSL (1-oxyl-2,2,5,5-tetramethylpyrroline-3-methyl-methanethiosulphonate) as spin label [248, 249]. The nitroxide-labeled bRC protein [250] (SL-bRC) provides a third paramagnetic probe within the bRC in addition to the "natural" radical ions $P_{865}^{\cdot+}$ and $Q_A^{\cdot-}$. According to the known protein 3D structure, the "artificial" nitroxide spin label experiences a water accessibility very different from that of the native cofactors, P_{865} and Q_A. Even under high-field (W-band) conditions, the close similarity of the g-tensor components results in strong overlap of the EPR spectra of $P_{865}^{\cdot+}$, $Q_A^{\cdot-}$ and nitroxide spin label embedded in their protein matrix environment.

A powerful pulse EPR technique that can be employed also at W-band frequencies is EDNMR. [189] Using a second mw source, it overcomes the instrumental limitations of the ESEEM single-resonance technique at W-band. Recently, W-band EDNMR has been demonstrated to provide superior sensitivity as compared to ENDOR [12]. Also the solvation properties of large protein metal complexes [195, 251] could be successfully studied by W-band EDNMR.

The effect of bRC coating in a trehalose glass matrix has been thoroughly studied previously using laser-flash optical and EPR spectroscopies [8, 225, 230, 233, 252].

In bRCs, the coating with trehalose affects the electron-transfer step between the primary and secondary quinone acceptors [233] which is a conformationally gated process [253]. The trehalose matrix also influences the lifetime of the charge-separated radical-pair state, $P^{\cdot+}_{865}Q^{\cdot-}_{A}$. Upon progressive dehydration of the trehalose matrix, the kinetics of $P^{\cdot+}_{865}Q^{\cdot-}_{A}$ charge recombination becomes faster and exhibits widely distributed rate constants [225, 230, 252, 254]. Thus, it mimics at room temperature the bRC recombination kinetics observed at cryogenic temperatures in the water–glycerol system when frozen in the dark [255, 256].

A reasonable explanation for this matrix effect is the stronger dynamical coupling between sugar and protein via hydrogen-bonding networks in a dehydrated trehalose matrix. It blocks the fluctuations between conformational substates of the bRC [230], as put forward in the "anchorage hypothesis" [232].

The progressive dehydration of sugar glasses requires a change of the water equilibria between the first solvation shell and bulk water (and possibly also between strongly bound internal water). Two relative hydration levels, *r,* were chosen in this work that result in a different extent of slaving the protein dynamics to the embedding sugar matrix: (i) $r = 11\%$ for which the protein dynamics is arrested on the time scale of seconds [252], and (ii) $r = 74\%$ for which the dynamics is only mildly retarded as compared to solution [14]. Using EDNMR, we aim to probe directly if the dehydration of the sugar matrix results in a changed hydration level of the inner protein core surrounding the native cofactors, $P^{\cdot+}_{865}$ and $Q^{\cdot-}_{A}$. To trace the exchange of water between the sugar matrix and the interior of the protein, the use of isotope-labeled water is essential, with regard to both deuterium and oxygen-17. By high-field EPR, we can test how the hydration of the sugar matrix translates into water exchange between the sugar matrix and either protein surface or protein interior.

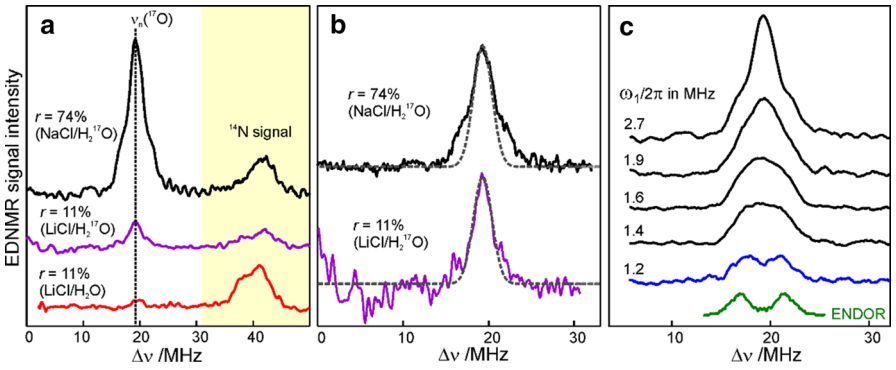

Fig. 18 **a** W-band EDNMR spectra for SL-bRC/trehalose glass samples equilibrated for 70 h at $r = 74\%$ (NaCl/H$_2$^{17}O) black trace; $r = 11\%$ (LiCl/H$_2$^{17}O) magenta trace; and $r = 11\%$ (LiCl/H$_2$O) red trace. The spectra were recorded at the same nitroxide spectral position (g_{zz}, $M_I = 0$). **b** The ^{17}O EDNMR spectra for $r = 74\%$ (NaCl/H$_2$^{17}O) (black trace) and $r = 11\%$ (LiCl/H$_2$^{17}O) (magenta trace) samples. The gray dashed lines show the best-fit simulation of experimental recordings to a Gaussian line. **c** Microwave field amplitude dependence of ^{17}O EDNMR spectra of SL-bRC/trehalose glasses equilibrated for three days at $r = 11\%$ (LiCl/H$_2$^{17}O). The black spectra were recorded using an HTA pulse length of $t_{HTA} = 20$ µs. The blue trace shows the EDNMR spectrum acquired with $t_{HTA} = 7$ µs. The green line at the bottom shows the Davies ENDOR spectrum recorded at the same spectral position (color figure online)

For details of the sample preparation, the controlled dehydration protocols, and the EDNMR/ENDOR experiments, see [16]. Similar to ENDOR, in EDNMR spectra the hyperfine or/and quadrupole coupled proton or deuterium nuclei yield signals centered at the nuclear Zeeman frequency ν_n(H) or ν_n(D), split by the hyperfine or quadrupole coupling constant.

In the following, the main results of this work will be briefly summarized:

Figure 18c shows EDNMR spectra recorded for SL-RC/trehalose at r = 74% ($H_2{}^{17}O$) with variable mw field amplitudes. At the highest mw field amplitude used, the intensity of the ^{17}O EDNMR line is about 0.1, and both distant and coupled ^{17}O nuclei are detected. When decreasing the mw field amplitude, the overall signal intensity decreases, but the matrix ^{17}O line is affected to a larger extent. To suppress the matrix line almost completely, a two times lower mw field amplitude and shorter HTA pulse length were used, see blue trace in Fig. 18c.

Subsequently, W-band Davies ENDOR measurements were performed to confirm the ^{17}O hyperfine coupling constant as extracted from the EDNMR spectrum, see green trace in Fig. 18c. In Davies ENDOR exclusively coupled water is probed since the signal from distant ^{17}O nuclei is suppressed because of the blind spot at $\nu_n(^{17}O)$. [33] The presence of the ^{17}O line in the EDNMR spectrum of the dehydrated protein/trehalose glass ($r = 11\%$) unambiguously shows that, despite extensive dehydration and the high rigidity of the trehalose, the water retained in the sugar and the water on the protein surface can exchange.

We conclude:

In this work, we compared the water accessibility at three protein sites within the reaction center from the purple bacterium *Rb. sphaeroides* R26 that hosts the two native radical cofactor ions $P_{865}^{\cdot+}$ and $Q_A^{\cdot-}$ and the artificial nitroxide spin label. The three paramagnetic reporter groups have distinctly different local environments in the protein and can probe different types of water molecules, internal water, bulk water and surface water. The native cofactors buried within the protein report on strongly bound internal water and on bulk water in pools and/or channels, the nitroxide radical is surface attached and reports on the first and second solvation shell of the protein.

The bRCs were embedded into a trehalose glass and equilibrated in the atmosphere of either low ($r = 11\%$) or high ($r = 74\%$) relative humidity. The resulting sugar matrix has very different properties: At low humidity and corresponding low hydration level the protein-matrix system is rigid with only 0.5 water molecules per sugar molecule; at higher humidity and hydration level the sugar matrix is less rigid and contains more water molecules as potential partners for hydrogen bonding to the protein and to the sugar matrix. Different hydration levels, therefore, affect the protein dynamics differently: At $r = 11\%$, the dynamics is blocked [9, 14, 252], at least on the timescale of $P_{865}^{\cdot+}$-$Q_A^{\cdot-}$ charge recombination, but is not affected at $r = 74\%$. This effect of the dry trehalose matrix, to inhibit internal protein dynamics (leading to bio-protection of proteins against thermal denaturation), was ascribed earlier to a strong "slaving" of the protein dynamics to that of the embedding matrix [206, 223]. The detailed molecular mechanism of bio-protection is still unclear and leaves open questions, for instance: Why does the hydration of different embedding disaccharide sugars has a strongly different effect on the solvation shell of the protein and on the

dynamics of the water molecules inside the protein [14]? For a detailed discussion of this issue, see [16].

As to the scientific significance of such studies, we want to emphasize that hydration water plays a crucial role in protein dynamics and structural relaxation on all time scales. In the literature [206, 223], it is suggested that changes in the amount of hydration water affect not only the protein's energy landscape but also significantly affect structural fluctuations between the "conformational substates" and, thereby, control biological function. Hence, understanding the functional difference between surface-bound water and bulk water is a key issue for controlling the biological function of macromolecules, including proteins, DNA, RNA, and photosynthetic reaction centers, right up to enabling anhydrobiotic food preservation and storage in dehydrated trehalose matrices at room temperature. Water is just far more than merely a solvent.

So, is dehydrated trehalose the elixir of Life? As far as countering extreme stress conditions by evolutionary adapted living organism are concerned, probably yes. Apparently, trehalose works so well because it possesses an optimum mix of physical and chemical parameters that Nature can provide and implement into a single molecular complex. None of them will be able to accomplish the task of anhydrobiotic stabilization on its own. What works is probably a cumulative effect of all the mechanisms put forward already in the various theories in the literature. The relative contribution of each parameter is adjusted according to the specific stress factor that has to be encountered since it endangers cellular survival in evolutionary selection.

What, at first glance, appears to be of mere academic interest in the biophysical and biological sciences reveals, at second glance, a promising future for trehalose applications in food and medical industries: Owing to its unique properties as allowing for anhydrobiotic survival under harsh conditions of dryness and heat trehalose proved to be an active stabilizer of enzymes, proteins, vaccines, pharmaceutical preparations, and even organs for transplantation. And in molecular engineering departments of biological research institutions, scientists are trying to copy the genetic code of "resurrection plants" in deserts to adapt "normal" plants to the looming global warming of the climate catastrophe.

Among the large variety of photosynthetic species are those with the astounding capability to survive extreme conditions of heat (higher than 60 °C) and dryness (more than 99% of their water body removed) as are typical for hot desert climates. An ultimate strategy by Nature for the survival of drought, in which an organism loses virtually all its free intercellular water, is anhydrobiosis in which the organism ceases metabolism for several years but remains capable of revival after rehydration. Hence, plants qualified for anhydrobiosis have been romanticized as resurrection plants. The pressing question is how anhydrobiosis is accomplished by the organisms. A common theme among such organisms is that during photosynthesis activity they accumulate large quantities of non-reducing disaccharides, the most common of which is trehalose. Survival in the dry state is strongly correlated with a high concentration of this sugar, but also sucrose is found in high concentration in certain organisms in their anhydrobiotic state. Anyhow, trehalose appeared to be particularly effective in stabilizing this state of "Life without water".

This concept of fluctuations between a large number of different conformations in a hierarchically structured energy landscape has been thoroughly studied over the past decades, both theoretically and experimentally, for well-characterized protein complexes, such as myoglobin as a paradigm system for globular proteins. And the Swiss-American physicist Hans Frauenfelder from the University of Illinois at Urbana-Champaign, later at Los Alamos National Laboratory, was a key figure in this field. He was born July 28, 1922, he died July 10, 2022 in Tesuque, New Mexico, shortly before celebrating his 100th anniversary. To quote a wise contemporary of his, Richard Feynman (1918–1988):

"… everything that living things do
can be understood in terms of
the jigglings and wigglings of atoms."

The control exerted on the RC dynamics and ET kinetics by the fluctuations of the cofactor environment could be clarified within the framework of the "unified model of protein dynamics" developed by Hans Frauenfelder and his co-workers. In particular, the RC from the purple bacterium *Rb. sphaeroides* provides a privileged model system for exploring the relationships between electron-transfer processes and protein conformational dynamics.

2.2.2 Electron–Electron Dipolar Spectroscopy

The determination of distance and orientation of protein domains and their changes in the course of biological action is of primary concern in proteomics to elucidate the relation between structure, dynamics and function. A variety of biophysical techniques have been developed and applied to measure distances (and orientations) between spin centers in large biosystems. Often, these systems are available only as disordered samples as frozen solutions so that X-ray crystallography is not applicable. For paramagnetic disordered systems, however, EPR spectroscopy offers powerful tools to obtain structural information over wide distance ranges. They are based on dominating anisotropic spin interactions. By this approach, established techniques like FRET (fluorescence energy transfer) or solid-state NMR are complemented in terms of distance ranges. For anisotropic electron–nuclear hyperfine interactions, as is preferentially measured by ENDOR techniques, the accessible distance range stays well below 1 nm (10 Å). For dominating dipolar electron–electron interaction, however, when measured by specialized microwave pulse sequences in pulsed electron–electron double resonance (PELDOR) techniques, the distance range can be dramatically extended, in ideal cases to about 8 nm (80 Å) [257], in proteins realistically to about 5 nm (50 Å). This means that even distances between cofactor radicals and radical pairs across photosynthetic membranes can be measured! This is good news for in-depth electron-transfer studies of primary photosynthesis (see below).

For large distances between well-localized electron spins A and B in a radical pair, for which the point-dipole approximation holds and the exchange coupling, J, can be neglected, the electron–electron dipolar Hamiltonian, $\widehat{H}_{ss}$, is commonly written as

$$\frac{\widehat{H}_{ss}}{h} = -\frac{\mu_0}{4\pi \cdot h} \cdot \frac{g_A(\theta_A, \varphi_A) \cdot g_B(\theta_B, \varphi_B) \cdot \mu_B^2}{r_{AB}^3} \cdot (A + B + C + D + E + F), \tag{20}$$

where $g_A(\theta_A, \varphi_A)$, $g_B(\theta_B, \varphi_B)$ are the orientation-dependent g-values of radicals A and B selected by the external magnetic field B_0, μ_B is the Bohr magneton, μ_0 the vacuum permeability, and h the Planck constant. In analogy of the Hamiltonian of the anisotropic part of the electron–nuclear hyperfine interaction (see Eq. 7), the six terms $A, B, ..., F$ represent products of spin-component operators and angular expressions in a spherical coordinate system $(r_{AB}, \theta, \varphi)$, in which r describes the radial distance of spin B from spin A located at the origin (or vice versa). The zenith and azimuth polar angles θ and φ describe the orientation of the radical-pair axis with respect to the external Zeeman field B_0 [258]:

$$\begin{aligned}
A &= \widehat{S}_z^A \cdot \widehat{S}_z^B \cdot \left(3\cos^2\theta - 1\right), \\
B &= \tfrac{1}{4} \cdot \left(\widehat{S}_+^A \cdot \widehat{S}_-^B + \widehat{S}_-^A \cdot \widehat{S}_+^B\right) \cdot \left(3\cos^2\theta - 1\right), \\
C &= \tfrac{2}{3} \cdot (\widehat{S}_+^A \cdot \widehat{S}_z^B + \widehat{S}_z^A \cdot \widehat{S}_+^B) \cdot \sin\theta \cdot \cos\theta \cdot e^{-i\varphi}, \\
D &= \tfrac{2}{3} \cdot (\widehat{S}_-^A \cdot \widehat{S}_z^B + \widehat{S}_z^A \cdot \widehat{S}_-^B) \cdot \sin\theta \cdot \cos\theta \cdot e^{i\varphi}, \\
E &= \tfrac{3}{4} \cdot \widehat{S}_+^A \cdot \widehat{S}_+^B \cdot e^{-2i\varphi}, \\
F &= \tfrac{3}{4} \cdot \widehat{S}_-^A \cdot \widehat{S}_-^B \cdot e^{2i\varphi}.
\end{aligned} \tag{21}$$

The $\widehat{S}_x^{A(B)}$ and $\widehat{S}_y^{A(B)}$ spin operators are expressed in terms of the raising and lowering shift operators $\widehat{S}_+^{A(B)}$ and $\widehat{S}_-^{A(B)}$. Note the formal analogy of the electron–electron dipolar interactions with the electron–nuclear dipolar (END) interaction discussed above. Following the same arguments as used for the END hyperfine interaction [1], in high magnetic fields, when the dipolar coupling of the two unlike electron spins is small compared to the difference of their Zeeman interactions, the dipolar splitting of the EPR transitions is predominantly determined by the ''secular'' $\widehat{S}_z^A \cdot \widehat{S}_z^B$ term A in Eq. (7), whereas the ''pseudo-secular'' $\widehat{S}_{+(-)}^A \cdot \widehat{S}_{-(+)}^B$ term B can be neglected to first order. The ''non-secular'' terms C, D, E, and F are not important at all for the dipolar energy splitting [137].

The pseudo-secular term becomes important in the case of like spins, i.e., when the dipolar coupling is large compared to the difference of their Zeeman interactions. This leads to a scaling of the dipolar coupling frequency by a factor of 3/2 as compared to the case of unlike spins [124]. The intermediate case with comparable magnitudes of the dipolar coupling and Zeeman splitting is more complex, and adequate data analysis requires simulation of the spectra on the basis of the full spin Hamiltonian of the molecular system, including both secular and pseudo-secular terms of the dipolar interaction. When working at a particular microwave frequency, the validity of the unlike-spin limit is guaranteed only for a large enough distance of the spins, e.g., $r_{AB} \geq 2$ nm (20 Å) at X-band [124]. In the case of a pair of two nitroxide radicals, which are frequently used for distance measurements on doubly site-specifically labeled proteins, the two nitroxide spins usually have their Zeeman (and hyperfine) frequencies substantially different and, hence, fulfill the condition

of the unlike-spin limit. The difference in resonance frequencies of the two radicals arises from their different orientations with respect to the Zeeman field $\vec{B}_0$, so that the effective g- and hyperfine-values of their g- and hyperfine- tensors are different.

Neglecting the exchange coupling, in the unlike-spin limit the dipolar coupling frequency, ν_{AB}, is given by

$$\nu_{AB}(\theta) = \nu_d \cdot \left(1 - 3cos^2\boldsymbol{\theta}\right), \tag{22}$$

with the dipole–dipole coupling parameter $\nu_d = \frac{\mu_0}{4\pi \cdot h} \cdot \frac{\mu_B^2 \cdot g_A \cdot g_B}{r_{AB}^3}$.

Here, the g_A and g_B values of the radical partners A and B are the weighted principal components of their g-tensors, i.e., weighted according to their orientations in the pair, r_{AB} is their distance and θ the angle between the Zeeman field B_0 and the interspin distance vector r_{AB}. For an isotropic distribution of angles θ, i.e., isotropic frozen sample without orientational selectivity of the experiment, a characteristic powder-type spectrum, the ''Pake pattern'', is obtained. From this, r_{AB} can be deduced, provided g_A and g_B are known from independent EPR experiments. At sufficiently good signal-to-noise ratio, the dipole–dipole coupling parameter ν_d can be directly read off from the singularities of the Pake pattern.

The methodological challenge is to devise an EPR strategy that separates the electron–electron coupling from other interactions, such as electron–nuclear hyperfine interactions and inhomogeneous line broadening. Common to most electron–electron dipolar EPR methods for weakly coupled radical-pair systems, in which the dipolar coupling is smaller than the cw EPR linewidth, is the electron spin echo (ESE)-detected mode of operation. It is an inherent strength of the ESE method that it is ''blind'' toward static energy contributions, thus eliminating the masking effects of any source of inhomogeneous EPR line broadening [259]. Only when the interactions become time-dependent and, thus, contribute to T_2 relaxation of the spin system, they determine the spin-echo formation. In cases of anisotropic spin interactions, such as electron–nuclear dipolar or quadrupolar interactions or electron–electron dipole interaction, the echo amplitude may become modulated (ESEEM, spin echo envelope modulation) when the time between the pulses in the echo sequence is varied.

In a biradical with interspin distances less than 80 Å the modulation pattern is often determined by the electron–electron dipole coupling frequency. The inhomogeneous broadening of nitroxide lineshapes from unresolved intramolecular proton or deuteron hyperfine interactions must be considered when extracting relaxation data from cw spectra, whereas the ESE measurements are independent of any source of inhomogeneous broadening.

The pulse electron–electron dipolar spectroscopy was originally introduced 1981–1984 in Novosibirsk as a 3-pulse method employing two microwave frequencies [64, 260–264] to measure weak electron–electron dipolar couplings from ESE decays. It soon received the acronym PELDOR (pulsed electron–electron double resonance). About a decade later, in 1993, the first publication on pulse electron–electron dipolar spectroscopy appeared from outside Novosibirsk [265]; the authors discussed orientational selection and created the acronym DEER (double electron–electron resonance). In the 4-pulse DEER method [65], an additional

refocusing mw pulse is introduced that provides dead-time free data collection. As the evolution of electron double quantum coherence (DQC) also depends on the electron dipole–dipole interaction, a powerful 6-pulse DQC method was introduced by the Freed group at Cornell [266, 267]. Commonly used pulse EPR schemes as well as dedicated cw EPR experiments for distance measurements are described in many review articles and books, for example in the anthology *Distance measurements in biological systems by EPR,* edited by L. J. Berliner, G. R. Eaton and S. S. Eaton [63]. In this book, experts in the field report in detail about the pros and cons of distance measurements by cw and pulse EPR methods when applied to a broad variety of biological two-spin systems. They range from organic radicals and transition-metal ions to dipolarly coupled nitroxide spin labels, to donor–acceptor cofactor radical-ion pairs in photosynthetic reaction centers. An important book covering in depth the subject of distance measurements by electron dipolar spectroscopy is the monograph *Principles of pulse electron paramagnetic resonance* by A. Schweiger and G. Jeschke [33]. Several excellent reviews have appeared in the last few years covering both methodologies and applications of pulse dipolar EPR spectroscopy, primarily on structural biology of spin-labeled systems which have attracted growing attention, for example [122–124, 268–273].

The high-field extension of 3-pulse PELDOR, which was developed with the aim to resolve the relative orientation of the radical-pair partners, is very powerful for large protein systems [128]. Also the conceptually related, but single-frequency dipolar spectroscopy method RIDME (relaxation-induced dipolar modulation enhancement) [67] has been extended to high magnetic fields and microwave frequencies. Interesting RIDME applications have been reported already, for example at 130 GHz on nitroxide biradicals [274] or at 95 GHz on donor–acceptor radical pairs in photosynthetic reaction centers [128].

Here, we will briefly describe a few aspects of PELDOR and RIDME at high Zeeman fields that are pertinent for measuring both distance and relative orientation of radical-pair partners. Orientation resolving high-field PELDOR (or DEER) experiments have been pioneered independently by three research groups: the

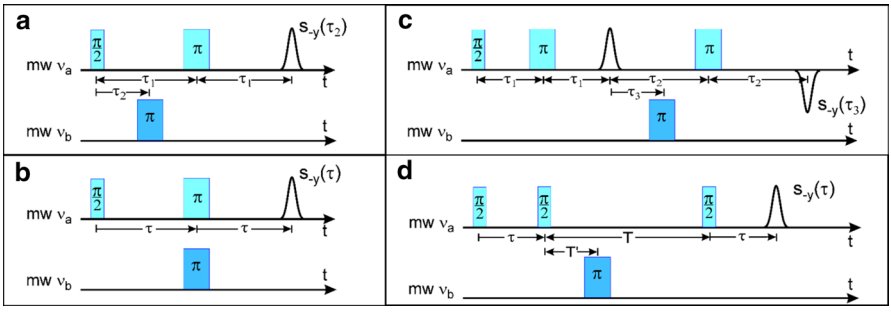

Fig. 19 The most important dual-frequency pulse schemes of pulse electron–electron double resonance. **a** 3-pulse constant-time PELDOR [64]; **b** 3-pulse variable-time PELDOR; **c** 4-pulse constant-time PELDOR (DEER) [65]; **d** 4-pulse variable-time PELDOR, all based on a stimulated-echo sequence [128, 276]

Prisner group in Frankfurt [125, 126, 275], the Jeschke group, then in Konstanz [127], and the Möbius group in Berlin [128, 152].

2.2.2.1 PELDOR Figure 19 shows the most prominent pulse schemes typically employed for dual-frequency PELDOR (or DEER) experiments. The 3-pulse version was first introduced by A. D. Milov, K. M. Salikhov, M. D. Shirov [261], see Fig. 19a. It is analogous to the SEDOR (spin-echo double resonance) sequence used in solid-state NMR to detect the coupling between two nuclear spins [277]. In this sequence, a 2-pulse Hahn echo sequence at ν_a with a fixed pulse separation time τ_1 is involved to selectively detect the echo intensity of the radical A of the A-B radical pair. An additional microwave pulse at time τ_2 after the first pulse and at the microwave frequency ν_b flips the B spin by 180°. If the spins A and B are coupled by dipolar interaction, the detected echo intensity becomes modulated when varying τ_2. The interaction frequency ν_{AB} is obtained by Fourier transformation of the echo time trace.

Our strategy for high-field PELDOR spectroscopy is as follows: We use the 3-pulse stimulated-echo (SSE) sequence, in which the mw pulses are frequency adjusted to the observer spins A, and apply within the mixing period between the SSE pulses an additional mw π-pulse in resonance with the partner spins B to flip them, see Fig. 19d. The PELDOR-time trace is obtained measuring the SSE echo intensity at different τ values and using the "reference-signal deconvolution" technique. The reference time trace is obtained by simply skipping the π-pulse at ν_b. Dividing the trace with the additional π-pulse by the reference trace yields the pure dipolar evolution function. When performed at stepped resonance field positions of both excitation sites within the spectra of the coupled radicals A and B, this strategy allows to find the particular field positions in the EPR spectrum that are conjugated by dipolar interaction between the A and B spins of the radical pair. For a detailed discussion of this strategy, see [1]. Orientational information on radicals in disordered solids is, of course, only available at a sufficient degree of orientation selectivity in the EPR spectrum. Therefore, PELDOR experiments in high-field EPR spectroscopy with adequate Zeeman magnetoselectivity appear to be a promising approach for structure determination of disordered protein systems [128].

An obvious problem is the excitation bandwidth which must exceed the dipolar coupling, since both EPR lines of the dipolar doublet of a given A or B spin have to be excited. This means that in dual-frequency (DF) PELDOR experiments, the pump pulse at the second resonance frequency ν_b must excite a significant fraction of B spins that are dipole-coupled to the observer spins A, whose resonance frequency is ν_a. In high-field EPR, the spectral width of the two radicals in the weakly coupled pair increases in proportion to their difference in g-values and applied Zeeman field. Fortunately, the bandwidth of the EPR resonator also increases with high mw frequency. Even for a single-mode cavity with high Q value, a bandwidth of 100 MHz was achieved at 95 GHz (W-band). This is sufficient for accommodating both ν_a and ν_b for donor–acceptor radical pairs in photosynthesis, but not for nitroxide spin-labeled radical pairs. W-band EPR spectra of nitroxide radicals are typically spread over a range of 400 MHz as compared to 200 MHz at X-band. We, thus, see that DF-PELDOR at W-band is applicable for donor–acceptor ion radical pairs in

photosynthesis, and detailed information of interspin distance and orientation of the charge-separated cofactors in the photocycle could be obtained [128].

Here is an interesting example:

Example: Conformational changes during light-induced electron transfer in photosynthesis

The chosen example of applications of high-field EPR and PELDOR spectroscopy mirrors our fascination for one of the great intellectual challenges of biology, the separation of charges induced by light, which is essential for photosynthesis and, hence, Life on Earth. New research advances the understanding of microbial photosynthesis provides new insight into the atomic structures and synthesizing mechanisms of key photosynthetic proteins. The capture of the sun's energy through photosynthesis in distinct photosynthetic organisms is the fundamentals of almost all life on Earth. Under the current circumstances of global climate change and food/energy crisis, there has been a revival of considerable interest in studying how photosynthetic bacteria and plants trap and convert solar energy in nature.

The reaction center (RC) of the purple photosynthetic bacterium mutant *Rhodobacter (Rb.) sphaeroides* R26 is a pigment–protein complex that is capable of converting light energy to chemical energy with quantum yield approaching 1. Electron transfer (ET) in this RC has been extensively studied; the structure and spectroscopic features of the complex are well known, the complex is very stable, and a large variety of mutants is available in addition to the wild type (WT). This RC also serves as a model system for understanding protein–cofactor interactions and the

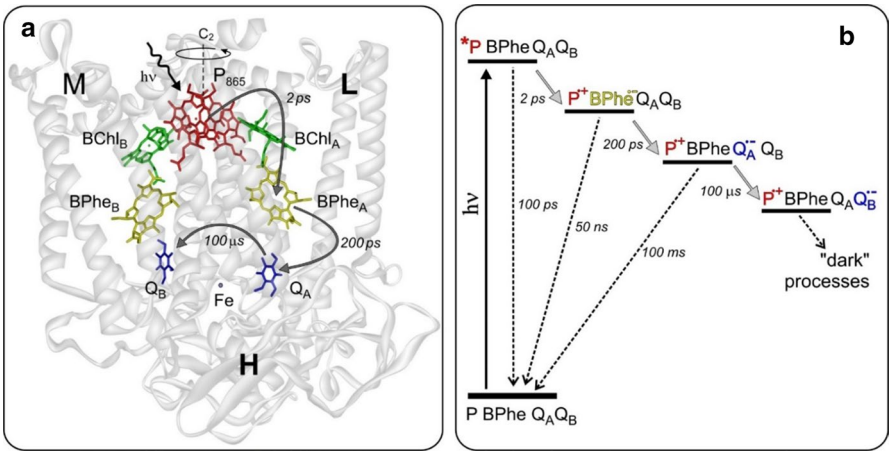

Fig. 20 **a** X-ray structural model of the RC from the photosynthetic purple bacterium *Rb. sphaeroides* R26 [279] composed of the protein subunits L, M, H and the cofactors P_{865}, BChl, BPhe, Q and Fe (P_{865}, primary donor "special pair" of bacteriochlorophyll *a* (BChl *a*); BPhe, bacteriopheophytin *a*; Q, ubiquinone acceptors Q_A, Q_B; Fe, non-heme iron Fe^{2+}). Light-induced electron transfer (ET) for charge separation proceeds predominantly along the A branch of the protein-embedded cofactors ("unidirectionality" enigma) despite the approximate C_2 symmetry of the cofactor arrangement. For the EPR experiments reported here, the non-heme high-spin iron Fe^{2+} in the RC was replaced by diamagnetic Zn^{2+} to avoid magnetic interaction with the iron. **b** The ET time constants range from 2 ps to 100 µs in the cascade of transmembrane charge-separation steps. For details and references, see overview [1]

role that protein plays in ET [278]. The RC from *Rb. sphaeroides* comprises 3 protein subunits, H, M, and L. As shown in Fig. 20, the RC complex binds 9 cofactors that form 2 potential ET chains (referred to as A and B) in a C_2 symmetric arrangement. The "special pair" (P_{865}) is a dimer of bacteriochlorophyll (BChl) *a* molecules and is located on the periplasmic side of the cytoplasmic membrane. Two monomeric BChls ($BChl_A$ and $BChl_B$, with the subscripts denoting which chain the cofactor belongs to) are present on either side of P_{865}. These are followed by 2 bacteriopheophytin (BPhe) molecules ($BPhe_A$ and $BPhe_B$). A non-heme iron Fe and 2 quinones (Q_A and Q_B) are near the cytoplasmic side of the RC. When P is excited by actinic light, an electron is transferred through the A branch cofactors, and then to Q_B. In the WT RC, the times for ET from *P to $BPhe_A$ to Q_A to Q_B are 3 ps, 200 ps, and 200 μs, respectively. The transfer from *P to $BPhe_A$ is thought to be via $BChl_A$, but this is still a controversially debated issue.

Photosynthesis generally starts with photon absorption by light-harvesting antenna. The absorbed energy is then rapidly and efficiently transferred to a reaction center (RC) for charge separation. Purple bacteria are the oldest photosynthetic species and carry out anaerobic photosynthesis in diverse ecological niches. In purple bacteria, light-harvesting 1 (LH1) complexes often associate with the RC to form a RC-LH1 core supercomplex, containing a high content of non-covalently attached pigments such as bacterial chlorophylls and carotenoids, to increase the effective cross section for light absorption of each RC. This then supports photosynthesis to operate effectively over a wide range of environmental light intensities and wavelengths. For example, purple bacteria are highly efficient in utilizing green and far-red light of wavelengths above 750 nm that plants and algae do not utilize.

Due to the simplicity of the photosynthetic machinery and ease of growth, anaerobic purple photosynthetic bacteria have been used to study the fundamental mechanisms of photosynthesis. For decades, X-ray crystallography has been used by structural biologists to solve the structural composition of water-soluble "globular" protein complexes. But not of water-insoluble membrane proteins, which were considered non-crystallizable. In 1982, Hartmut Michel (Munich) succeeded in crystallizing the photosynthetic reaction center of the purple bacterium *Rhodopseudomonas viridis*, thus creating the basis for a molecular X-ray crystal structure analysis of a membrane protein complex. The Nobel Prize in Chemistry 1988 was awarded to H. Michel, J. Deisenhofer, and R. Huber for their contributions to crystallize the membrane protein and determine the high-resolution X-ray structure of the RC of a photosynthetic purple bacterium. It is noted that over the past few years, the cutting-edge cryo-electron microscopy (cryo-EM) technology has revolutionized the structural understanding of photosynthetic RC-LH1 complexes in a variety of purple bacteria.

The flexibility of the quinone binding site in the RC of *Rb. sphaeroides* R26 has initiated speculations about its functional role in the charge-separation/charge-recombination electron-transfer cycle. For example, such speculations related to potential structural changes associated with Q_A reduction were fostered by an early observation by D. Kleinfeld, M. Y. Okamura and G. Feher [255] who showed by optical spectroscopy that the rate of recombination from the transient radical-pair

state $P^{\cdot+}_{865}Q^{\cdot-}_{A}$ to the ground state $P_{865}Q_A$ differs in RCs cooled to cryogenic temperatures in the dark (dark-adapted RCs) compared to RCs cooled under continuous illumination (light-adapted RCs) [255]. The authors explained the slower recombination kinetics in the light-adapted sample by suggesting changes of the donor–acceptor average distance (by ≈1 Å) and of its distribution. However, by using FTIR spectroscopy Breton and co-workers showed that near room temperature Q_A does not move significantly upon reduction with respect to its protein binding site [280]. To obtain structural information at lower temperatures transient and pulsed EPR studies were performed [281, 282]. No significant changes in the donor–acceptor distance and its distribution were observed by Zech et al. [281] using X- and Q-band transient direct-detection cw EPR and out-of-phase electron spin echo (ESE) experiments. On the other hand, Borovykh et al. [282] deduced by X-band electron spin echo envelope modulation (ESEEM) that the donor–acceptor distance in the sample frozen under illumination is slightly larger (≈ 0.4 Å) than that in the sample frozen in the dark. Potential light-induced structural changes associated with the charge-separated state, $P^{\cdot+}_{865}Q^{\cdot-}_{A}$, have also been investigated by X-ray diffraction on single-crystal RCs frozen either in the dark or under continuous illumination [283]. In contrast to the secondary quinone Q_B (see ref. [284]) the X-ray crystallography results for Q_A showed no significant changes, within the error margin (≈ 0.2 Å), neither in the donor and primary acceptor positions nor in their orientations [283, 285]. A few years ago, Heinen et al. [286] proposed from quantum-beat oscillations of transient Q-band EPR signals (T = 70 K) of radical pairs $P^{\cdot+}_{865}Q^{\cdot-}_{A}$ in dark-adapted RCs that an unprecedented reorientation of $Q^{\cdot-}_{A}$ by as much as 60° upon light-induced charge separation occurs. The authors concluded that this large difference in orientations reflects a rotation of the quinone in its ring plane that is caused by structure accommodation to the charged configuration of the acceptor binding site. At variance with this suggested model [286], Savitsky et al. [128] and Flores et al. [287] concluded from their orientation-resolving W-band PELDOR and Q-band ENDOR studies (at T = 150 K) of the transient $P^{\cdot+}_{865}Q^{\cdot-}_{A}$ radical pair that no large rearrangement at the Q_A site occur under illumination, see below. We want to point out that we believe that the discrepancy between the studies of refs. [128, 286, 287] is rooted in the inherent sign ambiguity of the measured squares of any spin-interaction tensors and degeneracy of structure solutions, and that in ref. [286] the wrong sign was chosen. The important issue of finding a unique solution for the spin-interaction tensor orientation is thoroughly discussed in [1] to which we refer for further reading.

The problem of finding the unique structure solution in the specific case of the quinone acceptor orientation after light-driven charge separation was solved by comparing the PELDOR and ENDOR spectra of RCs frozen under illumination with those of RCs frozen in the dark before illumination [128, 281, 282, 287], and doing so under otherwise identical conditions. While PELDOR gives information of the global structure of the dipolarly interacting radical pairs, ENDOR gives direct information on the local environment of the radicals via their electron–nuclear hyperfine interactions. As has been shown previously [140, 141, 288–290], ENDOR is exquisitely sensitive to probe protons H-bonded to quinones in bacterial RCs.

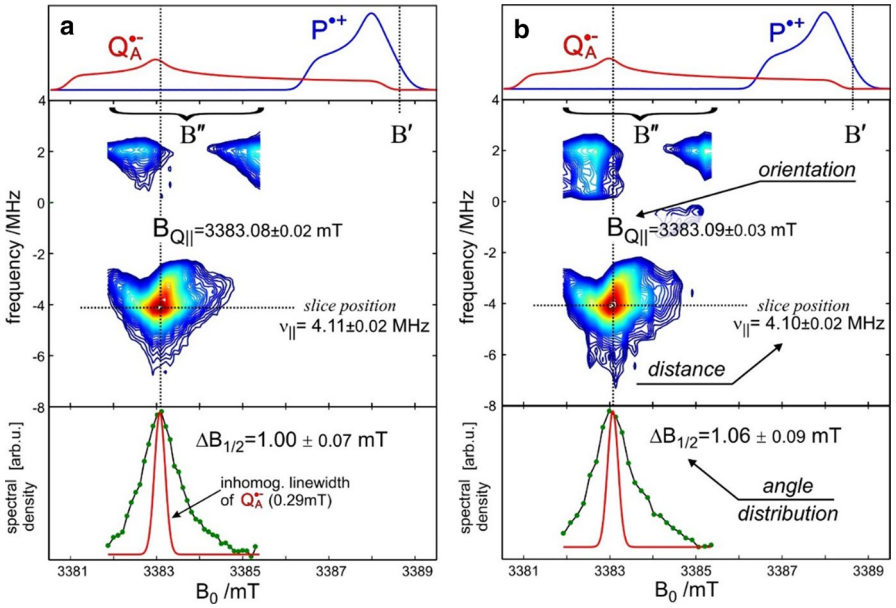

Fig. 21 W-band PELDOR spectra of the spin-correlated radical pair $P_{865}^{+}Q_A^{-}$ in Zn-substituted RCs from *Rb. sphaeroides* at 90 K, **a** in the sample frozen in the dark, **b** frozen under continuous illumination. Only those PELDOR responses are shown that were used to probe the spectral position, $B_{Q||}$, within the Q_A^{-} EPR spectrum corresponding to the parallel dipolar frequency, $\nu_{||}$. The observer mw frequency is fixed at the value corresponding to the field value B', while the pump mw is swept through the field region B''. Upper part: The individual EPR spectra of P_{865}^{+} and Q_A^{-} are shown for referring to the spectral positions. Middle part: Contour plot of the positive Fourier amplitudes of the PELDOR echo decays. Lower part: The contour-plot amplitude (at the slice position) vs magnetic field is shown (dots). The inhomogeneously broadend (intrinsic) EPR linewidth (red line) is 0.29 mT (note that the RC is fully deuterated allowing for such a narrow linewidth). The broadening of the PELDOR lines (width$\Delta B_{1/2}$) is due to the orientational distribution of Q_A^{-}. For further explanations, see refs. [128, 291]

In the following, we briefly summarize the results of such PELDOR and ENDOR experiments on $P_{865}^{+}Q_A^{-}$ and Q_A^{-} in RCs from *Rb. sphaeroides* [291]. The experiments are part of a larger research project related to the important question of whether the high quantum yield of photosynthetic primary electron-transfer processes are due to light-induced structural changes of the cofactor binding sites.

In Fig. 21, the PELDOR results for the dark-adapted and light-adapted RCs are summarized. The parameters $\nu_{||}$ and $B_{Q||}$, which are highly specific for the radical-pair structure ($\nu_{||}$ for the distance, $B_{Q||}$ for the orientation, see ref. [128]), can be directly read off from the PELDOR spectra. The values $\nu_{||} = 4.11 \pm 0.02$ MHz and $B_{Q||} = 3383.08 \pm 0.02$ mT for the dark-adapted sample fully agree with $\nu_{||} = 4.10 \pm 0.02$ MHz and $B_{Q||} = 3383.09 \pm 0.03$ mT for the light-adapted sample. Also, the angular distribution width, $\Delta B_{1/2}$, is the same within experimental error. This implies that neither the interspin distance in the radical pair nor the relative orientation of donor and acceptor ions is different for the different illumination-freezing

protocols. In other words, from PELDOR we learn that there is no conformational redistribution of Q_A under light-driven reduction.

This conclusion is fully supported by the Davies-type pulsed Q-band ^{1}H ENDOR experiment [291]: In the dark-adapted and light-adapted RCs, the ENDOR spectra of $Q_A^{\cdot-}$ are identical within experimental error. The ENDOR results irrefutably show that independent of the history of the freezing and illumination of the RCs, $Q_A^{\cdot-}$ remains linked to the protein by two asymmetrical H-bonds from His M219 and Ala M260 to the carbonyl oxygens. This conclusion is consistent with earlier ENDOR measurements [141] and DFT calculations [292] of the H-bonding network of the quinone acceptor. For further arguments in support of this conclusion, the reader is referred to ref. [291]. Clearly, further studies will be needed to fully understand the underlying strategies for fine-tuning the efficiency of primary electron transfer in photosynthesis.

As we have seen, high-field DF-PELDOR at W-band is well suited to elucidate the three-dimensional structure of the charge-separated radical pair $P_{865}^{\cdot+}Q_A^{\cdot-}$ in primary photosynthesis. The situation may be different for two-spin systems of nitroxide biradicals for which W-band EPR spectra are typically spread over a range of 400 MHz. For such systems, an alternative to high-field DF-PELDOR would be W-band field-jump (FJ)-PELDOR. Logically, in our laboratory at FU Berlin, we have built a powerful field-jump unit and attached it to our W-band spectrometer [1, 276]. The pulsed magnetic field of 16 mT at the sample inside the TE_{011} EPR cavity, made from Ti–6Al–4V alloy to reduce unavoidable eddy currents, is generated by a pulsed electric current (70 A) flowing through a pair of Helmholtz coils that are fixed outside the cavity and replace the field modulation coils. The screening field from eddy currents in the cavity was found to decay with a time constant of 110 ± 10 ns in the Ti–6Al–4V cavity, i.e., an order of magnitude faster than in the brass cavity of the same geometry. Thus, to satisfy the requirements for FJ-PELDOR experiments (to achieve a stable peak-field value and to avoid residual fields after switching off) with the Ti–6Al–4V cavity, a duration of the field jump of about 700 ns and an after-pulse delay of 500 ns are estimated which determine a minimum stimulated-spin-echo (SSE) mixing time interval T of about 1 μs. This pulse pattern already allows FJ-PELDOR experiments in high magnetic fields to be made for the determination of nanometer distance and relative orientation of nitroxide spin labels in disordered samples [276].

2.2.2.2 RIDME In the 3-pulse stimulated-echo sequence in resonance with the observer spins A, the partner spins B can flip also spontaneously by their longitudinal relaxation that occurs during the mixing period (interval T between the 2nd and 3rd microwave pulses). This relaxation mechanism is exploited in RIDME spectroscopy which can, thus, be considered as a single-frequency variant of dipolar spectroscopy in which T_1 relaxation substitutes the coherent mw irradiation in PELDOR to flip the B spins by 180° (π). Similar to PELDOR, the RIDME experiment yields an echo-decay time trace in which the dipolar coupling between the A and B spins shows up as a modulation with the period of the inverse dipolar frequency.

Certain conditions have to be met for the RIDME experiment to operate as a function of the preparation time τ: The fixed mixing time T should be long enough to allow the longitudinal spin relaxation to flip the partner spins in the pair, but short enough to avoid a considerable reduction of the echo signal caused by the longitudinal spin relaxation of the observer spins. The fraction of B spins flipping an odd number of times is given by the inversion factor [67]

$$q_{inv} = \frac{1}{2} \cdot \left(1 - e^{-\frac{T}{T_1}}\right), \tag{23}$$

where T_1 is the spin–lattice relaxation time. Under the conditions $T_1 >> \tau$ and $(T_1 \cdot \nu_{AB})^2 >> 1$, the stimulated-echo amplitude as a function of inter-pulse time τ is given [67] by

$$s_{-y}(\tau) = A_1(\tau) \cdot A_2(T) \cdot \left[1 - q_{inv} + q_{inv} \cdot \cos\left(2\pi \cdot \nu_{AB} \cdot \tau\right)\right], \tag{24}$$

where the relaxation factors $A_1(\tau)$ and $A_2(T)$ describe the echo decay because of transversal and longitudinal relaxation of the observer spins. Thus, measuring the echo amplitude will exhibit a periodic oscillation with dipolar frequency ν_{AB}. Unfortunately, hyperfine modulations can obscure the RIDME effect. Therefore, RIDME experiments are best performed at high magnetic fields and microwave frequencies, where hyperfine modulations are strongly reduced [128, 274].

If the RIDME experiment is performed successively at different field positions within the partially Zeeman-resolved EPR spectrum of the two radicals of a coupled pair, it can reveal the specific field positions at which the dipolar modulation occurs at the principal values, $\nu_{||} = \nu(\theta = 0)$ and $\nu_{\perp} = \nu(\theta = \pi/2)$, of the dipolar frequency. Magnetoselection at these field positions establishes correlations between the polar angles $(\eta_{A(B)}, \phi_{A(B)})$ that define possible orientations of the dipolar axis in the molecular frame of radicals in the pair.

The main advantage of the RIDME method is its simplicity as compared to PELDOR because it is based just on a single-frequency stimulated-echo pulse sequence. It can be performed with any pulsed EPR spectrometer without needing dual-frequency or field-jump extensions. Moreover, a large modulation depth, even at high-field EPR, can be reached because the inversion factor q_{inv} depends only on the time T in the stimulated-echo sequence.

The main disadvantage of the RIDME method is the partial loss of orientational selectivity. It can be a difficult task to assign the observed modulations to a specific radical in the radical pair, especially if the radicals are identical or their EPR spectra strongly overlap. Additionally, the success of a RIDME experiment depends on the proper choice of experimental conditions, in particular of the sample temperature. The dipolar modulations are enhanced in the case of a pure T_1 relaxation process, see Eq. (23), but the decay of stimulated-echo intensity can be governed by additional mechanisms, for example spectral diffusion [293]. For details concerning our 95 GHz high-field PELDOR and RIDME experiments on transient radical pairs in bacterial photosynthetic reaction centers, see [128] and [1].

3 Instrumentation

EPR spectroscopy, like any other spectroscopic method, must meet three main requirements to be useful as an analytical tool: (i) detection, (ii) identification, and (iii) characterization of the specimen. That means, first of all, the method should be sensitive enough to detect fingerprint signals of the system under investigation. The second step is the assignment of the observed signals to one or more species in the sample or, vice versa, identification of the species from the observed signals. The third step is the characterization of the species in their molecular environment using specific spin-interaction parameters that are extracted from the observed EPR signals.

Historically, EPR spectroscopy had to go a long way to fulfill these requirements. Sensitive detection methods were being developed but needed decades to reach the present standard. The systematic investigations of a large number of the paramagnetic species provided the knowledge about their spectroscopic properties and allowed to understand the molecular interactions suitable for characterizing the spin system. Finally, sophisticated data analysis techniques were developed and approved which allow EPR spectroscopists to extract the interaction of interest from the complex spectra. In the meantime, EPR spectroscopy is approaching the level of technical development necessary to become a powerful analytical tool, ready to be applied to characterize the investigated systems to hitherto unprecedented details.

While we were writing on this high-field EPR "Instrumentation" section, we realized that a full description of this success story would go far beyond the scope of the present review article. Instead, we decided to refer here to our 2009 book on *High-field EPR spectroscopy on proteins and their model systems* [1], which documents in detail the instrumentation of modern high-field EPR and its chronological development. From this monograph, we will quote only a few distinctive examples.

There are five basic requirements for a high-field/high-frequency EPR spectrometer: (i) A strong homogeneous and stable magnetic field; (ii) Suitable low-noise microwave sources; (iii) The microwave power must be transferred with minimal losses to a resonator with the sample and from the resonator to the detector by means of a suitable mw transmission line; (iv) The resonator must concentrate the incident microwave radiation onto the sample and allow to detect the small amount of energy absorbed when the EPR resonance condition is met; (v) The detector must be able to measure, with high signal-to-noise ratio, the variation of the mw power level in case of EPR absorption.

All considerations concerning the detection schemes at X- or Q-band generally hold also for high-frequency EPR. However, the degradations in the performance of specific spectrometer parts at high mw frequencies put limitations on the spectrometer design and require a careful choice of the components. In [1] individual sections are dedicated to the microwave sources, resonators, transmission lines and magnet systems which have been successfully tested and employed in high-field spectrometer designs of various laboratories. For additional information we refer to review articles dealing in detail with aspects of instrumentation development of high-frequency EPR [108, 110, 114, 131, 294–298].

3.1 The 95 GHz Spectrometer Built at FU Berlin

The W-band high-field EPR spectrometer at FU Berlin was designed as a multipurpose instrument for cw, pulsed and time-resolved EPR, as well as for double resonance experiments (ENDOR, ELDOR). The instrumental development started around 1983. The significant steps forward in the performance and capabilities of the spectrometer up to its present version have been taken predominantly by diploma and PhD students as well as postdoctoral co-workers of the Möbius group. In particular we mention (in chronological order) E. Haindl [75], O. Burghaus [74, 96, 299–301], T. Götzinger [302], M. Rohrer [74, 303–305], R. Klette [245, 306], T. F. Prisner [60, 298, 307], A. Schnegg [308], M. Fuhs [309–311], A. Savitsky [61, 128, 312], and Yu. Grishin [276].

The EPR spectrometer consists of the microwave bridge, the magnet system, the probehead, the cryostat, the control electronics. The mw bridge combines the transmitter, which produces the mw power for continuous or pulsed excitation of the sample, with the receiver for detecting the EPR signal. The external magnetic field is provided by a superconducting magnet which is sweepable to match the EPR resonance condition. The EPR probehead includes the mw cavity, sample holder, mw tuning mechanics, field modulation coils for cw EPR, rf coils for ENDOR. Each component is described in detail in [1]. Particular attention has been paid to the development of probeheads for 95 GHz EPR spectroscopy and its double resonance extensions ENDOR and PELDOR.

When striving for high spectrometer sensitivity at mm wavelengths, incorporation of a microwave resonance structure in the probehead is indispensable. There is no a priory preference for a single-mode cavity, which is commonly used in X- and Q-bands, or a multi-mode Fabry–Perot (FP) resonator, which is commonly used in the submillimeter and optical regions. The choice between these two resonance structures depends strongly on physical and technical considerations related to the type of EPR experiment to be performed. Consequently, both FP resonators and cylindrical single-mode cavities have been designed for our 95 GHz spectrometer.

3.1.1 Fabry–Perot probeheads

Fabry–Perot (FP) resonators have been constructed and tested in several high-field EPR laboratories. Most experimental set-ups use cryomagnets and FPs with vertical B_0 and resonator axes. This configuration, however, is inconvenient for sample access, light irradiation and extension to ENDOR. Hence, we have placed the axis of the FP resonator perpendicular to the B_0 axis [74]. Such a configuration allows to use vertically or horizontally mounted sample capillaries. The simultaneously used Mn^{2+} standard sample for precision magnet field measurements can be adjusted in its position within the FP (see Fig. 22). It consists of two concave spherical mirrors (diameter 13 mm and 19 mm with corresponding curvature radii of 15 mm and 20 mm) in an approximately confocal arrangement (radius of curvature equal to mirror distance). The mirror distance can be tuned by a fine thread to adjust the resonator frequency to the mw source frequency (10 MHz frequency

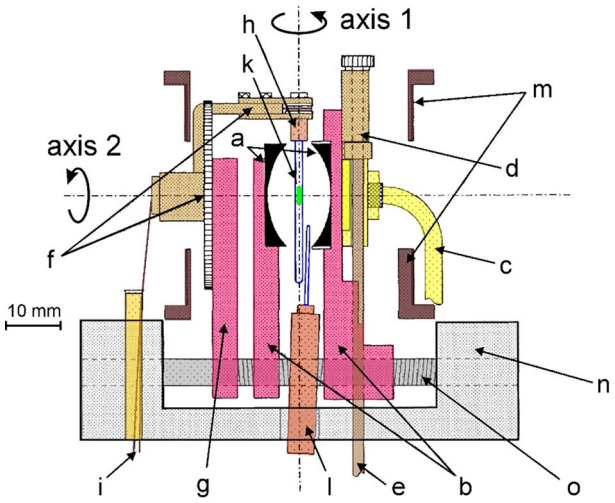

Fig. 22 W-band Fabry–Perot resonator with goniometer with mounted single crystal (shown orientation $B_0 \parallel$ crystal c axis. **a** mirrors (diameter 19 mm, distance ca. 10 mm); **b** mirror supports (synchronously movable for frequency-tuning); **c** WR10 waveguide; **d** microwave coupling unit with **e** drive shaft; **f** goniometer arm with gear for rotation of the arm about the resonator axis; **g** arm support (movable for adjusting the sample in the center of the resonator); **h** rotatable sample holder; **i** thread passing through arm **f** to sample holder **h** for sample-axis rotation; **k** quartz capillary with single crystal; **l** independently adjustable quartz capillary with Mn^{2+} standard sample; **m** modulation coils; **n** holder; **o** guide rod with right/left thread for symmetrical mirror adjustment (frequency-tuning). Rotation axes: axis 1, gear-driven rotation about the resonator axis; axis 2, thread-driven rotation about the sample capillary axis. For details, see [245, 306]

variation for 1 µm distance variation). In most EPR and ENDOR experiments, the fundamental TEM_{00q} with q set from 6 to 9 is preferred. For optimizing the detection sensitivity, the microwave coupling between resonator and waveguide is important. Sufficient coupling dynamics of the FP is achieved by moving a thin dielectric plate (MACOR) partially over the iris in one of the mirrors (for details of construction, see [74]).

The basic realization of the FP probehead allows only rotation of the sample around the sample axis with an accuracy of $\pm 1°$. In a next step, a FP probehead for single-crystal investigations with rotation around three axes by means of a goniometer was developed, Fig. 22. It allows to rotate the sample by 240° around the resonator axis and by 360° around the other two axes with an angular accuracy of better than 0.5° [245]. The FP probehead is equipped with two orthogonal quartz fiber bundles for uniform light excitation while rotating the single-crystal sample.

3.1.2 TE_{011} Cavity Probeheads

The disadvantages of FP resonators in terms of low filling and conversion factors become critical for pulsed high-field EPR experiments with only rather moderate mw power available at high frequencies. This was our motivation behind the

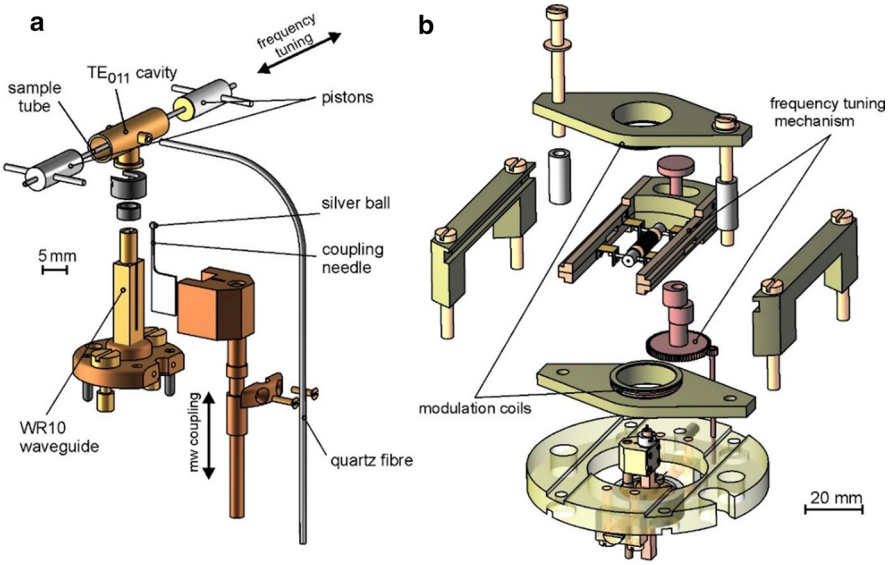

Fig. 23 **a** Exploded view of the 95 GHz EPR TE_{011} optical transmission cavity with microwave-coupling mechanism and light-access chimneys (with minimum mw radiation losses) to insert the quartz-fiber light pipe. **b** Exploded view of TE_{011} (ENDOR variant) probehead with frequency-tuning mechanism and field modulation coils. For details, see [74, 302]

construction of W-band EPR and ENDOR probeheads with cylindrical single-mode cavities. The TE_{011} mode has high filling and conversion factors, and its resonance frequency can easily be tuned by changing the cavity length. The development of cylindrical single-mode cavities for W-band started in our group in 1988 [302]. The first-generation construction design proved to be very reliable in terms of frequency and coupling stability. This design concept is still applied for fabricating new generations of W-band cylindrical cavities without major modifications.

Figure 23a shows exploded views of the W-band EPR probehead. The main elements are the cylindrical TE_{011} cavity optimized for 95 GHz, the frequency-tuning mechanism, the mw coupling mechanism and the field modulation coils. They are mechanically isolated from the cavity in order to avoid microphonics. At 10 kHz they supply up to 2 mT of field modulation amplitude at the sample. The cavity diameter is 4.16 mm. The cavity length can be adjusted to 4.16 ± 1.5 mm (corresponding to TE_{011} mode resonance frequencies from 92 to 104 GHz for an empty cavity). This is done by changing the separation of the two sliding pistons in the cavity by means of a gear drive of high mechanical precision, Fig. 23b. The tuning drive consists of two cam followers 180° out of phase, thereby guaranteeing the maximum of the mw field to stay in the center of the cavity. This is an important requirement for experiments with small single-crystal samples and light excitation. For the different capillary diameters (ID 0.1–1.0 mm), different pairs of pistons are used. On the top of the coupling needle (DELRIN) a small silver ball of 0.7 mm diameter is painted, using a suspension of fine silver flakes (about 8 μm). The coupling needle

can be moved in the upper part of the W-band (WR10) waveguide by means of a vertically sliding mechanism with a high-precision thread drive, Fig. 23a. The iris coupling hole in the middle of the cavity wall has a diameter of 0.8 mm, the wall thickness around the iris is less than 0.1 mm. For different EPR experiments it was necessary to construct different types of cavities. They are commented on in the following:

For pulsed W-band EPR experiments, in which a high B_1 field at the sample position is required, a special TE_{011} cavity with high Q is used. The cavity body was machined from gold (99.9%). Additionally, the brass pistons for the frequency adjustment of the cavity were gold plated (100 μm) at the front side. A room-temperature unloaded $Q_U = 7400$ was measured without sample. This is close to the calculated Q_U value of 8600 when accounting for the ohmic losses in the cavity walls only. At 90 K, $Q_U = 12{,}000$ was determined which is consistent with the room-temperature value taking the known temperature dependence of gold resistivity into account.

For specific EPR experiments in which light irradiation of the sample is required, the standard cw cavity is replaced by an optical transmission cavity, Fig. 23a. It has two symmetrically placed 0.6 mm holes in the cavity wall for the light access furnished with mw chimneys and holding a 0.8 mm thick quartz fiber [304].

For ENDOR experiments, the cw variant of the probehead had to be modified [303]. The standard cw cavity is replaced by a gold-plated bronze TE_{011} cavity, the body of which is slotted with regular slots of 0.3 mm width and 0.6 mm separation to reduce rf-induced eddy currents. The slots slightly reduce Q_U to a typical value of 4000. We use two variants of the ENDOR cavity, one with and the other without light-access holes. The bronze pistons are replaced by pistons machined from MACOR ceramics with gold-plated end faces. The rf ENDOR-coil holder is mounted on the top of the upper field modulation coil. The rf saddle coils around the cavity center produce a rf magnetic field perpendicular to both the external and mw magnetic fields [74].

In field-jump PELDOR experiments [276], the field modulation coils are replaced by field-jump coils of the same geometry. The cavity with dimensions that are adapted from the ENDOR variant is machined from a titanium/aluminum/vanadium alloy and then gold plated [276]. The ENDOR pistons are used for frequency-tuning. The unloaded quality factor of such a cavity configuration is about 3000.

3.2 The 360 GHz Spectrometer Built at FU Berlin

The instrumental development of the 360 GHz EPR spectrometer at FU Berlin has been started in 1995. Several PhD students and postdoctoral co-workers of the Möbius group were involved in this development, in particular M. Fuchs [25, 87, 313], A. Schnegg [152, 314], Yu. Grishin [119, 152] and T. F. Prisner [87]. During the last decade several design improvements of the spectrometer were realized including the pulse EPR and cw ENDOR extensions. The most notable difference of the 360 GHz ($\lambda \approx 0.8$ mm) spectrometer in relation to our W-band spectrometer

is the use of quasioptical microwave components and a corrugated waveguide in the transmission line to the probehead.

3.2.1 Quasioptical Microwave Propagation

The microwave propagation losses in normal metallic waveguides rise rapidly at high frequencies, making standard waveguides unusable above 150 GHz except for very short distances of a few cm. Dielectric fibers and similar "light-pipe" structures can work very well for frequencies in the visible and near-visible spectral region. Unfortunately, they have significant dielectric losses at millimeter waves leading to high damping of the propagated wave. Free space is a low-loss alternative. The damping of millimeter waves in air due to molecular absorption is quantified in dB/km in contrast to dB/m or even dB/cm in classical waveguide systems. The techniques for the propagation of electromagnetic waves over free space are well developed for radiation with wavelengths of less than a micron. Established techniques exist for optical systems for which the characterictic dimensions are many thousand times larger than the wavelength. These systems can be designed and analyzed using the traditional methods of geometrical optics with only rare resort to wave optics. In order to treat millimeter wave systems in the geometrical optics way, one would have to handle optical elements with at least one meter in diameter. Gaussian quasioptics offers a solution to this problem. Quasioptics can be considered as a specific branch of microwave science and engineering. This term is used to characterize methods and tools devised for handling electromagnetic waves propagating in the form of narrow directed beams, whose width w is greater than the wavelength λ, but smaller than the cross-section size, D, of the limiting apertures and guiding structures:$\lambda < w < D$. Normally, $D < 100 \cdot \lambda$, but also devices as small as $D = 3 \cdot \lambda$ can be analyzed using quasioptical principles. In contrast to geometrical optics, which requires $D > 1000 \cdot \lambda$, quasioptics consider both ray-like and diffraction-causing optical phenomena when tracing the beams as they interact with the surfaces of optical elements and the matter in the pathway.

The simplest form of an electromagnetic wave propagating through free space is the Gaussian beam. The fundamental-mode beam has a Gaussian distribution of the electric field amplitude perpendicular to the z-axis of propagation [315, 316]

$$|E(z,r)| = |E(0,r)| \cdot e^{-r^2/w^2}, \tag{25}$$

where r is the distance from the propagation axis and w is the beam radius. The beam radius w will have a minimum value w_0 at a specific place along the beam axis, which defines the beam waist. For a beam of wavelength λ at a distance z along the beam, as measured from the beam waist, the variation of the beam radius is given by

$$w(z) = w_0 \cdot \left(1 + (z/z_0)^2\right)^{1/2}, \tag{26}$$

and the radius of curvature R of the wavefront comprising the beam is

$$R(z) = z \cdot \left[1 + (z_0/z)^2\right], \tag{27}$$

where $z_0 = \pi \cdot w_0^2/\lambda$ is the confocal distance (also called Rayleigh length). Quasioptical elements for propagation of Gaussian beams are waveguides, lenses or mirrors to refocus the Gaussian beam, and antennas or feed-horn systems to transform the waveguide modes to Gaussian modes of propagation. The actual diameters of quasi-optical elements are determined by the boundary values of still tolerable diffraction and beam truncation effects. An element with a single aperture $D = 2 \cdot w$ has a coupling efficiency of 98.8%, i.e., a beam-power loss of -0.05 dB when transmitting a fundamental-mode beam.

The propagation of radiation in a Gaussian beam in free space is independent of its polarization. Thus, generation of beams with different polarizations and manipulation of them with polarization-dependent elements is possible. For example, wire grids with very thin conducting filaments, that are separated by distances less than a wavelength, are very effective polarizers. For radiation with the electric field in the directions of the wires currents are induced, and the grid acts as a reflector. A perpendicularly oriented electrical field does not induce currents, and the radiation passes the grid without attenuation. Proper manipulation of the Gaussian beam

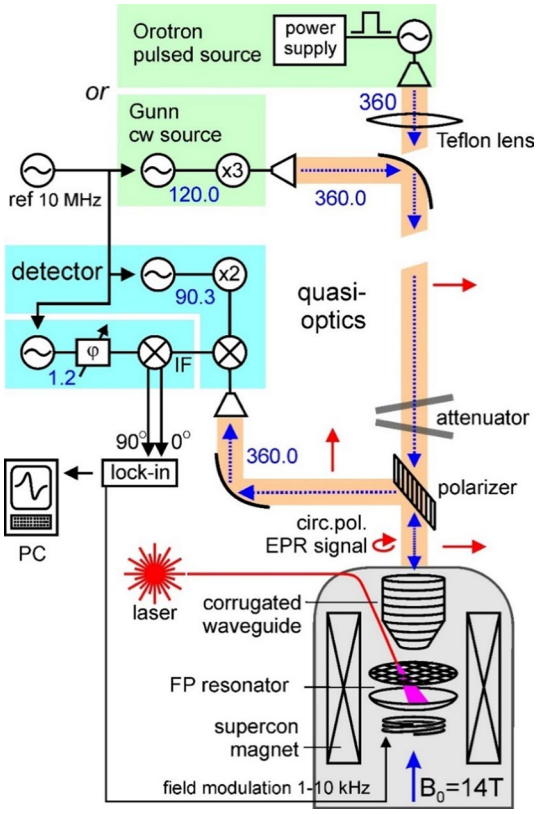

Fig. 24 The 360 GHz EPR spectrometer setup at FU Berlin [313]. The cw Gunn source (green) can be exchanged for the pulsed Orotron source (green) by replacing the first off-axis elliptical mirror for a Teflon lens. In the beam path of the quasioptical bridge (orange), beam propagation directions are indicated by dashed arrows (red) and polarization directions by solid arrows (green). Inside the magnet (gray), the corrugated waveguide, the modulation coil and the semiconfocal Fabry–Perot resonator with mesh coupling are indicated. The EPR-induced microwave signal reflected from the polarizer grid is focused onto the horn of the subharmonic mixer detector (blue). Light excitation is introduced into the probehead via a light guide (red) (color figure online)

polarization allows to construct the quasioptical analogs of corresponding waveguide-based microwave elements such as circulators, directional couplers etc., which become either extremely lossy or even impossible to realize for frequencies above 150 GHz. Detailed descriptions of such quasioptical elements can be found in the monographs by Lesurf [316] and Goldsmith [315]. The engineering and design concepts of quasioptical EPR systems are considered in detail by Gulla and Budil [317], and a transfer matrix method for characterizing and optimizing the performance of quasioptical EPR sample resonators is described by Earle, Zeng and Budil [318].

3.2.2 Microwave-Bridge Design

The general design of the 360 GHz microwave bridge is depicted in Fig. 24. There are three mw sources for sample excitation available. The Orotron source is described in detail in [1]. For pulsed 360 GHz EPR operation, the cw Gunn diode source in the spectrometer can be exchanged for a novel pulsed 360 GHz vacuum-tube source named Orotron (*Gycom*). The Orotron was tailor-made for our 360 GHz EPR studies in a joint German-Russian pilot project supported by the DFG [119]. The acronym Orotron was originally introduced as an abbreviation of the Russian words describing a device with an open resonator, generally a Fabry–Perot resonator, and a reflecting diffraction grating. Conceptually, the Orotron is a non-relativistic free-electron laser using the stimulated Smith–Purcell radiation of a flat electron beam interacting with a periodic grating structure. This acts as one of the mirrors in an over-sized high-quality Fabry–Perot resonator structure to achieve feedback for high output power and frequency stability. The electromagnetic field present in the open FP resonator bunches the electron beam which leads to coherent oscillation [319]. Such open resonator generators were independently developed by F. S. Rusin and G. D. Bogomolov in Moscow, USSR [320] and K. Mizuno and S. Ono in Sendai, Japan [321]. The present tailor-made design extends the traditional cw Orotron by a gate electrode and a high-voltage pulsing unit to control the electron beam current. The generated pulses at 360 GHz have pulse lengths from 100 ns to 10 μs and a pulse power of up to 30 mW. Within a 10 ms time slot, incoherent pulse trains of arbitrary duration can be generated. The pulsed Orotron has been incorporated in the quasioptical microwave bridge of our heterodyne induction-mode 360 GHz EPR spectrometer. First free-induction decay (FID) measurements at 360 GHz and a magnetic field of 12.9 T on a polycrystalline perylene-ion sample were very promising for future applications of the Orotron in EPR spectroscopy under very high-frequency/high-field conditions [119].

In the cw configuration [95, 313], the microwave at 360.03 GHz is generated either by a phase-locked tripled 120 GHz Gunn source (Farran Technology) or by a quadrupled 90 GHz Gunn oscillator (Radiometer Physics). The second cw source can be phase-locked to a 10 MHz oscillator or swept between 358.8 GHz and 361.2 GHz, which allows the precise frequency-tuning of the resonator containing the sample. The output power at 360 GHz is about 1 mW for both cw sources. For detection a heterodyne mixer scheme is employed. The central component of the receiver (Farran Technology) is a subharmonic mixer detector with a detection bandwidth of 100 MHz. In contrast to a fundamental mixer, in a subharmonic mixer

the incoming mw signal is mixed not with the fundamental frequency of the local oscillator (LO) input but with a higher harmonic. The local oscillator can, therefore, operate at a lower frequency with all the advantages of lower frequency components. The disadvantage, of course, is the less efficient mixing process. The LO is provided by a phase-locked, doubled 90.3 GHz Gunn oscillator. The necessary reference signal is supplied directly from the 10 MHz source of the transmitter control module. With the subharmonic mixer running at the 2nd LO harmonic, the EPR signal at 360 GHz is down-converted with a LO frequency of 361.2 GHz, so the resulting IF frequency is 1.2 GHz. This is then passed through a low-noise amplifier with 35 dB gain and a video filter. The noise figure of the complete receiver module is 15 dB. This performance is comparable to that of the most sensitive InSb hot-electron bolometer detectors nowadays available. The signal at 1.2 GHz is down-converted by a quadrature IF mixer (Anaren Microwave). The LO for this mixer is provided by a 1.21 GHz dielectric resonator oscillator (DRO) which again is phase-locked to the 10 MHz master oscillator. Since in a quadrature mixer both in-phase and out-of-phase signal components are generated simultaneously, both the absorptive and dispersive signal components can be detected in a single experimental run.

In the 360 GHz spectrometer [87, 313], we employ a quasioptical transmission line setup in which a Gaussian beam is launched into free space via a corrugated horn antenna. If free-space propagation is not feasible, cylindrical corrugated oversized waveguides are used. Conventional smooth-walled waveguides are inferior to corrugated waveguides due to excitation of higher-order modes, generation of standing waves at transitions from and to fundamental-mode waveguide sections, and distortion of the propagated beam polarization [322]. In analogy to geometrical optics, to refocus a diverging beam one can employ either curved mirrors or lenses. Lenses can be the origin of standing waves in the system and cause dielectric losses. Therefore, all focusing elements in our quasioptical transmission line are metallic off-axis elliptical mirrors.

To couple the microwave to the Fabry–Perot sample resonator, the output beam needs to be focused to a beam waist of 1.0 mm. This is achieved by a corrugated tapered waveguide section, made of gold-plated copper, at the end of the cylindrical waveguide. The corrugated waveguide itself consists of 100 mm long electroformed sections soldered to an overall length of 1080 mm. The diameter is 23 mm, being reduced by the taper over a length of 20 mm to 3 mm. The corrugation depth is 0.6 mm and the slot/metal pitch 0.25 mm. The material of the main waveguide section is German silver, which is preferred to copper since it has a lower coefficient for heat conduction.

The linear polarization of the Gaussian beam is utilized in an induction-mode detection scheme that was first described by Teaney et al. [323]. Later examples of this detection scheme at high magnetic fields were introduced for transmission mode by Prisner et al. [95] and for reflection mode by Smith et al. [90]. The Gaussian mw beam launched by the transmitter horn antenna has an initial beam waist w_0 of 1.48 mm and is linearly polarized. As is indicated in Fig. 24, the first off-axis mirror focuses the widened beam onto the upper end of the corrugated waveguide to a beam waist of 7.24 mm. On its way, the beam passes through a wire-grid polarizer that is oriented with an angle of 45° with respect to the optical axis.

The free-standing wires (12 wires/mm, 25 μm diameter) allow mw radiation that is polarized perpendicular to the direction of the wires to pass because in this direction no electric currents are induced, while radiation polarized along the wire direction is effectively reflected. Behind the polarizer, the residual radiation with polarization along the wires is attenuated by about 20 dB compared to the unattenuated component. By mounting a second grid on a rotation stage in front of the first, one obtains a polarizer/analyzer setup that acts as a variable attenuator with a dynamic range of 20 dB. The rotation stage is slightly tilted with respect to the optical axis to avoid the build-up of standing waves in the system.

In the cylindrically symmetric Fabry–Perot resonator, the excitation mw represents a composition of two circularly polarized modes with opposite polarization. Of those two modes only one interacts with the spin system and, therefore, becomes partially attenuated when magnetic resonance absorption occurs. Recombined with the unattenuated component, this yields elliptically polarized mw radiation that is reflected back into the corrugated waveguide. When hitting the wire-grid polarizer, only the component orthogonal to the excitation mw is reflected onto the receiver antenna, while the excitation power itself is passed to the transmitter tripler and attenuated there.

Essential in this context is the use of the cylindrically symmetric Fabry–Perot resonator as a bimodal cavity. Since all directions of polarization in the resonator are degenerate, both the excitation microwave and the EPR induction component, polarized orthogonally to the excitation component, have to be supported by the resonator structure. This also applies to the oversized waveguide transmission line. The use of a single-mode cavity, despite many advantages, is not possible within an induction-mode detection scheme.

The maximum obtainable isolation of the excitation from the detection arm is ultimately limited by the cross-polarized microwave component that is induced by the off-axis mirrors. This effect is partly corrected by the polarizer grid that is passed after the first mirror. Overall, this induction-mode setup provides an attenuation of the excitation power with respect to the EPR signal power of 20–30 dB.

The superconducting magnet is a Teslatron H system (Oxford Instruments). It can sustain a magnetic field of up to $B_0 = 14$ T. The experiments are typically run with a central magnetic field $B_0 = 12.846$ T, the resonance field for the free-electron g-value and a microwave frequency of 360 GHz. The lowest accessible g-value with a 14 T central field is $g = 1.84$.

Integrated into the main coil assembly is a superconducting sweep coil with a sweep range of ± 100 mT. This way the magnet can be swept with a sweep rate of up to 70 mT/min, while the main coil remains in persistent mode. The homogeneity of the magnet is specified to 3 ppm in a 10 mm sphere. This was verified with an NMR Gaussmeter with a deuterium probe that was moved along the symmetry axis of the magnet. The linearity of the field sweep has also been tested with an NMR gaussmeter for a full sweep. The sweep is not linear and after a half cycle, a remanence field of 4 mT can be observed. After a full cycle the field offset was 0.05 mT. This necessitates the use of a standard sample for magnetic field calibration. We normally use Mn^{2+}/MgO dissolved in a polystyrene film as the standard sample whose magnetic interaction parameters are knows with high precision [74].

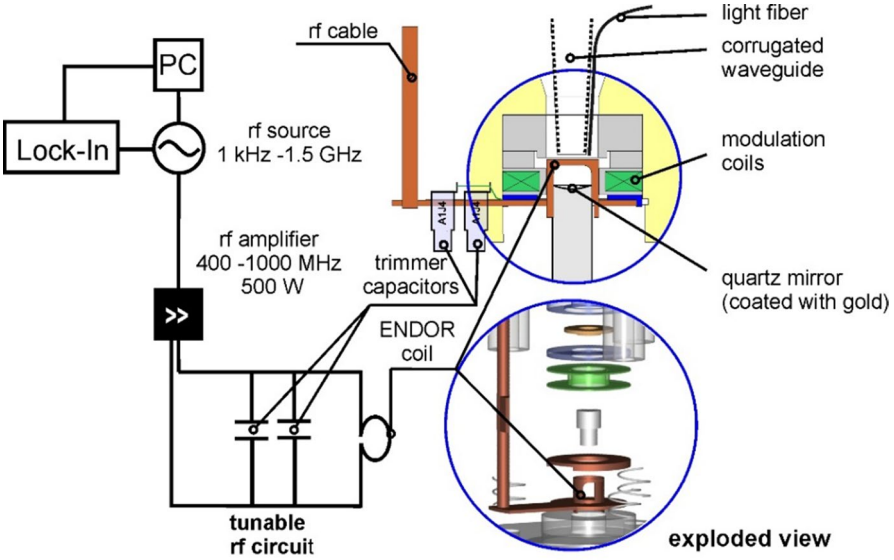

Fig. 25 Tunable rf circuit (left) together with a cross-section and an exploded view of the 360 GHz/550 MHz EPR/ENDOR probehead (right). The resonant rf circuit consists of a single-loop coil and two trimmer capacitors, which provide frequency-tuning and -matching. The rf is generated by a sweepable generator, a power amplifier and a single-turn coil, which generates a B_2 field perpendicular to the microwave field B_1. The sample is placed on the gold-coated spherical quartz mirror. Note that for the EPR/ENDOR experiment the mw coupling mesh as the flat mirror of a Fabry–Perot resonator was removed. For details, see [152, 314]

The warm bore of the cryomagnet has a diameter of 88 mm. This allows to employ a cryostat with the rather large diameter of 62 mm to accommodate the probehead. The cryostat is a helium-cooled static-flow cryostat (Oxford Instruments, CF1200) which covers a temperature range of 3.8–300 K. In a static-flow design, the probehead is not cooled directly by the He vapor. Instead, the probehead space is closed off and filled with a buffer gas (e.g., argon) which in turn is cooled by a copper heat exchanger shield that is in direct contact with the helium. This setup avoids stability problems which often arise in direct-flow cryostat designs.

3.2.3 Probeheads

Several probeheads have been developed for EPR and ENDOR measurements at 360 GHz [152, 313]. The ENDOR version is shown in Fig. 25. Both EPR and ENDOR probeheads are based on the plane-concave Fabry–Perot resonator operated in the TEM_{006} mode. With a resonant mirror distance $d = 2.58$ mm and curvature radius $R = 8.06$ mm, one obtains a confocal distance of 3.76 mm. A typical value for the finesse of the resonator with sample is $F = 160$, giving for the loaded quality factor $Q_L = 800$. Coupling to the tapered end of the corrugated waveguide is achieved through the flat mirror, which is a highly reflective metallic mesh (typically 30 wires/mm). The mesh consists of electro-formed copper and is stretched to an exchangeable mesh holder, where it is fixed onto a circular frame. Since the mesh

holders are exchangeable, the mesh can be replaced by another mesh with different reflectivity, thus allowing for variable coupling for different samples. Tuning is achieved by translating the spherical mirror along three guide rods via a micrometer screw on top of the corrugated waveguide outside the magnet. The field modulation coils frame the spherical mirror. The modulation amplitudes can be raised up to 3 mT without generating excessive microphonics. A quartz fiber integrated into the probehead allows for photo-generation of radicals or triplet states inside the resonator by laser excitation. The overall detection sensitivity of the spectrometer equipped with the FP resonator has been measured to be $1.5 \cdot 10^{10}$ spins/mT at 1 Hz detection bandwidth by evaluating the signal-to-noise ratio of a known number of spins in a Mn^{2+} sample.

Figure 25 shows a cross section and an exploded view of the 360 GHz EPR/ENDOR probehead together with the resonant rf circuit for ENDOR experiments. The sample is placed on the gold-coated quartz mirror and irradiated by a mw field B_1 and a perpendicular rf field B_2 that is produced in a single-loop ENDOR coil. The ENDOR coil is part of the resonant circuit (center frequency 547 MHz; bandwidth 60 MHz) which can be frequency-tuned and impedance-matched by two trimmer capacitors mounted on the rf circuit plate close to the ENDOR coil. The rf power is provided by a digital frequency generator (Hewlett Packard, 8648B) and amplified by a 500 W power amplifier (Amplifier Research, 500HB). To reduce standing waves in the rf transmission line, a high-power rf circulator is used. The maximum B_2 generated by the ENDOR coil is 0.8 mT at 20 W incident rf power, for which unwanted heating effects are avoided. ENDOR spectra are typically recorded at a fixed external field B_0 and mw field B_1, while sweeping the frequency of the rf field B_2. The B_2 field is frequency modulated, and the ENDOR signals are recorded using a lock-in amplifier. For more details of the 360 GHz ENDOR experiments, see [152].

To conclude this section: Many options for exploiting the strength of high-field EPR spectroscopy in terms of spectral and temporal resolution critically rely on the availability of powerful cw and pulsed mm and sub-mm microwave sources. Naturally, the technical difficulties and limitations rise with rising microwave frequencies. Nevertheless, the 360 GHz spectrometer could already be used to perform successful studies on the structure of protein systems such as the cofactors of photosynthesis and DNA photolyase in their binding pockets. Examples of pertinent references include: [324–327].

Acknowledgements Over the years, many co-workers in the Möbius group—diploma and PhD students, postdocs and senior scientists—have contributed to the high-field EPR work reviewed in this article. In the course of these activities, it was their enthusiasm and tenacity which allowed to solve the numerous technical problems in developing high-field EPR, ENDOR, ESEEM, EDNMR and PELDOR instrumentation operating at 95 GHz or 360 GHz, and to apply these techniques to novel molecular systems from biology and biochemistry. In this context, we specifically acknowledge the former students (in chronological order): Olaf Burghaus, Anna Toth-Kischkat, Thomas Götzinger, Robert Klette, Martin Rohrer, Moritz Knüpling, Jens Törring, Gordon Elger, Michael Fuhs, Ingo Köhne, Andreas Bloeß, Martin Fuchs, Marcus Gallander, Alexander Schnegg; and the former postdocs (in alphabetical order): Edmund Haindl, Martina Huber, Chris Kay, Wolfgang Lubitz, Martin Plato, Thomas Prisner, Anton Savitsky and Stefan Weber. K.M. wants to thank them all for their eminent contributions to exciting experiments of high-field EPR spectroscopy.

Author contributions All authors equally contributed to the writing of the manuscript.

Funding Open Access funding enabled and organized by Projekt DEAL. Over the years, our high-field EPR activities have received enduring support from the Deutsche Forschungsgemeinschaft (DFG) in the frame of DFG priority programs (SFB 337, SFB 498, III P 5-MO 132/14-1, SPP 1051, MO 132/19-2, Cluster of Excellence RESOLV EXC 1069); by Volkswagenstiftung priority programs (I/70 382, I/73 145, I/73 146); and by the European Union network programs HCM (CHRX-CT9-30 328), TMR (FMRX-CT98-0214), INTAS (01-483) and COST (P15), which is gratefully acknowledged. K. M. is particularly thankful for the long-standing support of his scientific work by the Freie Universität Berlin (Department of Physics) and the Max Planck Gesellschaft (Max Planck Institute for Chemical Energy Conversion).

Declarations

Conflict of Interest The authors declare no competing financial interests.

References

1. K. Möbius, A. Savitsky, *High-field EPR spectroscopy on proteins and their model systems: characterization of transient paramagnetic states* (RSC Publishing, London, 2009)
2. A.A. Sukhanov, M.D. Mamedov, K. Möbius, A.Y. Semenov, K.M. Salikhov, Appl. Magn. Reson. **51**, 909–924 (2020)
3. S. Mula, A. Savitsky, K. Möbius, W. Lubitz, J.H. Golbeck, M.D. Mamedov, A.Y. Semenov, A. van der Est, Photochem. Photobiol. Sci. **11**, 946–956 (2012)
4. A. Savitsky, O. Gopta, M. Mamedov, J.H. Golbeck, A. Tikhonov, K. Möbius, A. Semenov, Appl. Magn. Reson. **37**, 85 (2009)
5. M. Malferrari, A. Savitsky, M.D. Mamedov, G.E. Milanovsky, W. Lubitz, K. Möbius, A.Y. Semenov, G. Venturoli, Biochim. Biophys. Acta, Bioenergy. **1857**, 1440–1454 (2016)
6. K. Möbius, A. Savitsky, M. Malferrari, F. Francia, M.D. Mamedov, A.Y. Semenov, W. Lubitz, G. Venturoli, Appl. Magn. Reson. **51**, 773–850 (2020)
7. A.A. Sukhanov, M.D. Mamedov, K. Möbius, A.Y. Semenov, K.M. Salikhov, Appl. Magn. Reson. **49**, 1011–1025 (2018)
8. A. Savitsky, M. Malferrari, F. Francia, G. Venturoli, K. Möbius, J. Phys. Chem. B. **114**, 12729–12743 (2010)
9. M. Malferrari, A. Savitsky, W. Lubitz, K. Möbius, G. Venturoli, J. Phys. Chem. Lett. **7**, 4871–4877 (2016)
10. K. Möbius, W. Lubitz, N. Cox, A. Savitsky, Magnetochem. **4**, 50 (2018)
11. A. Savitsky, J. Niklas, J.H. Golbeck, K. Möbius, W. Lubitz, J. Phys. Chem. B. **117**, 11184–11199 (2013)
12. A. Nalepa, K. Möbius, W. Lubitz, A. Savitsky, J. Magn. Reson. **242**, 203–213 (2014)
13. K. Möbius, W. Lubitz, A. Savitsky, Prog. Nucl. Magn. Reson. Spectrosc. **75**, 1–49 (2013)
14. M. Malferrari, A. Nalepa, G. Venturoli, F. Francia, W. Lubitz, K. Möbius, A. Savitsky, Phys. Chem. Chem. Phys. **16**, 9831–9848 (2014)
15. I. Shelaev, M. Gorka, A. Savitsky, V. Kurashov, M. Mamedov, F. Gostev, K. Möbius, V. Nadtochenko, J. Golbeck, A. Semenov, Z. Phys, Chem. **231**, 325–345 (2017)

16. A. Nalepa, M. Malferrari, W. Lubitz, G. Venturoli, K. Möbius, A. Savitsky, Phys. Chem. Chem. Phys. **19**, 28388–28400 (2017)
17. A. Nalepa, K. Möbius, M. Plato, W. Lubitz, A. Savitsky, Appl. Magn. Reson. **50**, 1–16 (2019)
18. S.D. Chemerisov, G.D. Perekhodtsev, D.S. Tipikin, Y.S. Lebedev, A.I. Prokof'ev, A.I. Aleksandrov, A.A. Dubinskii, K. Möbius, O.G. Poluektov, J. Schmidt, J. Chem. Soc., Faraday Trans. **92**, 1959–1968 (1996)
19. G. Rist, J.S. Hyde, J. Chem. Phys. **49**, 2449 (1968)
20. G. Rist, J.S. Hyde, J. Chem. Phys. **50**, 4532 (1969)
21. G. Rist, J.S. Hyde, J. Chem. Phys. **52**, 4633 (1970)
22. A.W. Hornig, J.S. Hyde, Mol. Phys. **6**, 33–41 (1963)
23. S.D. Chemerisov, O.Y. Grinberg, D.S. Tipikin, Y.S. Lebedev, H. Kurreck, K. Möbius, Chem. Phys. Lett. **218**, 353–361 (1994)
24. D.S. Tipikin, G.G. Lazarev, Y.S. Lebedev, Zh. Fiz, Khim. **67**, 176–179 (1993)
25. M.R. Fuchs, A. Schnegg, M. Plato, C. Schulz, F. Müh, W. Lubitz, K. Möbius, Chem. Phys. **294**, 371–384 (2003)
26. C.P. Poole, *Electron spin resonance* (Wiley, New York, 1983)
27. G. Feher, Bell Syst. Tech. J. **36**, 449–484 (1957)
28. Z.C. Liang, J.H. Freed, J. Phys. Chem. B. **103**, 6384–6396 (1999)
29. J.H. Freed, Annu. Rev. Phys. Chem. **51**, 655–689 (2000)
30. P.P. Borbat, A.J. Costa-Filho, K.A. Earle, J.K. Moscicki, J.H. Freed, Science **291**, 266–269 (2001)
31. J. H. Freed, *in Very high frequency (VHF) ESR/EPR*, ed. by O. Grinberg, L. J. Berliner. Kluwer/ Plenum Publishers, New York, (2004), pp. 19–45
32. R.J. Blume, Phys. Rev. **109**, 1867–1873 (1958)
33. A. Schweiger, G. Jeschke, *Principles of pulse electron paramagnetic resonance* (Oxford University Press, Oxford, 2001)
34. K.M. Salikhov, A.G. Semenov, Y.D. Tsvetkov, *Electron spin echo and its applications* (Nauka, Moscow, 1976)
35. A.D. Milov, K.M. Salikhov, Y.D. Tsvetkov, Zh. Eksper, Teor. Fiz. **63**, 2329–2335 (1972)
36. A.D. Milov, K.M. Salikhov, M.D. Schirov, Fiz. Tverd. Tel. **23**, 957 (1981)
37. K.M. Salikhov, C.H. Bock, D. Stehlik, Appl. Magn. Reson. **1**, 195–213 (1990)
38. K.M. Salikhov, Y. Kandrashkin, A.K. Salikhov, Appl. Magn. Reson. **3**, 199–216 (1992)
39. D. Stehlik, K. Möbius, Annu. Rev. Phys. Chem. **48**, 745–784 (1997)
40. G. Feher, Phys. Rev. **103**, 834–835 (1956)
41. W.B. Mims, Proc. R. Soc. London Ser. A. **283**, 452–457 (1965)
42. E.R. Davies, Phys. Lett. A. **47**, 1–2 (1974)
43. A. Cederquist, PhD Thesis, Washington University, St. Louis, Missouri, (1963)
44. J.S. Hyde, A.H. Maki, J. Chem. Phys. **40**, 3117–3118 (1964)
45. J. H. Freed, *in Multiple electron resonance spectroscopy*, ed. by M. M. Dorio, M. M., J. H. Freed. Plenum Press, New York, (1979), pp. 73–142
46. G. Feher, Physica. **24**, S80–S87 (1958)
47. J.H. Freed, J. Chem. Phys. **50**, 2271–2272 (1969)
48. K.P. Dinse, R. Biehl, K. Möbius, J. Chem. Phys. **61**, 4335–4341 (1974)
49. H. Kurreck, B. Kirste, W. Lubitz, *Electron-nuclear double resonance spectroscopy of radicals in solution* (Wiley, New York, 1988)
50. F. Gerson, W. Huber, *Electron spin resonance spectroscopy of organic radicals* (Wiley-VCH, Weinheim, 2003)
51. F. Gerson, G. Gescheidt, *in Biological magnetic resonance*, ed. by S. S. Eaton, G. R. Eaton, L. J. Berliner. Springer, New York, (2005), pp. 145–164
52. R. Biehl, M. Plato, K. Möbius, J. Chem. Phys. **63**, 3515–3522 (1975)
53. R.J. Cook, D.H. Whiffen, Proc. R. Soc. Lond. **84**, 845–848 (1964)
54. H. Levanon, K. Möbius, Annu. Rev. Biophys. Biomol. Struct. **26**, 495–540 (1997)
55. W. Lubitz, F. Lendzian, *in Biophysical techniques in photosynthesis*, ed. by J. Amesz, A. J. Hoff. Kluwer, Dordrecht, (1996), pp. 255–275
56. W.B. Mims, Phys. Rev. B. **5**, 2409–2419 (1972)
57. S.S. Kim, S.I. Weissman, J. Am. Chem. Soc. **101**, 5863–5864 (1979)
58. A.J. Hoff, *Advanced EPR applications in biology and biochemistry* (Elsevier, Amsterdam, 1989)
59. K. A. McLauchlan, M. T. Yeung, *in Electron spin resonance*, ed. by N. Atherton, E. R. Davies, B. C. Gilbert (Royal Society of Chemistry, Cambridge, 1994), pp. 32–62

60. T.F. Prisner, M. Rohrer, K. Möbius, Appl. Magn. Reson. **7**, 167–183 (1994)
61. A. Savitsky, M. Kühn, D. Duche, K. Möbius, H.J. Steinhoff, J. Phys. Chem. B. **108**, 9541–9548 (2004)
62. J. van Tol, L.C. Brunel, R.J. Wylde, Rev. Sci. Instr. **76**, 074101 (2005)
63. L.J. Berliner, S.S. Eaton, G.R. Eaton (eds.), *Distance measurements in biological systems by EPR* (Kluwer/Plenum, New York, 2000)
64. A.D. Milov, A.B. Ponomarev, Y.D. Tsvetkov, Chem. Phys. Lett. **110**, 67–72 (1984)
65. M. Pannier, S. Veit, A. Godt, G. Jeschke, H.W. Spiess, J. Magn. Reson. **142**, 331–340 (2000)
66. S. Saxena, J.H. Freed, J. Phys. Chem. A. **101**, 7998–8008 (1997)
67. L.V. Kulik, S.A. Dzuba, I.A. Grigoryev, Y.D. Tsvetkov, Chem. Phys. Lett. **343**, 315–324 (2001)
68. Y. S. Lebedev, *in Foundations of modern EPR*, ed. by S. S. Eaton, K. M. Salikhov (World Scientific, Singapore, 1998), p. 731
69. O. Grinberg, A. A. Dubinskii, *in Very high frequency (VHF) ESR/EPR*, ed. by O. Grinberg, L. J. Berliner (Kluwer/Plenum Publishers, New York, 2004), pp. 1–15
70. D.J.E. Ingram, *Biological and biochemical applications of electron spin resonance* (Adam Hilger, London, 1969)
71. E.F. Slade, D.J.E. Ingram, Proc. R. Soc. Lond. Ser. A. **312**, 85–98 (1969)
72. I. Amity, Rev. Sci. Instr. **41**, 1492–1494 (1970)
73. Y. Alpert, Y. Couder, J. Tuchendl, H. Thome, Biochim. Biophys. Acta. **322**, 34–37 (1973)
74. O. Burghaus, M. Rohrer, T. Götzinger, M. Plato, K. Möbius, Meas. Sci. Technol. **3**, 765–774 (1992)
75. E. Haindl, K. Möbius, H. Oloff, Z. Naturforsch. A. **40**, 169–172 (1985)
76. W. Wang, R.L. Belford, R.B. Clarkson, P.H. Davis, J. Forrer, M.J. Nilges, M.D. Timken, T. Walczak, M.C. Thurnauer, J.R. Norris, A.L. Morris, Y. Zhang, Appl. Magn. Reson. **6**, 195–215 (1994)
77. R.T. Weber, J.A.J.M. Disselhorst, L.J. Prevo, J. Schmidt, W.T. Wenckebach, J. Magn. Reson. **81**, 129–144 (1989)
78. O.J. Grinberg, A.A. Dubinskii, V.F. Shuvalov, L.G. Oranskii, V.I. Kurochkin, J.S. Lebedev, Dokl. Akad. Nauk SSSR. **230**, 884–887 (1976)
79. T. Tatsukawa, T. Maeda, H. Sasai, T. Idehara, I. Mekata, T. Saito, T. Kanemaki, Int. J. Infrared. Milli. **16**, 293–305 (1995)
80. L.R. Becerra, G.J. Gerfen, B.F. Bellew, J.A. Bryant, D.A. Hall, S.J. Inati, R.T. Weber, S. Un, T.F. Prisner, A.E. McDermott, K.W. Fishbein, K.E. Kreischer, R.J. Temkin, D.J. Singel, R.G. Griffin, J. Magn. Reson. A. **117**, 28–40 (1995)
81. W.B. Lynch, K.A. Earle, J.H. Freed, Rev. Sci. Instr. **59**, 1345–1351 (1988)
82. K.A. Earle, D.S. Tipikin, J.H. Freed, Rev. Sci. Instr. **67**, 2502–2513 (1996)
83. K.A. Earle, J.H. Freed, Appl. Magn. Reson. **16**, 247–272 (1999)
84. A.L. Barra, L.C. Brunel, J.B. Robert, Chem. Phys. Lett. **165**, 107–109 (1990)
85. F. Muller, M.A. Hopkins, N. Coron, M. Grynberg, L.C. Brunel, G. Martinez, Rev. Sci. Instr. **60**, 3681–3684 (1989)
86. V.F. Tarasov, G.S. Shakurov, Appl. Magn. Reson. **2**, 571–576 (1991)
87. M.R. Fuchs, T.F. Prisner, K. Möbius, Rev. Sci. Instr. **70**, 3681–3683 (1999)
88. E.J. Reijerse, P.J. van Dam, A.A.K. Klaassen, W.R. Hagen, P.J.M. van Bentum, G.M. Smith, Appl. Magn. Reson. **14**, 153–167 (1998)
89. H.P. Moll, C. Kutter, J. van Tol, H. Zuckerman, P. Wyder, J. Magn. Reson. **137**, 46–58 (1999)
90. G.M. Smith, J.C.G. Lesurf, R.H. Mitchell, P.C. Riedi, Rev. Sci. Instr. **69**, 3924–3937 (1998)
91. M. Rohrer, J. Krzystek, V. Williams, L.C. Brunel, Meas. Sci. Technol. **10**, 275–284 (1999)
92. T. F. Prisner, *in Advances in magnetic and optical resonance*, ed. by W. Warren (Academic, New York, 1997), pp. 245–299
93. J. Allgeier, J. A. J. M. Disselhorst, R. T. Weber, W. T. Wenckebach, J. Schmidt, *in Modern pulsed and continuous-wave electron spin resonance*, ed. by L. Kevan, M. K. Bowman (Wiley, New York, 1990), pp. 267–283
94. A.Y. Bresgunov, A.A. Dubinskii, V.N. Krimov, Y.G. Petrov, O.G. Poluektov, Y.S. Lebedev, Appl. Magn. Reson. **2**, 715–728 (1991)
95. T.F. Prisner, S. Un, R.G. Griffin, Israel J. Chem. **32**, 357–363 (1992)
96. O. Burghaus, A. Toth-Kischkat, R. Klette, K. Möbius, J. Magn. Reson. **80**, 383–388 (1988)
97. J.W.A. Coremans, M. van Gastel, O.G. Poluektov, E.J.J. Groenen, T. den Blaauwen, G. van Pouderoyen, G.W. Canters, H. Nar, C. Hammann, A. Messerschmidt, Chem. Phys. Lett. **235**, 202–210 (1995)

98. L. Paschedag, J. van Tol, P. Wyder, Rev. Sci. Instr. **66**, 5098–5099 (1995)
99. J.A.J.M. Disselhorst, H. van der Meer, O.G. Poluektov, J. Schmidt, J. Magn. Reson. A. **115**, 183–188 (1995)
100. K.A. Earle, B. Dzikovski, W. Hofbauer, J.K. Moscicki, J.H. Freed, Magn. Reson. Chem. **43**, S256–S266 (2005)
101. M.M. Hertel, V.P. Denysenkov, M. Bennati, T.F. Prisner, Magn. Reson. Chem. **43**, S248–S255 (2005)
102. A.K. Hassan, A.L. Maniero, H. van Tol, C. Saylor, L.C. Brunel, Appl. Magn. Reson. **16**, 299–308 (1999)
103. P.A.S. Cruickshank, D.R. Bolton, D.A. Robertson, R.I. Hunter, R.J. Wylde, G.M. Smith, Rev. Sci. Instrum. **80**, 103102 (2009)
104. G. Smith, EPR Newslett. **32**, 5–6 (2022)
105. D. Schmalbein, G.G. Maresch, A. Kamlowski, P. Höfer, Appl. Magn. Reson. **16**, 185–205 (1999)
106. P. Höfer, A. Kamlowski, G. G. Maresch, D. Schmalbein, R. T. Weber, *in Very high frequency (VHF) ESR/EPR*, ed. by O. Grinberg, L. J. Berliner (Kluwer/Plenum Publishers, New York, 2004), pp. 401–429
107. K. Möbius, Chem. Soc. Rev. **29**, 129–139 (2000)
108. G. M. Smith, P. C. Riedi, *in Electron paramagnetic resonance*, ed. by Atherton, N. M., M. J. Davies, B. C. Gilbert (Royal Society of Chemistry, Cambridge, 2000), p. 164
109. T. Prisner, M. Rohrer, F. MacMillan, Annu. Rev. Phys. Chem. **52**, 279 (2001)
110. P. C. Riedi, G. M. Smith, *in Electron paramagnetic resonance*, ed. by B. C. Gilbert, B. C., M. J. Davies, D. M. Murphy (Royal Society of Chemistry, Cambridge, 2002), p. 254
111. J. H. Freed, *in Very high frequency (VHF) ESR/EPR*, ed. by O. Grinberg, L. J. Berliner (Kluwer/Plenum Publishers, New York, 2004), p. 21
112. K. A. Earle and A. I. Smirnov, *in Very high frequency (VHF) ESR/EPR*, ed. by O. Grinberg, L. J. Berliner (Kluwer/Plenum Publishers, New York, 2004), p. 469
113. T. F. Prisner, *in Very high frequency (VHF) ESR/EPR*, ed. by O. Grinberg, L. J. Berliner (Kluwer/Plenum Publishers, New York, 2004), p. 249
114. P. C. Riedi, G. M. Smith, *in Electron paramagnetic resonance*, ed. by B. C. Gilbert, M. J. Davies, D. M. Murphy (Royal Society of Chemistry, Cambridge, 2004), p. 338
115. K. Möbius, A. Savitsky, A. Schnegg, M. Plato, M. Fuchs, Phys. Chem. Chem. Phys. **7**, 19–42 (2005)
116. M. Bennati, T.F. Prisner, Rep. Prog. Phys. **68**, 411–448 (2005)
117. P. C. Riedi, *in Electron Paramagnetic Resonance*, ed. by B. C. Gilbert, M. J. Davies, D. M. Murphy (Royal Society of Chemistry, Cambridge, 2006), p. 245
118. K. Möbius, D. Goldfarb, *in Biophysical techniques in photosynthesis*, ed. by T. J. Aartsma, and J. Matysik (Springer, Dordrecht, 2008), pp. 267–304
119. Y.A. Grishin, M.R. Fuchs, A. Schnegg, A.A. Dubinskii, B.S. Dumesh, F.S. Rusin, V.L. Bratman, K. Möbius, Rev. Sci. Instr. **75**, 2926–2936 (2004)
120. A. Bloeß, K. Möbius, T.F. Prisner, J. Magn. Reson. **134**, 30–35 (1998)
121. A. Savitsky, A.A. Dubinskii, M. Plato, Y.A. Grishin, H. Zimmermann, K. Möbius, J. Phys. Chem. B **112**, 9079–9090 (2008)
122. G. Jeschke, EPR Newslett. **14**, 14–16 (2005)
123. O. Schiemann, T.F. Prisner, Q. Rev, Biophysics **40**, 1–53 (2007)
124. P.P. Borbat, J.H. Freed, EPR Newslett. **17**, 21–33 (2007)
125. V.P. Denysenkov, T.F. Prisner, J. Stubbe, M. Bennati, Appl. Magn. Reson. **29**, 375–384 (2005)
126. V.P. Denysenkov, T.F. Prisner, J. Stubbe, M. Bennati, Proc. Natl. Acad. Sci. USA **103**, 13386–13390 (2006)
127. Y. Polyhach, A. Godt, C. Bauer, G. Jeschke, J. Magn. Reson. **185**, 118–129 (2007)
128. A. Savitsky, A.A. Dubinskii, M. Flores, W. Lubitz, K. Möbius, J. Phys. Chem. B. **111**, 6245–6262 (2007)
129. M.M. Dorio, J.H. Freed (eds.), *Multiple electron resonance spectroscopy* (Plenum, New York, 1979)
130. N.M. Atherton, *Principles of electron spin resonance* (Ellis Horwood, New York, 1993)
131. A. A. Doubinski, *in Electron paramagnetic resonance*, ed. by N. M. Atherton, M. J. Davies, B. C. Gilbert (Royal Society of Chemistry, Cambridge, 1998), p. 211
132. J.H. Freed, Ann. Rev. Phys. Chem. **51**, 655–689 (2000)

133. M. Fuhs, K. Möbius, *in Lecture notes in physics*, ed. by C. Bertier, P. L. Levy, G. Martinez (Springer, Berlin, 2002), pp. 476–493
134. C. Wegener, A. Savitsky, M. Pfeiffer, K. Möbius, H.-J. Steinhoff, Appl. Magn. Reson. **21**, 441–452 (2001)
135. O. Grinberg, L.J. Berliner (eds.), *Very high frequency (VHF) ESR/EPR* (Kluwer/Plenum, New York, 2004)
136. W. Lubitz, K. Möbius, K.P. Dinse, Magn. Reson. Chem. **43**, S2–S3 (2005)
137. A. Abragam, *The principles of nuclear magnetism* (Oxford University Press, Oxford, 1961)
138. A. Carrington, A.D. McLachlan, *Introduction to magnetic resonance* (Harper, New York, 1967)
139. J.S. van der Brink, A.P. Spoyalov, P. Gast, W.B.S. van Liemt, J. Raap, J. Lugtenburg, A.J. Hoff, FEBS Lett. **353**, 273 (1994)
140. W. Lubitz, G. Feher, Appl. Magn. Reson. **17**, 1–48 (1999)
141. M. Flores, R. Isaacson, E. Abresch, R. Calvo, W. Lubitz, G. Feher, Biophys. J. **92**, 671–682 (2007)
142. P.J. Bratt, P. Heathcote, A. Hassan, J. van Tol, L.C. Brunel, J. Schrier, A. Angerhofer, Chem. Phys. **294**, 277–284 (2003)
143. W. R. Hagen, *in Advanced EPR, applications in biology and biochemistry*, ed. by A. J. Hoff (Elsevier, Amsterdam, 1989), pp. 785–812
144. J.R. Pilbrow, *Transition ion electron paramagnetic resonance* (Clarendon, Oxford, 1990)
145. J. Krzystek, J. Telser, B.M. Hoffman, L.C. Brunel, S. Licoccia, J. Am. Chem. Soc. **123**, 7890–7897 (2001)
146. C. Mantel, A.K. Hassan, J. Pecaut, A. Deronzier, M.N. Collomb, C. Duboc-Toia, J. Am. Chem. Soc. **125**, 12337–12344 (2003)
147. D. Goldfarb, V. Krymov, *in Very high frequency (VHF) ESR/EPR*, ed. by O. Grinberg, L. J. Berliner (Kluwer/Plenum, New York, 2004), pp. 305–351
148. A. L. Maniero, *in Very high frequency (VHF) ESR/EPR*, ed. by O. Grinberg, L. J. Berliner (Kluwer/Plenum, New York, 2004), pp. 478–494
149. K. Möbius, M. Plato, W. Lubitz, Phys. Rep. **87**, 171–208 (1982)
150. M. Mehring, P. Höfer, A. Grupp, Ber. Bunsen Ges. Phys. Chem. Chem. Phys. **91**, 1132–1137 (1987)
151. B. Epel, D. Goldfarb, J. Magn. Reson. **146**, 196–203 (2000)
152. A. Schnegg, A.A. Dubinskii, M.R. Fuchs, Y.A. Grishin, E.P. Kirilina, W. Lubitz, M. Plato, A. Savitsky, K. Möbius, Appl. Magn. Reson. **31**, 59–98 (2007)
153. J.H. Freed, J. Chem. Phys. **43**, 2312–2332 (1965)
154. J.H. Freed, J. Phys. Chem. **71**, 38–51 (1967)
155. J.H. Freed, D.S. Leniart, H.D. Connor, J. Chem. Phys. **58**, 3089–3105 (1973)
156. K.P. Dinse, R. Biehl, M. Plato, K. Möbius, J. Magn. Reson. **6**, 444–452 (1972)
157. K.P. Dinse, K. Möbius, R. Biehl, Z. Naturforsch. A **28**, 1069–1080 (1973)
158. M. Plato, W. Lubitz, K. Möbius, J. Phys. Chem. **85**, 1202–1219 (1981)
159. W. Lubitz, *in Electron paramagnetic resonance*, ed. by B. C. Gilbert, M. J. Davies, D. M. Murphy (Royal Society of Chemistry, Cambridge, 2004), pp. 174–242
160. K. Möbius, EPR Newslett. **16**, 18–24 (2006)
161. K. Möbius, R. Biehl, *in Mulitiple electron resonance spectroscopy*, ed. by M. M. Dorio, J. H. Freed (Plenum, New York, 1979), pp. 475–507
162. W. Lubitz, M. Plato, K. Möbius, R. Biehl, J. Phys. Chem. **83**, 3402–3413 (1979)
163. K. Möbius, D. Goldfarb, *in Biophysical techniques in photosynthesis, vol. II*, ed. by T. J. Aartsma, J. Matysik (Springer, Dordrecht, 2008), pp. 267–304
164. P.E. Doan, N.S. Lees, M. Shanmugam, B.M. Hoffman, Appl. Magn. Reson. **37**, 763–779 (2010)
165. M. van Gastel, W. Lubitz, EPR investigation of [NiFe] hydrogenases, in *High resolution EPR*. ed. by L. Berliner, G. Hanson (Springer, New York, 2009), pp.441–470
166. H. Blok, I. Akimoto, S. Milikisyants, P. Gast, E.J.J. Groenen, J. Schmidt, J. Magn. Reson. **201**, 57–60 (2009)
167. A. Silakov, E.J. Reijerse, S.P.J. Albracht, E.C. Hatchikian, W. Lubitz, J. Am. Chem. Soc. **129**, 11447–11458 (2007)
168. P. Höfer, A. Grupp, H. Nebenfuhr, M. Mehring, Chem. Phys. Lett. **132**, 279–282 (1986)
169. W.L. Hubbell, C. Altenbach, Curr. Opin. Struct. Biol. **4**, 566 (1994)
170. J. B. Feix and C. S. Klug, *in Electron paramagnetic resonance*, ed. by B. C. Gilbert, M. J. Davies, D. M. Murphy (Royal Society of Chemistry, Cambridge, 2006), pp. 50–72
171. H.-J. Steinhoff, Front. Biosci. **7**, 97–110 (2002)

172. A. I. Smirnov, *in Electron paramagnetic resonance*, ed. by B.C. Gilbert, M. J. Davies D. M. Murphy (Royal Society of Chemistry, Cambridge, 2002), pp. 109–136
173. K. Möbius, A. Savitsky, C. Wegener, M. Plato, M. Fuchs, A. Schnegg, A.A. Dubinskii, Y.A. Grishin, I.A. Grigor'ev, M. Kuhn, D. Duche, H. Zimmermann, H.J. Steinhoff, Magn. Reson. Chem. **43**, S4–S19 (2005)
174. M. Plato, H.J. Steinhoff, C. Wegener, J.T. Törring, A. Savitsky, K. Möbius, Mol. Phys. **100**, 3711–3721 (2002)
175. R. Owenius, M. Engström, M. Lindgren, M. Huber, J. Phys. Chem. A. **105**, 10967–10977 (2001)
176. M. Engström, R. Owenius, O. Vahtras, Chem. Phys. Lett. **338**, 407–413 (2001)
177. Z. Ding, A.F. Gulla, D.E. Budil, J. Chem. Phys. **115**, 10685–10693 (2001)
178. M. Pavone, A. Sillanpaa, P. Cimino, O. Crescenzi, V. Barone, J. Phys. Chem. B. **110**, 16189–16192 (2006)
179. H.J. Steinhoff, A. Savitsky, C. Wegener, M. Pfeiffer, M. Plato, K. Möbius, Biochim. Biophys. Acta. **1457**, 253–262 (2000)
180. T.I. Smirnova, T.G. Chadwick, M.A. Voinov, O. Poluektov, J. van Tol, A. Ozarowski, G. Schaaf, M.M. Ryan, V.A. Bankaitis, Biophys. J. **92**, 3686–3695 (2007)
181. J. Seliger, V. Zagar, Chem. Phys. **306**, 309–314 (2004)
182. J.N. Latosinska, M. Latosinska, J. Koput, J. Mol. Struct. **648**, 9–18 (2003)
183. A. Lai, H.L. Flanagan, D.J. Singel, J. Chem. Phys. **89**, 7161–7166 (1988)
184. H.L. Flanagan, D.J. Singel, J. Chem. Phys. **87**, 5606–5616 (1987)
185. H.L. Flanagan, G.J. Gerfen, A. Lai, D.J. Singel, J. Chem. Phys. **88**, 2162–2168 (1988)
186. A. Bloess, K. Möbius, T.F. Prisner, J. Magn. Reson. **134**, 30–35 (1998)
187. L. Kevan, *in Time domain electron spin resonance*, ed. by L. Kevan, R. N. Schwartz (Wiley, New York, 1979), pp. 279–341
188. J.W.A. Coremans, O.G. Poluektov, E.J.J. Groenen, G.W. Canters, H. Nar, A. Messerschmidt, J. Am. Chem. Soc. **119**, 4726–4731 (1997)
189. P. Schosseler, T. Wacker, A. Schweiger, Chem. Phys. Lett. **224**, 319–324 (1994)
190. L. Rapatskiy, N. Cox, A. Savitsky, W.M. Ames, J. Sander, M.M. Nowaczyk, M. Roegner, A. Boussac, F. Neese, J. Messinger, W. Lubitz, J. Am. Chem. Soc. **134**, 16619–16634 (2012)
191. A. Potapov, B. Epel, D. Goldfarb, J. Chem. Phys. **128**, 0542320 (2008)
192. M. Flores, A.G. Agrawal, M. van Gastel, W. Gaertner, W. Lubitz, J. Am. Chem. Soc. **130**, 2402–2403 (2008)
193. G. Jeschke, H.W. Spiess, Chem. Phys. Lett. **293**, 9–18 (1998)
194. A. Potapov, I. Pecht, D. Goldfarb, Phys. Chem. Chem. Phys. **12**, 62–65 (2010)
195. N. Cox, W. Lubitz, A. Savitsky, Mol. Phys. **111**, 2788–2808 (2013)
196. D. Baute, D. Goldfarb, J. Phys. Chem. A. **109**, 7865–7871 (2005)
197. M. Mehring, P. Höfer, A. Grupp, Ber. Bunsen-Ges. Phys. Chem. **91**, 1132–1137 (1987)
198. D. Goldfarb, B. Epel, H. Zimmermann, G. Jeschke, J. Magn. Reson. **168**, 75–87 (2004)
199. S. Khodadadi, A.P. Sokolov, Biochim. Biophys. Acta. **1861**, 3546–3552 (2017)
200. K. Henzler-Wildman, D. Kern, Nature **450**, 964–972 (2007)
201. H. Frauenfelder, G. Chen, J. Berendzen, P.W. Fenimore, H. Jansson, B.H. McMahon, I.R. Stroe, J. Swenson, R.D. Young, Proc. Nat. Acad. Sci. USA **106**, 5129–5134 (2009)
202. S. Khodadadi, A.P. Sokolov, Soft Matter **11**, 4984–4998 (2015)
203. P. Ball, Chem. Rev. **108**, 74–108 (2008)
204. V.C. Nibali, M. Havenith, J. Am. Chem. Soc. **136**, 12800–12807 (2014)
205. Y. Levy, J.N. Onuchic, Annu. Rev. Biophys. Biomol. Struct. **35**, 389–415 (2006)
206. H. Frauenfelder, P.W. Fenimore, G. Chen, B.H. McMahon, Proc. Nat. Acad. Sci. USA **103**, 15469–15472 (2006)
207. Y. Maruyama, Y. Harano, Chem. Phys. Lett. **581**, 85–90 (2013)
208. R.L. Baldwin, Proc. Nat. Acad. Sci. USA **111**, 13052–13056 (2014)
209. B. Halle, Philos T R Soc B. **359**, 1207–1223 (2004)
210. U. Ermler, G. Fritzsch, S.K. Buchanan, H. Michel, Structure. **2**, 925–936 (1994)
211. L. Baciou, H. Michel, Biochem. **34**, 7967–7972 (1995)
212. Y. Umena, K. Kawakami, J.R. Shen, N. Kamiya, Nature **473**, 55–65 (2011)
213. R.G. Bryant, C. R. Phys. **11**, 128–135 (2010)
214. N.V. Nucci, M.S. Pometun, A.J. Wand, J. Am. Chem. Soc. **133**, 12326–12329 (2011)
215. N.V. Nucci, M.S. Pometun, A.J. Wand, Nat. Struct. Mol. Biol. **18**, 245–315 (2011)
216. K. Yokoyama, T. Kamei, H. Minami, M. Suzuki, J. Phys. Chem. B. **105**, 12622–12627 (2001)

217. A.I. McIntosh, B. Yang, S.M. Goldup, M. Watkinson, R.S. Donnan, Chem. Soc. Rev. **41**, 2072–2082 (2012)
218. A.C. Fogarty, D. Laage, J. Phys. Chem. B. **118**, 7715–7729 (2014)
219. J.T. King, K.J. Kubarych, J. Am. Chem. Soc. **134**, 18705–18712 (2012)
220. D. Laage, G. Stirnemann, F. Sterpone, R. Rey, J.T. Hynes, Ann. Rev. Phys. Chem. **62**, 395–416 (2011)
221. D.M. Leitner, M. Gruebele, M. Havenith, Hfsp J. **2**, 314–323 (2008)
222. H.J. Bakker, J.L. Skinner, Chem. Rev. **110**, 1498–1517 (2010)
223. H. Frauenfelder, S.G. Sligar, P.G. Wolynes, Science **254**, 1598–1603 (1991)
224. L. Cordone, P. Galajda, E. Vitrano, A. Gassmann, A. Ostermann, F. Parak, Eur. Biophys. J. Biophys. **27**, 173–176 (1998)
225. G. Palazzo, A. Mallardi, A. Hochkoeppler, L. Cordone, G. Venturoli, Biophys. J. **82**, 558–568 (2002)
226. J.S. Clegg, Comp. Biochem. Phys. B. **128**, 613–624 (2001)
227. L. Cordone, M. Ferrand, E. Vitrano, G. Zaccai, Biophys. J. **76**, 1043–1047 (1999)
228. G. Caliskan, D. Mechtani, J.H. Roh, A. Kisliuk, A.P. Sokolov, S. Azzam, M.T. Cicerone, S. Lin-Gibson, I. Peral, J. Phys. Chem. **121**, 1978–1983 (2004)
229. G. Caliskan, A. Kisliuk, A.M. Tsai, C.L. Soles, A.P. Sokolov, J. Phys. Chem. **118**, 4230–4236 (2003)
230. F. Francia, M. Dezi, A. Mallardi, G. Palazzo, L. Cordone, G. Venturoli, J. Am. Chem. Soc. **130**, 10240–10246 (2008)
231. S. Giuffrida, G. Cottone, F. Librizzi, L. Cordone, J. Phys. Chem. B. **107**, 13211–13217 (2003)
232. L. Cordone, G. Cottone, S. Giuffrida, G. Palazzo, G. Venturoli, C. Viappiani, Biochim. Biophys. Acta. **1749**, 252–281 (2005)
233. F. Francia, G. Palazzo, A. Mallardi, L. Cordone, G. Venturoli, Biophys. J. **85**, 2760–2775 (2003)
234. M.S. Malferrari, A. Mamedov, M.D. Milanovsky, G.E. Lubitz, W. Möbius, K. Semenov, A. Su, G. Venturoli, Biochim. Biophys. Acta. **1857**, 1440–1454 (2016)
235. J.L. Green, C.A. Angell, J. Phys. Chem. **93**, 2880–2882 (1989)
236. F. Sussich, C. Skopec, J. Brady, A. Cesaro, Carbohydr. Res. **334**, 165–176 (2001)
237. A. Lerbret, P. Bordat, F. Affouard, M. Descamps, F. Migliardo, J. Phys. Chem. B. **109**, 11046–11057 (2005)
238. L. Cordone, G. Cottone, A. Cupane, A. Emanuele, S. Giuffrida, M. Levantino, Curr. Organ. Chem. **19**, 1684–1706 (2015)
239. G. Feher, J.P. Allen, M.Y. Okamura, D.C. Rees, Nature **339**, 111–116 (1989)
240. M.M. Leonova, T.Y. Fufina, L.G. Vasilieva, V.A. Shuvalov, Biochem.-Moscow. **76**, 1465–1483 (2011)
241. T.L. Olson, J.C. Williams, J.P. Allen, Photosynth. Res. **120**, 87–98 (2014)
242. G. Feher, M.Y. Okamura, Appl. Magn. Reson. **16**, 63–100 (1999)
243. J.P. Allen, G. Feher, T.O. Yeates, H. Komiya, D.C. Rees, Pros. Natl. Acad. Sci. USA **84**, 5730–5734 (1987)
244. K. M. R. Giangiacomo, D. E. Gunner, M. R. Dutton, L. P., *in Progress in photosynthesis research*, ed. by J. Biggins (Springer Netherlands, Dodrecht, 1987), pp. 409–412
245. R. Klette, J.T. Törring, M. Plato, K. Möbius, B. Bönigk, W. Lubitz, J. Phys. Chem. **97**, 2015–2020 (1993)
246. R.A. Isaacson, F. Lendzian, E.C. Abresch, W. Lubitz, G. Feher, Biophys. J. **69**, 311–322 (1995)
247. E. Bordignon, A.I. Nalepa, A. Savitsky, L. Braun, G. Jeschke, J. Phys. Chem. B. **119**, 13797–13806 (2015)
248. G.I. Likhtenshtein, J. Yamauchi, S.I. Nakatsuji, A.I. Smirnov, R. Tamura, *Nitroxides: applications in chemistry, biomedicine and materials science* (Wiley-VCH, Weinheim, 2008)
249. W. L. Hubbell, *in Membrane protein structure: experimental approaches*, ed. by S. H. White (Oxford University Press, London, 1994), pp. 224–248
250. P. Gajula, I.V. Borovykh, C. Beier, T. Shkuropatova, P. Gast, H.J. Steinhoff, Appl. Magn. Reson. **31**, 167–178 (2007)
251. E.M. Bruch, M.T. Warner, S. Thomine, L.C. Tabares, S. Un, J. Phys. Chem. B. **119**, 13515–13523 (2015)
252. M. Malferrari, F. Francia, G. Venturoli, J. Phys. Chem. B. **119**, 13600–13618 (2015)
253. M.S. Graige, G. Feher, M.Y. Okamura, Proc. Nat. Acad. Sci. USA **95**, 11679–11684 (1998)

254. F. Francia, G. Palazzo, A. Mallardi, L. Cordone, G. Venturoli, Biochim. Biophys. Acta. **1658**, 50–57 (2004)
255. D. Kleinfeld, M.Y. Okamura, G. Feher, Biochemistry **23**, 5780–5786 (1984)
256. B.H. McMahon, J.D. Muller, C.A. Wraight, G.U. Nienhaus, Biophys. J. **74**, 2567–2587 (1998)
257. G. Jeschke, A. Bender, H. Paulsen, H. Zimmermann, A. Godt, J. Magn. Reson. **169**, 1–12 (2004)
258. C.P. Slichter, *Principles of magnetic resonance* (Harper & Row, New York, 1963)
259. R.N. Schwartz, L.L. Jones, M.K. Bowman, J. Phys. Chem. **83**, 3429–3434 (1979)
260. K.M. Salikhov, S.A. Dzuba, A.M. Raitsimring, J. Magn. Reson. **42**, 255–276 (1981)
261. A.D. Milov, K.M. Salikohov, M.D. Shirov, Fiz. Tverd. Tela. **23**, 975–982 (1981)
262. A.D. Milov, A.B. Ponomarev, Y.D. Tsvetkov, J. Struct. Chem. **25**, 710–713 (1984)
263. A.M. Raitsimring, K.M. Salikhov, Bull. Magn. Reson. **7**, 184–217 (1985)
264. A.D. Milov, A.G. Maryasov, Y.D. Tsvetkov, Appl. Magn. Reson. **15**, 107–143 (1998)
265. R.G. Larsen, D.J. Singel, J. Chem. Phys. **98**, 5134–5146 (1993)
266. P.P. Borbat, J.H. Freed, Chem. Phys. Lett. **313**, 145–154 (1999)
267. P. P. Borbat, J. H. Freed, *in Distance measurements in biological systems by EPR*, ed. by L. J. Berliner, S. S. Eaton, G. R. Eaton (Kluwer, New York, 2000), pp. 383–459
268. K.V. Lakshmi, G.W. Brudvig, Curr. Opin. Struct. Biol. **11**, 523–531 (2001)
269. G. Jeschke, Chem. Phys. Chem. **3**, 927–932 (2002)
270. H.J. Steinhoff, Biol. Chem. **385**, 913–920 (2004)
271. S. S. Eaton, G. R. Eaton, *in Electron paramagnetic resonance*, ed. by B.C.Gilbert, M. J. Davies, D. M. Murphy (Royal Society of Chemistry, Cambridge, 2004), pp. 318–337
272. G. Jeschke, H. W. Spiess, *in Novel NMR and EPR techniques*, ed. by J. Dolinsek, M. Vilfan, S. Zumer (Springer, Berlin), pp. 21–63
273. A. V. Astashkin, A. Kawamori, *in Biophysical techniques in photosynthesis*, ed. by T. J. Aartsma, J. Matysik (Springer, Dordrecht, 2008), pp. 325–343
274. L.V. Kulik, S.V. Paschenko, S.A. Dzuba, J. Magn. Reson. **159**, 237–241 (2002)
275. V.P. Denysenkov, D. Biglino, W. Lubitz, T.F. Prisner, M. Bennati, Angew. Chem. Int. Ed. **47**, 1224–1227 (2008)
276. A.A. Dubinskii, Y.A. Grishin, A.N. Savitsky, K. Möbius, Appl. Magn. Reson. **22**, 369–386 (2002)
277. D.E. Kaplan, E.L. Hahn, J. Phys. Rad. **19**, 821–825 (1958)
278. J.P. Allen, G. Feher, T.O. Yeates, H. Komiya, D.C. Rees, Proc. Natl. Acad. Sci. USA **84**, 6162–6166 (1987)
279. J.P. Allen, G. Feher, T.O. Yeates, H. Komiya, D.C. Rees, Proc. Natl. Acad. Sci. USA **84**, 5730–5734 (1987)
280. J. Breton, C. Boullais, J.R. Burie, E. Nabedryk, C. Mioskowski, Biochemistry **33**, 14378–14386 (1994)
281. S.G. Zech, R. Bittl, A.T. Gardiner, W. Lubitz, Appl. Magn. Reson. **13**, 517–529 (1997)
282. I.V. Borovykh, S.A. Dzuba, I. Proskuryakov, P. Gast, A.J. Hoff, Biochim. Biophys. Acta. **1363**, 182–186 (1998)
283. E.C. Abresch, A.P. Yeh, S.M. Soltis, D.C. Rees, H.L. Axelrod, M.Y. Okamura, G. Feher, Biophys. J. **76**, A141–A141 (1999)
284. M.H.B. Stowell, T.M. McPhillips, D.C. Rees, S.M. Soltis, E. Abresch, G. Feher, Science **276**, 812–816 (1997)
285. G. Katona, A. Snijder, P. Gourdon, U. Andreasson, O. Hansson, L.E. Andreasson, R. Neutze, Nat. Struct. Mol. Biol. **12**, 630–631 (2005)
286. U. Heinen, L.M. Utschig, O.G. Poluektov, G. Link, E. Ohmes, G. Kothe, J. Am. Chem. Soc. **129**, 15935–15946 (2007)
287. M. Flores, A. Savitsky, E. C. Abresch, W. Lubitz, K. Möbius, *in Photosynthesis. energy from the sun*, ed. by J.F. Allen, B. Osmond, J. H. Golbeck, E. Gantt (Springer, Heidelberg, 2008), pp. 59–64
288. M.L. Paddock, M. Flores, R. Isaacson, C. Chang, E.C. Abresch, M.Y. Okamura, Biochemistry **46**, 8234–8243 (2007)
289. M. Flores, R. Isaacson, E. Abresch, R. Calvo, W. Lubitz, G. Feher, Biophys. J. **90**, 3356–3362 (2006)
290. M. Flores, R.A. Isaacson, R. Calvo, G. Feher, W. Lubitz, Chem. Phys. **294**, 401–413 (2003)
291. M. Flores, A. Savitsky, M.L. Paddock, E.C. Abresch, A.A. Dubinskii, M.Y. Okamura, W. Lubitz, K. Möbius, J. Phys. Chem. B. **114**, 16894–16901 (2010)
292. S. Sinnecker, M. Flores, W. Lubitz, Phys. Chem. Chem. Phys. **8**, 5659–5670 (2006)

293. W.B. Mims, Electron spin echos, in *Electron paramagnetic resonance*. ed. by S. Geschwind (Plenum, New York, 1972), pp.263–352
294. D. E. Budil, K. A. Earle, W. B. Lynch, J. H. Freed, *in Advanced EPR: appications in biology and biochemistry*, ed. by A. J. Hoff (Elsevier, Amsterdam, 1989), pp. 307–340
295. Y. S. Lebedev, *in Modern pulsed and continuous-wave electron spin resonance*, ed. by L. Kevan, M. K. Bowman (John Wiley, New York, 1990), pp. 365–404
296. D. E. Budil, K. A. Earle, *in Very high frequency (VHF) ESR/EPR*, ed. by O. Grinberg, L. J. Berliner (Kluwer/Plenum Publishers, New York, 2004), pp. 353–399
297. L. C. Brunel, J. van Tol, A. Angerhofer, S. Hill, J. Krzystek, A. L. Maniero, *in Very high frequency (VHF) ESR/EPR*, ed. by O. Grinberg, L. J. Berliner (Kluwer/Plenum Publishers, New York, 2004), pp. 466–536
298. T. F. Prisner, *in Advanced magnetic and optical resonance*, ed. by W. Warren (Academic, New York, 1997), pp. 245–299
299. O. Burghaus, *Diploma thesis* (Freie Universtät Berlin, Berlin, 1984)
300. O. Burghaus, E. Haindl, M. Plato, K. Möbius, J. Phys. E. **18**, 294–296 (1985)
301. O. Burghaus, PhD thesis, Freie Universtät Berlin, Berlin (1990)
302. T. Götzinger, *Diploma thesis* (Freie Universtät Berlin, Berlin, 1990)
303. M. Rohrer, *Diploma thesis* (Freie Universtät Berlin, Berlin, 1991)
304. M. Rohrer, PhD Thesis, Freie Universtät Berlin, Berlin (1995)
305. M. Rohrer, M. Plato, F. MacMillan, Y. Grishin, W. Lubitz, K. Möbius, J. Magn. Reson. A. **116**, 59–66 (1995)
306. R. Klette, PhD thesis, Freie Universtät Berlin, Berlin (1994)
307. T.F. Prisner, A. van der Est, R. Bittl, W. Lubitz, D. Stehlik, K. Möbius, Chem. Phys. **194**, 361–370 (1995)
308. A. Schnegg, *Diploma thesis* (Freie Universtät Berlin, Berlin, 1998)
309. M. Fuhs, PhD thesis, Freie Universtät Berlin, Berlin (1999)
310. M. Fuhs, T. Prisner, K. Möbius, J. Magn. Reson. **149**, 67–73 (2001)
311. M. Fuhs, A. Schnegg, T. Prisner, I. Köhne, J. Hanley, A.W. Rutherford, K. Möbius, Biochim. Biophys. Acta. **1556**, 81–88 (2002)
312. A.N. Savitsky, M. Galander, K. Möbius, Chem. Phys. Lett. **340**, 458–466 (2001)
313. M. Fuchs, PhD thesis, Freie Universtät Berlin, Berlin (1999)
314. A. Schnegg, PhD thesis, Freie Universtät Berlin, Berlin (2003)
315. P.F. Goldsmith, *Quasioptical systems* (IEEE Press, New York, 1998)
316. J.C.G. Lesurf, *Milimetre-wave optical, devices and systems* (Adam Hilger, New York, 1990)
317. A.F. Gulla, D.E. Budil, Concept. Magn. Reson. B. **22B**, 15–36 (2004)
318. K.A. Earle, R. Zeng, D.E. Budil, Appl. Magn. Reson. **21**, 275–286 (2001)
319. R.P. Leavitt, D.E. Wortman, C.A. Morrison, Appl. Phys. Lett. **35**, 363–365 (1979)
320. F. S. Rusin and Bogomolo, JEPT Letters-USSR. **4** 160 (1966)
321. K. Mizuno, S. Ono, The ledatron, in *Infrared and millimeter waves*. ed. by K.J. Button (New, York, 1979), pp.213–233
322. J. L. Doane, *in Infrared and millimeter waves*, ed. by K.J. Button (Academic Press New York, 1985), pp. 123–170
323. D.T. Teaney, M.P. Klein, A.M. Portis, Rev. Sci. Instr. **32**, 721–729 (1961)
324. C.W.M. Kay, R. Feicht, K. Schulz, P. Sadewater, A. Sancar, A. Bacher, K. Möbius, G. Richter, S. Weber, Biochem. **38**, 16740–16748 (1999)
325. M.R. Fuchs, E. Schleicher, A. Schnegg, C.W.M. Kay, J.T. Törring, R. Bittl, A. Bacher, G. Richter, K. Möbius, S. Weber, J. Phys. Chem. B. **106**, 8885–8890 (2002)
326. A. Schnegg, C.W.M. Kay, E. Schleicher, K. Hitomi, T. Todo, K. Möbius, S. Weber, Mol. Phys. **104**, 1627–1633 (2006)
327. A. Okafuji, A. Schnegg, E. Schleicher, K. Möbius, S. Weber, J. Phys. Chem. B. **112**, 3568–3574 (2008)